Copper Indium Sulfide Colloidal Quantum Dot Solar Cells

David So

under the supervision of
Professor Gerasimos Konstantatos

a thesis submitted in partial fulfillment
of the requirements for the degree of

Doctor

to the
Universitat Politecnica de Catalunya
Barcelona, 2016

ICFO
The Institute of Photonic Sciences

UNIVERSITAT POLITÈCNICA DE CATALUNYA
BARCELONATECH
UPC

About the cover

Colloidal quantum dot solar cell technology is one of the latest additions to the family of solar energy conversion devices but has been largely based on PbS which has the restricted element Pb. This work aims to introduce $CuInS_2$ as an alternative to PbS.

The cover represents a solar cell, having its corresponding layers labelled, with a sun in the background. The sun is rendered to show a spectrum of colors, which represents the colors attainable with quantum-confined $CuInS_2$ and is portrayed as a splash/burst, in the way that this work aims to introduce $CuInS_2$ to *make a splash*.

This image is done in watercolor to allude to the nontoxicity of the semiconductor as well as solution-based processes afforded by colloidal quantum dots. One can think of these materials as paints or inks which can be used to make devices.

To my mother Teresa,
who gave so much

ABSTRACT

The ubiquity of solar energy conversion technology is an exciting target which we aspire for in this century. Colloidal quantum dot (CQD) solar cells are an attractive platform, being low-cost and allowing facile control on film properties and device fabrication, but to date are dominated by PbS but contains the restricted element Pb. $CuInS_2$ (CIS) is a non-toxic alternative, showing promise in the bulk and as sensitizer but has not been thoroughly investigated for solid-state CQD solar cells. In this work we aim to incorporate CIS nanocrystals (NCs) into the gamut of CQD solar cell materials by making optoelectronic CQD solids, by fabricating functional devices in various architectures and by identifying and overcoming the limiting material properties and device mechanisms.

We described a synthethic scheme that resulted in CIS NCs that can be deposited as CQD solids with controllable thicknesses. CIS NCs are typically synthesized using long chain thiols which are difficult to remove from the NC surface. We introduced long chain amines and phosphines, decomposable chalcogenides and zinc oleate treatments to substitute the functions that the thiol performed. This led to cubic nanocrystals with controllable size, from 2 nm to 3.2 nm, and optical properties with bandgaps ranging from 2.5 eV to 1.5 eV. These particles are also copper poor, decorated with indium and zinc on the surface. With this, we were able to design a ligand exchange protocol using hard ligands for making solid-state CQD films which is a step forward to engineering optoelectronic devices.

We fabricated optoelectronic devices using these films and identified thin film properties that could limit device performance. These assemblies of CIS NCs couple to each other as seen in changes in photoluminescence lifetimes with distance. When the distance between nanocrystals is reduced, these *p*-type films conduct although having low mobilities ($\sim 10^{-5}$ $cm^2V^{-1}s^{-1}$), displaying features that signify high trap densities, such as high responsivity and long photoconductive decays. The ability to form solid-state films has allowed us to

fabricate optoelectronic devices such as transistors, photodetectors and solar cells. In solar cells, CIS CQD solids have led to good open-circuit volages (V_{OC}s), around 0.6 V, but low short-circuit currents (J_{SC}s), ~1 mA/cm^2, and fill factors (FFs), ~0.30. With the absorption coefficient of the CIS CQD solids, we found that the internal quantum efficiency (IQE) of these devices, is far below 10%. These highlight the importance of addressing the high trap density in the quantum dot solid.

We addressed the low J_{SC}s and FFs in CIS CQD solar cells by utilizing a bulk heterojunction (BHJ) architecture. This non-annealed architecture was fabricated by increasing the pore size of the TiO$_2$ network which allowed for the uniform and deep infiltration of CIS NCs. By using a BHJ architecture, we improved the performance of CIS CQD solar cells: mainly from an increase in J_{SC} and FF leading to a six-fold increase in efficiency from initially at 0.15% to 1.16%. From analysis of Suns-V_{oc}, -J_{sc} and transient V_{oc} and J_{sc} measurements, we have identified that BHJ devices have less trap-assisted recombination and a lower activation energy (E_U) for hole extraction. This was confirmed by shifts in the full device photoluminescence. We suggested that the BHJ structure allows for quenching of deeper tail states near the valence band in CIS by the transfer of electrons from TiO$_2$.

In this work, we have started from synthetic molecular precursors, to engineering supramolecular structures in trying to introduce CIS NCs into CQD optoelectronics, showcasing various devices: field effect transistors, photodetectors, bilayer and BHJ solar cells. In each stage, we have highlighted material, film and device properties which will be necessary for good performance. Ultimately this work aims to stimulate new interest in further development of CIS CQD solar cells, opening the possibility for non-toxic CQD photovoltaics.

Resumen

Conseguir la ubicuidad de la tecnología de conversión de energía solar es un objetivo al que aspiramos en este siglo. Las células solares de puntos cuánticos coloidales (CQD) constituyen una plataforma interesante, debido a su bajo coste y a que permiten un control sencillo sobre las propiedades de la película y la fabricación de dispositivos, pero que están dominadas por PbS. El $CuInS_2$ (CIS) es una alternativa no tóxica, prometedora en cuanto al grosor y como sensibilizadora, pero que no ha sido estudiada a fondo para su uso en células solares de CQD. El objetivo de este trabajo es incorporar nanocristales de CIS en toda la gama de materiales de células solares de CQD, mediante la creación de sólidos optoelectrónicos de CQD, fabricando dispositivos funcionales con diversas arquitecturas e identificando y superando las limitaciones de las propiedades de los materiales y los mecanismos de los dispositivos.

Describimos una estrategia sintética que resultó en nanocristales de CIS que pueden ser depositados en forma de sólidos de CQD con espesores controlables. Los nanocristales de CIS son típicamente sintetizados utilizando tioles de cadena larga que son difíciles de eliminar de su superficie. Introdujimos aminas y fosfinas de cadena larga, un calcogenuro descomponible y tratamientos de oleato de zinc para substituir las funciones que realizaba el tiol. Esto generó nanocristales cúbicos de tamaño controlable, de 2 nm a 3.2 nm, con E_g de entre 2.5 eV y 1.5 eV. Estás partículas también son pobres en cobre, y su superficie está cubierta de indio y zinc. Mediante este proceso hemos podido diseñar un protocolo de intercambio de ligandos utilizando ácidos duros para generar películas de CQD en estado sólido, lo que constituye un avance para la ingeniería de dispositvos optoelectrónicos.

Utilizando estas películas, fabricamos dispositivos optoelectrónicos e identificamos las propiedades de película fina que podrían limitar el rendimiento del dispositivo. Estos ensamblados de nanocristales de CIS se acoplan entre sí tal y como muestran los cambios en la duración de la fotoluminiscencia con la distancia. Cuando la distancia entre nanocristales se reduce, estas películas de

tipo-p conducen, a pesar de tener bajas movilidades ($\sim 10^{-5}$ cm^{2}V^{-1}s^{-1}) y de mostrar características que indican altas densidades de trampa, tales como una alta capacidad de respuesta y largos decaimientos fotoconductores. La capacidad para formar películas en estado sólido nos ha permitido fabricar dispositivos optoelectrónicos como transistores, fotodetectores y células solares. En las células solares, los sólidos de CQD de CIS han dado buenos V_{oc}s, en torno a 0.6 V, pero bajas J_{sc}s $\sim$1 mA/cm^2, y FFs $\sim$0.30. Los coeficientes de absorción de los sólidos de CQDs de CIS indicaron que la eficiencia quántica interna (IQE) de estos dispositivos está muy por debajo del 10%. Esto destaca la importancia de solucionar la alta densidad de trampas en los sólidos de punto cuántico.

Los bajos J_{sc} y FF en células solares de CQD de CIS fueron abordados utilizando una arquitectura de heterounión mayor (BHJ). Esta arquitectura no recocida se fabricó aumentando el tamaño de poro de la red de TiO$_2$, lo que permitió una infiltración uniforme y profunda de los nanocristales de CIS. Utilizando la arquitectura BHJ hemos mejorado el rendimiento de las células solares de CQD de CIS, principalmente debido al aumento de las Jsc y los FFs, que conducen a incremento de seis veces en la eficiencia, del 0.15% inicial al 1.16%. A partir del análisis de las mediciones de Suns-V_{oc}, -J_{sc} y V_{oc} y J_{sc} transitorios, hemos identificado que los dispositivos de BHJ tienen una menor recombinación asistida por trampa y una menor energía de activación (E_U) para la extracción de huecos. Esto fue confirmados por los cambios en la fotoluminiscencia del dispositivo total. Sugerimos que la estructura de BHJ permite el quenching de los tail states más profundos cerca de la nada de valencia en CIS por la transferencia de electrones de TiO$_2$.

En este trabajo, intentado introducir nanocristales de CIS en dispositivos optoelectrónicos, comenzando por precursores moleculares sintéticos hasta el diseño de estructuras supramoleculares. En cada etapa, hemos destacado el material y las propiedades de película y de dispositivos que serán necesarios para conseguir un buen rendimiento. Este trabajo tiene como objetivo final estimular un nuevo interés en futuros desarrollos de células solares de CQD de CIS, abriendo la posibilidad para fotovoltaicas no tóxicas de CQD.

Translation by Eneko Espillaga

ACKNOWLEDGEMENTS

This work, or rather, experience would not have been possible without the help of a lot of people I met along the way: people who have helped me scientifically and administratively, people how have been a support socially and groups of people who have helped fund the things we do.

Firstly, I thank Prof Gerasimos Konstantatos for believing that I can do it. On one occasion he referred to me as "leading the project on CZTS in our group". We eventually moved to CIS, but this gave me the sense that I wasn't working solely to follow orders and that my expertise was recognized. He gave me the freedom (and the funding) to do what I did, and how to do it, but was always available for a chat. And everything was clearer after each meeting. I am deeply grateful for his confidence and guidance throughout these years.

I am also thankful to the members of FON, formerly SPNP. You have all been a source of interesting conversations and laughs, emotional support and technical know-how. Luis had set-up most of the characterization hubs in the lab, writing the code for these. He has always been helpful in teaching how things work and which buttons to press. Pelayo was always jovial and was possibly the sharpest guy in the bunch. He was patient every time I told him that I needed help with the PL and Agilent—these machines can be quite moody. Dominik? He's in the cleanroom. When he was not, together with Luis and Pelayo, he made the office a great place to work in. Also he was ready to lend a hand when I needed help with photoconductivity and FET measurements. I am grateful for Maria's supervision during the first years when I was learning the nuts and bolts of the chemistry lab. She taught me to be rigorous in approaching each experiment. Tania has been a chat buddy in the lab and has made working in the lab feel like a relaxing day in the park, minus the fresh air. I appreciated Alex's efforts during the first years for performing EDX measurements for CZTS: the EDX is also quite moody. Agustin, Fiona and Silke are the managers of light next to our office. They have been a resource and help for me when it came to nanofabrication, reference articles,

seminal work, currents events, restaurant recommendations and music. Guillem, Alba, and partly Arianna, you silly interns. You never failed to give a fresh take on science and you have made life inside and outside ICFO fun. Nicky, and adopted group member Tim, you brought a positive and uplifting attitude to the group. You were a pleasure to work with when I was involved with ABS. Santanu has been an indispensable help for the electrical characterization of the devices. He has been a springboard for bouncing-off ideas. Zafer and Jianjun are my newest officemates, thank you for bearing with me when I vented my frustrations during the writing process. YuBi and Shuchi, thank you for the chats and company in the lab. And to the rest of the group, Helmut, Diana, Nengjie, Arup and Yiming, this group dynamic wouldn't have been complete without you and I am glad to have crossed paths with you.

I thank the groups of people at ICFO for keeping it a bright place to be in, the HR department, the purchasing department, the technical support from the nanofabrication and post-processing lab and the maintenance department.

I thank the people outside of ICFO who have been an emotional encouragement for me which had kept me going. Monday nights and the people of St George's, you have been a family to me. Eneko and the flatmates (Urtzi, Eric, Aurora, Rita, Lihong, Martin, Nicolas, Gonzalo, Emil and Fito the cat), Equador 1 3º3ª has been a home to me, thank you. The pub quiz gang, Miguel and the Filipino community, I enjoyed my life in Barcelona with you guys. I thank Jerome for being a great friend, a travel buddy and being ever ready to listen to my musings. And Elizabeth, you are and have been a wellspring of love, joy and reason. I am excited about what lies ahead because in the end I know you are there waiting for me.

For my mother, *maraming salamat sa mga taong ipinagpasakit mo dahil sa akin. Alam kong hindi ako naging kasing buti na anak, at na hindi ako nakatulong nang madalas. Ngunit salamat sa pagtutustos mo sa aking pagaaral, sa pagtitiwala mo sa akin at sa walang humpay mo sa pagmamahal sa akin.*

And to Him, who has made all things possible even though we have not begun to ask nor imagined what could be possible, be all the glory.

David So
27th May 2016, Barcelona

CONTENTS

LIST OF PUBLICATIONS BY THE AUTHOR

This work is based on the following publications:

So, D.; Konstantatos, G. Thiol-Free Synthesized Copper Indium Sulfide Nanocrystals as Optoelectronic Quantum Dot Solids. *Chem. Mater.* **2015**, 27, 8424–8432.

So, D.; Pradhan, S.; Konstantatos, G. Solid-State Colloidal CuInS$_2$ Quantum Dot Solar Cells enabled by Bulk Heterojunctions. *Nanoscale*, **2016**, DOI:10.1039/C6NR05563J, just accepted

Other publications by the author:

Stavrinadis, A.; Rath, A. K.; de Arquer, F. P. G.; Diedenhofen, S. L.; Magén, C.; Martinez, L.; So, D.; Konstantatos, G. Heterovalent Cation Substitutional Doping for Quantum Dot Homojunction Solar Cells. *Nat. Commun.* **2013**, 4, 2981.

Cao, Y.; Stavrinadis, A.; Lasanta, T.; So, D.; Konstantatos, G. The Role of Surface Passivation for Efficient and Photostable PbS Quantum Dot Solar Cells. *Nat. Energy* **2016**, 1, 16035.

Bernechea, M.; Miller, N. C.; Xercavins, G.; Mäckel, H.; So, D.; Stavrinadis, A.; Konstantatos, G. Solution Processed Solar Cells based on Environmentally Friendly AgBiS$_2$ Nanocrystals. *Nature Photonics*, **2016,** 10, 521–525.

Stavrinadis, A.; So, D.; Konstantatos, G. Low-Temperature, Solution-Based Sulfurization and Necking of PbS CQD Films. *J. Phys. Chem. C*, **2016**, DOI: 10.1021/acs.jpcc.6b05858, just accepted

LIST OF FIGURES, TABLES AND SCHEMES

FIGURES

Tables

xviii

Schemes

xx

LIST OF ACRONYMS

BET	*Brunauer, Emmett, Teller*
BHJ	*bulk heterojunction*
BJH	*Barrett-Joyner-Halenda*
CIGS	*copper indiun gallium sulfide*
CIS	*copper indium sulfide*
CP	*chalcopyrite*
CQD	*colloidal quantum dot*
CZTS	*copper zinc tin sulfide*
DDT	*dodecanethiol*
Δn	*excess charge carrier density*
DSSC	*dye-senstized solar cell*
EdAm	*ethylenediamine*
EDT	*ethanedithiol*
EDX	*energy-dispersive X-ray spectroscopy*
E_g	*band gap energy*
EMA	*effective mass approximation*
EQE	*external quantum efficiency*
E_U	*Urbach energy*
eV	*electron volt*
FET	*field effect transistor*
FF	*fill factor*
FTIR	*Fourier-transform infrared spectroscopy*
FWHM	*full width at half maximum*
G_m	*transconductance*
HSAB	*hard-soft acid-base theory*
I_{DS}	*drain-source current*
In_{Cu}	*indium in a copper site*
IQE	*internal quantum efficiency*
IV	*current-voltage*
J_{sc}	*short-circuit current*
LbL	*layer-by-layer*
λ_p	*photoluminescence peak*
MPA	*mercaptopropionic acid*
NC	*nanocrystal*
n_{id}	*idealty factor*
P3HT	*poly (3-hexylthiophene)*
PCE	*power conversion efficiency*
PL	*photoluminescence*
ppb	*parts per billion*
PSiF-DBT	*Poly[2,7-(9,9-dioctyl-dibenzosilole)-alt-4,7-bis(thiophen-2-yl)benzo-2,1,3-thiadiazole]*
PTB7	*Poly({4,8-bis[(2-ethylhexyl)oxy]benzo[1,*

	2-b:4,5-b']dithiophene-2,6-diyl}{3-fluoro-2-[(2ethylhexyl)carbonyl]thieno[3,4b]thiophenediyl})
PV	*photovoltaics*
QD	*quantum dot*
R_0	*Förster radius*
RPM	*revolutions per minute*
SAXS	*small-angle X-ray scattering*
SEM	*scanning electron microscopy*
SIMS	*secondary ion mass spectrometry*
SSSC	*semiconductor sensitized solar cells*
TEM	*transmission electron microscopy*
TMS	*hexamethyldisilathiane*
TOP	*trioctylphosphine*
TPC	*transient photocurrent*
TPV	*transient photovoltage*
TRPL	*time-resolved photoluminescence*
V_{Cu}	*copper vacancy*
V_{DS}	*drain-source voltage*
V_G	*gate voltage*
V_{oc}	*open-circuit voltage*
WZ	*wutzite*
XRD	*X-ray diffraction*
ZB	*zincblende*

CHAPTER 1
Introduction

1.1 The energy problem, the promise of solar energy and its challenges

We will probably see within this century, the end of the era of profitably extractable fossil fuels[1]. The oil market, accustomed to conventional petroleum reserves, will likely shift to nonconventional sources such as bitumen, tight oils, oil sand, and oil shale which present additional environmental and economic hurdles for extraction. Currently, we rely on fossil fuels for 78% of our energy expenditures[2]. This is concerning since our dependence on a declining energy source lies against a backdrop of a growing global power consumption, which has been increasing by 1.5% from 2007 to 2012, reaching 18 TW on 2013[2].

In response to this, various government policies have been put in place which provided subsidies in support of renewable energy developments, attracting investments and driving the cost-competitiveness of new technologies[3]. In 2014, renewable energies resulted in 58% of net additions to the global power capacity[3]. However, at present, non-traditional non-biomass-based renewable energies only satisfy less than 10% of our energy demand[3], even when solar energy alone—the sun irradiating 86 PW on the earth's surface[4]—could more than provide for the world´s energy consumption[5].

Solar photovoltaics (PV) is a rapidly growing sector, with more than 60% of the PV global capacity (177 GW) having been added over the past 3 years, with an increase of 40 GW in 2014[3]. While this is impressive, there is still a large gap

to be filled to reach the total global power consumption. The challenge of closing this gap, of widespread deployment of solar energy conversion technology, is met by addressing the following interrelated constraints:

Cost : Photovoltaics incur a heavy capital investment and must be able to compete with fossil fuels, demanding a cost per watt of 0.35 €/W.[5]

Lifetime : The operating lifetime should be longer than the operation time needed to balance fabrication and installation costs[5]. A longer lifetime will reduce the amortized cost of power produced.

Power conversion efficiency (PCE) : For the same fabrication cost, devices with higher efficiencies at converting solar to electrical power will drive down the cost per watt. On the other hand, for the same power produced, devices with higher PCEs will require a smaller installation area. To put this into scale, solar technology with an efficiency of 10%[6] would need to cover only 0.4% of the earth's surface to satisfy the global power demand.

Material abundance : Large quantities of material will be needed for addressing the TW power requirement; this is hindered by material abundance and will eventually affect cost. For example, 5 tons of the rare metal indium is needed for a 50 GW solar PV system based on copper indium gallium selenide[7]; this is mitigated by a predicted 47 kton-global reserve.

Toxicity : Whether this technology is deployed in a controlled enclosure or close to the consumer, health or environmental hazards of constituent materials or elements and their regulatory practices are important concerns. In particular, cadmium and selenium have low threshold concentrations which are deemed dangerous to life and health[8] and that in the European Union, under the Restriction of Hazardous Substances directive[9] the use of hazardous substances such as lead, mercury and cadmium is inhibited in electrical and electronic equipment.

1.2 Solar cell operation and characterization

Solar cell operation. A solar cell is a converter of electromagnetic energy from the sun (sunlight) to electrical energy. In all PV technology, power conversion is achieved through a series of processes. Light excites an electron in an absorber material of a certain bandgap E_g if this light has energy higher than E_g. This excited electron leaves behind a quasiparticle, a hole, in its place. These electrons and holes, once free, are transported through selective contacts or through the absorber itself, to an external circuit before they recombine. Thus, the action of light provides a current through the flow of photogenerated carriers, and a voltage through the difference of the potentials of these hole and electron concentrations, resulting in electrical power.
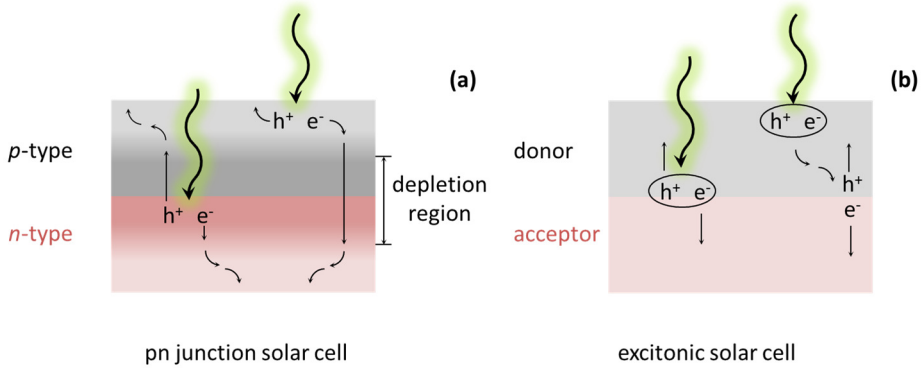
Figure 1.1 The difference between *pn*-junction and excitonic solar cells. The *pn* junction solar cell is comprised of two materials of different conductivity type in contact with each other forming a depletion region (a) which drive free carriers to contacts. Excitonic solar cells (b) have bound electron hole pairs and need an interface to spate these charges.

PV technology can be grouped according to their operation mechanisms, as *pn*-junction solar cells and as excitonic solar cells (Figure 1.1). At the core of *pn*-junction solar cells is the contact of two materials with different conductivity types, one having excess holes (*p*-type) and another having excess electrons (*n*-type). When these two materials are placed in contact, the carriers equilibrate and recombine through the junction such that a region at this interface is free from charge (called the depletion region). This region possesses a built-in field which drives photogenerated carriers to respective contacts; outside of this

3

region, carriers move diffusively before they are collected. The main difference between this type of solar cells and excitonic solar cells is that for the latter, photogenerated carriers remain bound (an exciton). Electrons excited by light are attracted coulombically to the holes they left behind as the absorber material may have weak dielectric constants to screen the charges. As zero-charge species, excitons cannot be acted on by an electric field and can only move diffusively. At an interface, if the energy band offset is large enough, the bound carriers can be dissociated.

Solar cell characterization. As a converter of sunlight to electricity, the most pragmatic way to describe a solar cell is by its power conversion efficiency (PCE), which is the ratio of outgoing electrical power P_{out} and incoming solar power P_{in}:

$$PCE = \frac{P_{out}}{P_{in}} = \frac{J_{max}V_{max}}{P_{in}}$$

where J_{max} and V_{max} are the current density and voltage that leads to the maximum power output.
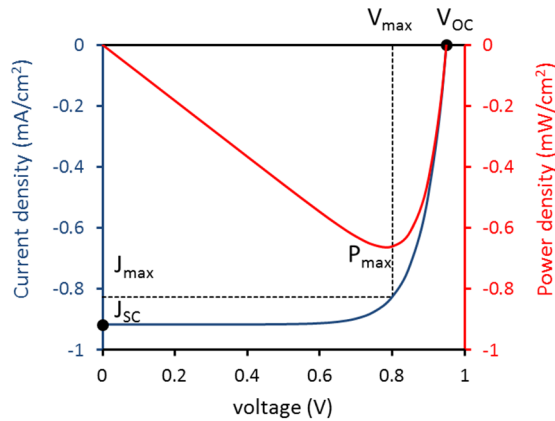
Figure 1.2 Typical current-voltage curve with pertinent figures of merit. Under light, solar cells produce a current and a voltage. The current-voltage curve features important figures of merit such as the short-circuit current density (J_{SC}), the open circuit voltage (V_{OC}), and fill factor (FF from P_{max}), all of which are needed to calculate the power conversion efficiency (PCE).

When no load such as a non-resistive wire is connected to the terminals of a solar cell under illumination (at short circuit conditions), we can measure a

current passing through this wire I_{SC}. Since this current is dependent on the device area, this value is normalized to give the short-circuit current density J_{SC}. On the other hand, when an infinite load is connected to the terminals of a solar cell under illumination, no current flows but a voltage develops (V_{OC}). Therefore, in between these points (0, J_{SC}) and (V_{OC}, 0), at intermediate loads, we will find (J_{max}, V_{max}) leading to the maximum power output (Figure 1.2). The fill factor then is defined as the ratio between the product of J_{max} and V_{max} and the product of J_{sc} and V_{oc}:

$$FF = \frac{J_{max} \, V_{max}}{J_{sc} \, V_{oc}}$$

And the PCE then can be written as

$$PCE = \frac{P_{out}}{P_{in}} = \frac{J_{max} V_{max}}{P_{in}} = \frac{J_{sc} \, V_{OC} \, FF}{P_{in}}$$

Another assessment of device performance is by looking into the probability that a photon of a particular wavelength is converted into extracted electrons, called the external quantum efficiency (EQE):

$$EQE \, (\lambda) = \frac{hc}{q\lambda} \frac{J_{sc}(\lambda) - J_{dark}}{P_i \, (\lambda)}$$

where h, c and q are the Planck's constant, speed of light in vacuum and elementary charge, respectively. J_{SC} (λ) is the short-circuit current density at a particular illumination wavelength λ, J_{dark} the current density in dark conditions and $P_i(\lambda)$, the incident power of monochromatic light. However, not all light might be absorbed in a solar cell due to reflection $R(\lambda)$ and transmission $T(\lambda)$ and the internal quantum efficiency (IQE):

$$IQE \, (\lambda) = \frac{EQE \, (\lambda)}{1 - R(\lambda) - T(\lambda)}$$

can be used instead to adequately evaluate poorly absorbing devices.

With the EQE(λ), it is thus possible to obtain the J_{SC} under sunlight by integrating the product of EQE(λ) and solar photon flux $\Phi(\lambda)$ with incremental changes in wavelengths for all wavelengths.

$$J_{SC} = q \int \Phi \, (\lambda) \, EQE(\lambda) \, d\lambda$$

1.3 Perspectives on traditional and emerging PV technologies

Since the first time PV was discovered by Becquerel in 1839[10], to its first viable commercial demonstration in 1954 at Bell labs[11], up until the present where new materials and architectures are being developed and record PCEs being superseded[12,13], PV research has been working towards, altogether and in part, addressing the challenges pointed out in section 1.1. There are five main technologies for photovoltaics: silicon, thin film metal chalcogenide, organic, dye-sensitized and perovskite, and quantum dot solar cells. We will briefly discuss each of these technologies, highlighting their advantages, challenges, state of the art and working principles.
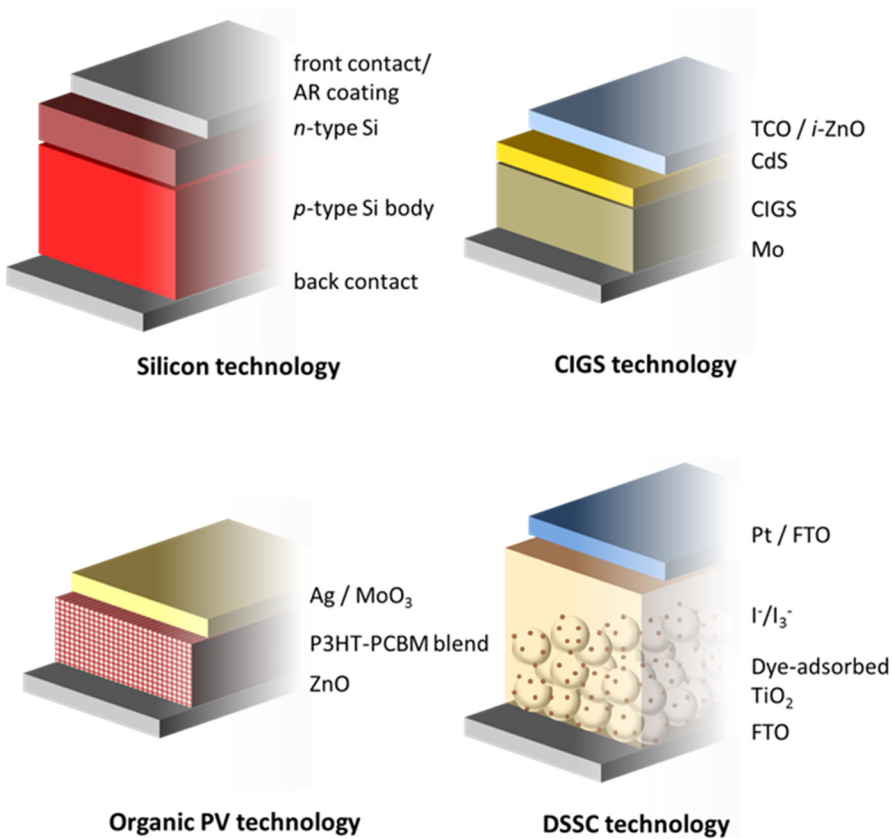
Figure 1.3 Various PV technologies and their device structures. Silicon, CIGS, organic and DSSC technologies all follow a layered architecture: absorber materials are sandwiched between selective contacts.

1.3.1 Silicon and thin film solar cell technology

Silicon technology. Silicon-based PV dominates the PV industry at 90% of the market share[14], as well, apart from GaAs, claiming the highest single junction research cell efficiency at 25% PCE[12]. It is a mature technology and most solar cell characterization and theory[6,15] are based on this material system. In this technology, a *p*-doped silicon wafer, having excess holes, is treated with a surface diffusion of *n*-type dopants, in turn creating a layer with excess electrons and forming a *p-n* homojunction. Silicon has notable electrical properties, having carrier mobilities in the order of 10^2-10^3 cm^2 V^{-1}s^{-1}, controllable doping (10^{14}-10^{20}cm^{-3}), high minority carrier lifetime (~1 ms), high purity and high dielectric constants[16] which makes it an excellent material for PV and electronics. However, silicon-based PV have high fabrication costs, are rigid and require thick absorber layers owing to silicon's low absorption coefficient[17]. This motivates research in looking for alternative material systems.

Thin film solar cells. Thin film solar cells[18], from *p*-type semiconductor absorbers, such as Cu(In$_{1-x}$Ga$_x$)Se$_2$ (CIGS) and CdTe and recently CuZnSnS$_{4-x}$Se$_x$ (CZTS), represent one of the fastest growing sectors in the photovoltaic industry and attempt to address silicon's low absorption coefficient and high fabrication costs. Being direct band gap semiconductors, these materials have high absorption coefficients—or stated in another way, are optically dense. As an example, CIGS has an absorption coefficient of the order of 10^5 cm^{-1} within the range of 500-800 nm[19] while for silicon, it is two orders of magnitude lower[17]. Thus for the same arbitrary amount of absorbed incident light only a hundredth of the thickness of silicon is necessary for these high absorption coefficient materials. These materials, called metal chalcogenides, are deposited via vacuum- or solution-based methods onto metalized substrates, typically molybdenum, after which a thin layer of *n*-type cadmium sulfide, a window layer of *i*-ZnO and a conducting oxide are subsequently deposited. These devices operate via a *p-n* heterojunction.

Device engineering has led to laboratory-scale CdTe and CIGS devices having 21.0% and 20.5% PCEs respectively[12–14]. But despite their continuously reducing market price—at 3.5 €/W for installed CdTe solar cells which is touted to approach grid parity[20]—there are two concerns which serve to weaken the

confidence in devices containing these materials: abundance and toxicity. Both indium and tellurium are rare elements: 160 and 5 parts per billion (ppb) respectively in the earth's crust, comparable with gold at 4 ppb. For this reason, research into CZTS is appealing, being only composed of abundant elements. However, the highest research-cell efficiency for devices based on CZTS is still at 12.6%[12,13] leaving much room for improvement. Further, metal chalcogenide solar cells contain a cadmium sulfide layer which can affect its deployment under various restriction policies, prompting research on novel Cd-free buffer layers[21].

1.3.2 Organic, dye-sensitized and perovskite solar cells

The preceding section discussed on what are termed first and second generation photovoltaics; these technologies operate via a *p-n* junction. While these constitute more than 95% of the market, new technologies are being developed to overcome the shortcomings presented before, such as high fabrication costs, material abundance and in part, toxicity. An additional trait for PV technologies that is attractive for commercial applications is whether materials can be deposited on flexible substrates. These emerging PV technologies (third generation) mainly operate on a different paradigm, using an excitonic mechanism for solar energy conversion and exploit new materials and architectures.

Organic solar cells. Organic solar cells[22,23] are composed of semiconducting conjugated polymers and small molecules. Significant attention was given to this technology when in 1995, solar cells from a mixture of P3HT (poly(3-hexylthiophene)) and fullerene gave a PCE of 2.9%.[24] In this technology, light is mainly absorbed by semiconducting conjugated polymers. Polymers have low dielectric constants and electrons and holes generated from excitation by light remain bound, requiring an interface for them to be dissociated. In polymers, the exciton diffusion length, the average length between generation and recombination, is on the order of tens of nanometers[25]; as such, a blended architecture, wherein an intimately mixed phase of semiconducting polymer and small molecule forms percolating paths, is needed for high performing devices. To date, through changes in material processing and improvements in material properties, a record efficiency of 11.5%[12,13] is achieved. This technology

8

received a lot of enthusiasm, spurring the founding of various companies, mainly due to this technology's appealing features: low fabrication cost, lightweight and its compatibility to roll-to-roll[26] production due to being amenable for deposition onto flexible substrates. These materials however have low carrier mobilities— limiting layer thickness and degrade upon exposure to air and moisture.[27]

Dye-sensitized solar cells. Dye-sensitized solar cells[28,29] (DSSCs), also named Grätzel cells after Michael Grätzel, became a prominent PV technology when in 1991, an efficiency of 7.1%[30] was reported, an unprecedented figure for such cells at that time and even impressive to this date. In DSSCs, light is absorbed by dye molecules which transfer the charges to respective contacts: electrons to an electron conducting oxide, typically TiO_2 and holes to hole-transporting layers such as triiodies or polysulfides in solution or solid-state electrolytes. In these devices, charges do not travel in the absorber dye, but are extracted to their respective contacts as they are photo-generated. For this reason, a mesoporous conducting scaffold, onto which the dyes are adsorbed, is needed to increase dye loading and consequently, the absorption of incoming light. Unfortunately, the PCE of DSSCs has plateaued since its first report in 1991, that after two decades has just reached a value of 11.9%[12,13]. Further, these devices normally contain corrosive liquid electrolytes which pose encapsulation challenges for commercial applications.

Perovskite solar cells. Interest in this technology is renewed with the advent of perovskite solar cells[31,32], which now has taken off as its own body of research. Perovskites are materials with a crystal structure similar to calcium titanate ($CaTiO_3$), where for perovskite solar cells, absorber materials usually are based on methylammonium (MA) lead halides ($MAPbX_3$), where X = I, Br or Cl. A PV device using this material was first reported in 2009[33] with a PCE of 3.8% using a DSSC architecture. Later, it was found that the device would work even without using scaffolds such as TiO_2 or Al_2O_3—that charges could travel through the material and function as a solid-state thin film bilayer heterojunction[34]. Record PCEs for perovskite solar cells are now at an astounding 21.1%[12,13]. The incredible performance of perovskites can mostly be attributed to its relatively high absorption coefficient[31,32], long diffusion lengths (~1 μm)[35] and low exciton binding energies (<16meV)[36]. It also has a relatively

9

facile deposition process, typically employing ambient spin-coating and mild annealing. The technology however suffers from chemical instability and degrades with prolonged light exposure[37]. These solar cells also contain Pb, although efforts have been made to replace it with more benign elements such as Sn[38,39], albeit not performing as well as the Pb-based analogue.

1.4 Brief overview on semiconductor nanocrystals (NCs)

The final PV technology we will discuss and on which this thesis will be focused is on quantum dot solar cells. This represents one of the newest technologies for solar energy conversion but is still largely centered on Pb- or Cd-based materials, encouraging expansion into more benign material systems. But before this, we will first introduce a short section on nanocrystals, their synthesis, properties and applications.

1.4.1 NC synthesis, properties and applications

What are semiconductor NCs? Semiconductor nanocrystals are inorganic semiconducting materials which have sizes typically in the range of 1 to 100 nm. Colloidal nanocrystals (NCs) are simply nanocrystals which are individually suspended in solution, whose suspension is usually aided by ligands attached to their surfaces. To date, advances in colloidal synthetic chemistry has led to a myriad of crystal structures[40], nanocrystal shapes and heterostructures[41,42], spanning simple spheres and polyhedra, to hollow or segmented structures with different material constituents. We also now have an extensive library of nanocrystals of different elemental compositions, accessed by direct chemical synthesis[41,42], cation exchange reactions[43–45] and various doping strategies[46].

Synthesis of NCs. Colloidal semiconductor nanocrystals are typically synthesized in inert environments using Schlenk line techniques. Typically, these materials are synthesized by injecting a decomposable chalcogenide source into ligand-stabilized metal complexes dissolved in a hot organic solvent. There are four steps to any colloidal nanocrystal synthesis[47,48]: nucleation, growth, isolation and post-treatments. To obtain monodisperse products: particles with a small size distribution, it is important to separate the nucleation and growth events such that all particles will have similar growth history. Spontaneous nucleation is induced by a supersaturation of the solution of reactive monomers whereas

10

growth is a diffusion-controlled process of monomers precipitating and redissolving at the interface of formed crystals and the solution. These events occur simultaneously but ongoing nucleation is suppressed through fast consumption of monomers by a nucleation burst. This burst of nucleation is achieved either by a swift injection of monomers or the decomposition of monomers in unison at a particular temperature. During growth, there are two regimes: at high monomer concentrations, the size distribution is focused as smaller nanocrystals grow faster by diffusion than do larger crystals; at low monomer concentrations, the size-distribution is defocused (Ostwald ripening) by dissolution of smaller crystals and growth of larger ones. Thus it is equally important to control nanocrystal growth. The growth process is ended by quenching the reaction and removing the products by isolating them from the reaction. This is performed by repeated cycles of precipitation and redispersion in anti-solvents and solvents to remove any unreacted precursors. Finally, optional post-treatments may be performed to encase the nanocrystals in a shell of another semiconductor[42], to tune the material composition by cation-exchange[45] or to change surface ligands to modify surface properties[49].

Properties of NCs. The size of these semiconductors gives rise to interesting properties. The most striking of these is in changes in its optical properties. The exciton has a physical size, the exciton Bohr radius. If the crystal size is smaller than the exciton Bohr radius, more energy is needed to create the excitons. The charges become confined quantum mechanically and can be treated as particles in a box, having discrete energy levels with the size of this box relating to nanocrystal size. These semiconductor nanocrystals are termed quantum dots (QDs). For example in CdSe[50], the band gap was tuned from its bulk value of 1.7 eV to 3.0 eV with corresponding changes in emission. The high surface to volume ratio of these materials points to the increased importance of the surface: for example, band edge levels can be shifted with appropriate ligand choice[51] and that the degree of surface passivation should be managed[52,53]. These materials also show deviating thermal properties such as a depressed melting point as compared to the bulk because of higher solid surface energies[41] and a lower thermal conductivity due to phonon scattering at the surface[42]. Another exciting phenomenon is that of carrier multiplication[54], wherein a high energy photon generates two excitons instead of one as it is posited that the

11

crystal size restricts cooling by lattice vibrations. Finally, the more pragmatic property that emerges from colloidal semiconductor nanocrystals as compared to the bulk is that they have better processability being already crystallized and in solution. Whereas, bulk semiconductors traditionally employ high temperatures or vacuum processes for their fabrication, colloidal semiconductor nanocrystals lend themselves to other ambient, low temperature and low cost deposition technologies such as spincoating, dipcoating and spray coating.

Applications of NCs. Because of these interesting properties, these materials have been used for the development of various applications such as in biology[55], thermoelectrics[42] and optoelectronics[42,56,57]. These materials have length scales comparable with biological materials and do not easily photobleach. As such, they have been used as markers to probe biological processes through their photoluminescence[55]. Also, as these materials usually have a well-defined emission peak, it is possible to multiplex signals which is difficult for organic emitters with broad emissions. Further, having a lower thermal conductivity results in higher thermoelectric efficiencies[42] leading to a promise of better thermoelectric devices. Finally, high photoluminescence quantum yields and their bandgap tunability have piqued interest for use in efficient light emitting diodes[56,57].

1.4.2 NC solar cells

With the properties stated above, such as bandgap tunability, band edge position modification, controlled composition and doping, the possibility for multiple exciton generation and good processability, it comes to no surprise that these materials will find use as absorbers in solar cells[58–61]. There are two main classes of semiconductor nanocrystalline solar cells: semiconductor sensitized[58] and colloidal quantum dot (CQD) solar cells[59].

Semiconductor-sensitized solar cells (SSSC). Semiconductor-sensitized solar cells[58] have the same structure and operating principle as dye-sensitized solar cells, however, instead of a dye, use semiconductor nanocrystals. They bypass the high cost of dyes which are often ruthenium-based complexes. Like dye-sensitized solar cells, charges are not expected to travel in the absorber and thus a thin layer of semiconductor nanocrystals are adsorbed by infiltrating NCs with bifunctional ligands or grown in-situ by chemical bath deposition on the TiO_2

12

scaffold. These cells use polysulfide electrolytes as triiodide electrolytes etch the semiconductor nanocrystals. The highest reported efficiencies to date is based on $CuInSe_2$ and $CuInS_2$ quantum dots at 11.6%[62] and 7.0%[63] PCEs respectively. As with DSSCs, the commercial applications of these remarkable efficiencies are held back by the use of liquid electrolytes.

Fabrication of CQD film. The developments in solid-state colloidal quantum dot solar cells can be attributed to, along with the synthesis of monodisperse high quality nanocrystals[64], the deposition of functional optoelectronic films[51–53,59,65–67]. These films are deposited from solution onto a flat conducting substrate through various solution coating methods such as spincoating. The nanocrystals are stabilized in solution by long organic ligands which act as insulators and a barrier for charge transport. Reducing this inter-dot spacing between nanocrystals increases the carrier mobility and therefore the conductivity in these films[68]. This process of ligand removal/replacement is called a ligand exchange process; the protocol to perform this process in the solid state is through the layer-by-layer (LbL) process wherein (1) a QD layer of uniform thickness is deposited, (2) new ligands in an anti-solvent is reacted with the film, (3) the film is washed with anti-solvent to wash away reactants and by-products and (4) the film is washed with the original NC solvent to wash away uncreated particles. Steps (1)-(4) constitute one cycle of the LbL process and give fine control over the film thickness.

Electronic considerations for the CQD film. For this film to perform well in an optoelectronic device, several electronic properties have to be taken into consideration[59]: its carrier mobility, trap density, carrier life time (diffusion length), doping, band edge levels and stability. These materials can be viewed as polycrystalline analogues of monocrystalline films. Mobilities in the range of 10^{-4} $cm^2V^{-1}s^{-1}$ from PbS films treated with short organic ethanedithiol (EDT) to 10^{-1} $cm^2V^{-1}s^{-1}$ from those treated with inorganic halide ligands can be obtained[69] and can even reach as high as 10^2 $cm^2V^{-1}s^{-1}$ for HgSe films[70]. While it might seem logical to increase mobility to as high as possible a value, doing so will only increase the probability of charges encountering traps[71]. Most traps appear during the LbL process as passivating ligands desorb from the surface, as such a judicious surface passivation is needed[72,73]. In the absence of an extracting field, charges must be able to diffuse towards collectors before they recombine; the

diffusion length is dependent on mobility and carrier lifetime, therefore these parameters can be controlled to affect performance. It has been found that by increasing the diffusion length from 70 ns to 230 nm, arising from a two-fold and eight-fold increase in carrier lifetime and mobility respectively, efficiencies of upwards of 9% can be acheieved[74]. The carrier type[73,75], as determined whether the Fermi level is closer to the valence or conduction band, and band edge positions[51] are necessary parameters for the band energetics dictating carrier flow in the device and has been controlled by surface treatments and heterovalent atom inclusions. Finally, these devices should show stability during operation. By appropriate ligand choice and mild post-treatment annealing[65,72], no changes in performance was found after 150 days in storage or 1000 hours or continuous illumination.

CQD solar cells and architectures. Colloidal quantum dot solar cells, mostly based on PbS, have reached impressive PCEs in a little over a decade from proof of concept devices (PCE ~ 0.01%) in 2005[76] to more than 10% in 2016[77]. These developments have come from an understanding of the material and electronic properties discussed above as well as the device operation and the experimental solutions that address or improve on them[59]. In terms of operation, CQD solar cells operate in the same way as first and second generation solar cells, employing a *pn*-junction for energy conversion, which necessitates the same considerations of the electronic properties of the semiconductor film. Excitons in a PbS CQD film for example are easily dissociated with a 40 meV exciton dissociation energy[78]. However, due to low mobilities, carrier lifetimes and thin depletion widths (~200nm)[79], these devices share similarities with excitonic solar cells, having a strong compromise with collection length and absorption thickness. These limitations have been attempted to be addressed by changing the device architecture[59] to which solution processing easily lends itself. The main architectures are the Schottky, depleted heterojunction and bulk heterojunction solar cells.

The Schottky cell is one of the simplest solar cells, where a Schottky contact—a rectifying contact between a metal and a semiconductor due to the formation of a potential by migration of carriers from semiconductor to metal—is present. In *p*-type colloidal semiconductor films, Schottky contacts are formed with metals with low work functions; after equilibration, this creates

14

a potential barrier for hole flow and an incentive for electron flow at the interface. Current record efficiency for this device architecture is at 5.2%[80]. However, thin depletion widths (50-100 nm)[81–83] , Fermi level pinning limiting the open circuit voltage (V_{oc}) and illumination of the junction at the back contact[74] are hindrances for this architecture.

These problems can be abated through the design of the depleted heterojunction[79]. In these devices, two semiconductors of different compositions and conducting type are brought in contact such that they form a Type II staggered junction—the valence and conduction bands of the *p*-type semiconductor each are higher than those of the *n*-type semiconductor—and that their respective carriers migrate to create a region that is free of carriers at the interface (depletion region). Indeed, this creates a larger built-in potential and allows the junction to be placed closer to the incident illumination if a thin transparent *n*-type semiconductor like TiO_2 is chosen. These answer the problems present in the Schottky device configuration and along with improvements on the CQD film properties, lead to devices with the highest efficiency for CQD solar cell technology at 10% in 2016[12,77].

However, minority carrier diffusion lengths, at 70nm, still limit device efficiency by compromising the absorber thickness. One way to overcome this is through a bulk heterojunction structure. Similar to organic solar cells, the device is enabled by an intimate contact of two materials, bringing carriers close to the depletion region instead of a dissociating interface. This structure is achieved either by infiltrating a porous oxide network with the CQD[84,85] or creating a solution containing both *n*- and *p*-type nanocrystals which are then processed into a film[86,87]. Six-fold improvements in short circuit photocurrent density (J_{sc}) was achieved compared to its planar analogue are seen when Bi_2S_3 was mixed with PbS[86]. While the increase in J_{sc} through nanostructuring is undisputed, V_{oc} and fill factor (FF) varies: increasing in one report[87] due to the passivation of traps by the complementary material and decreasing in others[84], as suggested due to increased bimolecular recombination at interfaces. Despite the lower performance of this architecture, at 6%[85], this structure can pave the way to using even materials with low diffusion lengths and high trap density.

Colloidal quantum dots allow for facile control over the architecture of solar cells, at the moment showing rapid increase in efficiency. This technology

however contains Pb and can raise concerns on its regulatory acceptance. This motivates us to develop new non-toxic materials for CQD solar cells.

1.5 Non-toxic nanocrystals for photovoltaics

While the toxicity of nanomaterials can also be due to their size, having a comparable size scale with biochemical molecules, we refer to non-toxic nanocrystals as that having no toxic elements such as lead, cadmium or mercury. Research on the use of non-toxic nanocrystals for photovoltaics can be grouped into three categories: (1) NC-annealed film, (2) SSSCs, (3) CQD solar cells, employing various nanocrystals containing non-toxic elements: CZTS [88–92] (E_g = 1.5 eV), InP[93] (1.34 eV), Sb_2S_3[94] (1.55 eV), Cu_2S[95] (1.21 eV), Bi_2S_3 [96–98] (1.4 eV), $AgBiS_2$ [99] (1.3 eV), Zn_3P_2[100] (1.5 eV) and FeS_2 [101–106] (0.95 eV). A separate section on $CuInS_2$ (1.55 eV) will follow after this.

NC-annealed film. The synthesis of CZTS[88] nanocrystals, first reported in 2009[89,90], started the research into using this benign nanomaterial for solar energy conversion. As discussed in the preceding section, CZTS was born out of CIGS technology in the hopes of using more abundant materials; and like its bulk counterpart, CZTS nanocrystals employ a CdS layer to form a heterojunction and undergo an annealing or selenization step [89,91,92], with a record efficiency of 7.7%[91] close to its thin film analogue. When no annealing is performed, the device performance is low at 0.23% PCE[89].

Non-toxic SSSCs. Semiconductor sensitized solar cells were originally largely based on CdSe[58] but now include non-toxic alternatives such as InP, Sb_2S_3 and $CuInX_2$. In fact, CdSe has been superseded in PCE by $CuInSe_2$ at 11.6%[62]. CQDs of indium phosphide doped with tin adsorbed onto a mesoporous TiO_2 network with a liquid electrolyte has led to a PCE of 3.5%[93]. In the solid state, Sb_2S_3-sensitized TiO_2[94] has led a PCE of 5.13% using P3HT as a hole conductor.

Non-toxic CQD solar cells. CQD solar cells demand a high-quality CQD film for devices to perform well and mostly have been fulfilled by PbS QDs. Flexible, albeit not completely non-toxic, non-annealed solar cells from cuprous sulfide (Cu_2S), a precursor to CIGS technology, have been made with CdS nanocrystals at 0.23% PCE. Hybrid solar cells using Bi_2S_3 nanocrystals and P3HT have been developed, starting from a PCE of 0.46% for planar bilayer

16

devices[96] to a more than two-fold increase in PCE at 1.1% with material blending[97] and additional thiol functionalization of the conducting polymer[98]. Bi_2S_3 NC films suffered from low mobilities ($\sim 1 \times 10^{-5}$ $cm^2V^{-1}s^{-1}$) and short carrier lifetimes (5 ns)[96] and therefore benefitted from a blended architecture. Recently, a new colloidal semiconductor nanocrystal, $AgBiS_2$, has been reported showing a certified PCE of 6% at its debut[99]. This material is sandwiched between ZnO and a conjugated polymer (PTB7). It is impressive that with a thickness of less than 50 nm, this material results in solar cells with a J_{SC} reaching 20 mA/cm^2 and an EQE reaching 80%. These devices were fabricated in air and both the solution and completed devices result in stable performance even after storing in air for more than 30 days.

Non-toxic NC solar cells being developed. There are two materials, Zn_3P_2 and FeS_2, which have yet to show photovoltaic effects in completed devices. Sandwiched between ZnO and MoO_3, the Zn_3P_2 device[100] rectified but did not show any photovoltage nor photocurrent under light. It did show that it responded to light, with an on-off ratio of 2. Together with a survey of materials balancing projected power output and material abundance[101] and the report of the synthesis of FeS_2 NCs[102,103], FeS_2 NCs received exposure as the next promising material for solar cells. As with Zn_3P_2 however, devices from this material still have not shown any photovoltaic effect, only showing photoconductance[106]. Even for single crystals, FeS_2 has shown poor performance, particularly having low V_{oc}, which has been attributed to a large number of defects in the bandgap[104,105].

1.6 $CuInS_2$ nanocrystals: current trends and prospects

Among non-toxic nanocrystal alternatives, with more than 100 papers since 2011[107], copper indium sulfide $CuInS_2$ (CIS) has been one of the most researched material partly due to its proven promise in the bulk with 20.5%[12,13] PCE for CIGS and 11.4%[108] for thin film $CuInS_2$, a large stoichiometry tolerance from the low enthalpy of formation of neutral defect pairs ($2V_{Cu}^-$, In_{Cu}^{**})[109], a broadly tunable bandgap with high quantum yields[110–112] and the possibility of multiple exciton generation[113]. Various through and excellent reviews have collated the range of syntheses and applications for CIS QDs.[107,114–116] Two distinguishing features surface in these reviews: that CIS is

mostly synthesized using dodecanethiol (DDT) and that for solar cells, CIS is used as a sensitizer to TiO_2 in an SSSC configuration. The general synthesis scheme for DDT-based synthesis is to dissolve indium and copper salts in DDT; this solution is then heated up to more than 200°C where DDT begins to decompose releasing sulfur into the system. DDT performs many roles in this synthesis of CIS NCs: to act as solvent, to provide the sulfur source, to control the reactivities of Cu and In and to stabilize the nanocrystals in solution. This facile synthetic scheme and the multifunctionality of DDT have made it popular for the synthesis of CIS NCs.

For solar cell applications, CIS NCs have been used in all three kinds of devices, as an NC-annealed film, as a sensitizer in SSSCs and a CQD solid. Solar cells from NC-annealed films borrow heavily from its thin film analogue, using annealing[117–119] or selenization and using CdS[120–124] as a buffer layer. The CIS NC solution is treated as a precursor ink, which is recrystallized and grown to form the bulk thin film with 8.2% PCE from multiphase nanoparticles[125]. Using CIS NCs in this way however, waives both the cost-effectiveness and adaptability provided by the colloidal nanocrystal platform, and also the low toxicity of the elements in CIS nanocrystals. CIS NCs have been employed as sensitizers in liquid junction solar cells[63,126,127] with a highest efficiency of 7%[63] and at 11.6% for its selenide analogue[62]. This remarkable performance is in contrast to those of quantum dot solid-state solar cells, which for unannealed films has shown more modest efficiencies of 0.2%[117–119], only reaching 1.5% for annealed ones[123]. In high performing architectures: in annealed films and in SSSCs, CIS has been treated to improve film quality or used as an absorber film that does not facilitate charge transport.

For $CuInS_2$ nanocrystals to be added to the repertoire of nanomaterials in solar cell technology based on CQD solids as a non-toxic alternative, it is first important to fabricate conductive and photoconductive solution-processable films. DDT has been noted to be difficult to remove from the surface[63,110]; this hinders film formation via the LbL process and highlights thus the performance gap between devices with CIS as sensitizers and those with CIS as a quantum dot solid. Further, a device architecture which does not utilize CdS, then, has to be developed; this includes an appropriate n-type material that matches the energy band diagram of CIS and the design of a proper device configuration.

18

1.7 Thesis objectives

Current CQD technology is dominated by PbS; CIS NCs present themselves as non-toxic alternatives. The goal of this thesis then is to address the challenges that are set before CIS for its application as a CQD solid absorber in solar cells. We aim to do this by tackling the following issues:

Processability of CIS NCs: There is a gap between the performance of annealed CIS or CIS used as sensitizers and current CIS CQD film. This necessitates the formation of high-quality CQD films. We aim to develop a ligand exchange protocol to form photoconducting CQD films. This may entail the rational choice of replacing ligands or the omission of DDT in the synthesis.

Device architecture for CIS CQD solar cells: Most CIS films use CdS as a buffer layer; these devices do not deviate from the architecture of thin film metal chalcogenide PV. We aim to design and optimize a suitable device architecture that will enable CIS CQD films to perform in a photovoltaic device.

Limitations of the CIS CQD solar cell: The properties of the CQD film are significant considerations for CQD PV technology. As well, much of the advancement in the field has been brought about by an understanding of the device operation. We aim to identify the operating mechanisms of CIS CQD solar cells and to characterize the properties of the CQD film that hinder its performance.

1.8 Thesis outline

In view of these objectives, this thesis is organized as follows:

Chapter 2: We introduce a synthetic scheme that does not incorporate DDT. While we have found it possible to exchange DDT with shorter ligands, it required harsh conditions to do so. Thus we saw it necessary to go back to the synthesis and modify it. DDT performed many roles and we had to select various molecules to fill in the roles it left behind. By the end of this chapter, we present a synthesis of CIS with tunable sizes and emission, a

model of the particle composition and a ligand-exchange strategy to form films.

Chapter 3: We characterize the CQD films and fabricate optoelectronic devices. We aimed to incorporate the CIS CQDs into solar cells as absorber films, but to do this, we first had to characterize these films, measuring its mobility, carrier concentration, photoresponse, among others. We did this by making preliminary optoelectronic devices. This chapter closes with describing solar cells made out of the CQD solid and its limitations.

Chapter 4: We design a bulk heterojunction and pinpoint the issues influencing performance. The bulk heterojunction is a useful platform for utilizing materials with poorer electronic properties. We engineer a structure by modifying porosities to allow infiltration of CIS into an oxide layer. This works ends with a report on changes in performance and their causes and a proposal for the operating mechanism of solar cells made from this material.

CHAPTER 2
Thiol-Free Synthesis of CuInS$_2$ Nanocrystals for Solution-Processable Films[a]

   In the previous chapter, we proposed copper indium sulfide CuInS$_2$ (CIS) as a viable alternative to PbS in colloidal quantum dot photovoltaics, owing to it not being composed of toxic elements, having proven good photovoltaic performance in the bulk[108] and in sensitized solar cells[63], having a broadly tunable bandgap with high quantum yields[110–112] and having the possibility of multiple exciton generation[113]. We also noted that there is a discrepancy between the exciting efficiencies seen in annealed films, in those used as sensitizers at 8.2%[125] PCE and at 7.0%[63] PCE respectively and in those wherein CIS is used as a colloidal quantum dot solid (CQD), at 0.2%[117,119] PCE. It is crucial therefore to investigate the formation of high quality CQD films to close the gap in performance between these architectures. In this chapter, we will initially undertake an attempt to process CIS nanocrystals (NCs) synthesized using schemes from the literature into solid state films. Consequently, we have found it difficult to remove DDT from the surface and found it necessary to redesign the synthetic scheme using other ligands. The rest of this chapter will discuss

---

the material properties of the products from this synthesis and close with a ligand exchange strategy to form solid-state CQD films.

2.1 Attempt at the removal of DDT from the surface of the nanocrystal

Copper indium sulfide nanocrystals are nanomaterials of active research, whose synthesis, properties and application have been extensively covered in 5 reviews,[107,114–116,128] in just 3 years prior. In these reviews, it can be gleaned that a majority of the synthetic schemes utilize dodecanethiol (DDT), stemming from the early reports from the Scholes[111], Klimov[112] and Peng[110] group. This method results in highly monodisperse, broadly emitting, high photoluminescence (PL) quantum yield materials with long PL lifetimes[110–112].
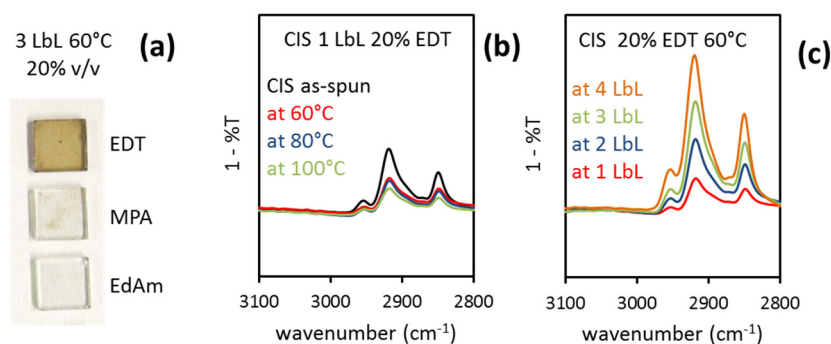
Figure 2.1 DDT removal from CIS synthesized based on literature. (a) Images of films deposited using different ligands (ethanedithiol EDT, mercaptopropionic acid MPA and ethylenediamine EdAm) to remove DDT on particles synthesized using recipes from literature. (b, c) FTIR spectra using different deposition conditions with EDT. With EDT, harsher conditions do not remove DDT completely (b) and that while films build, there is still a lot of organic residue (c).

We followed the synthesis described by Zhong and Scholes.[111] This synthesis involves the decomposition of DDT in a solution of copper iodide, indium acetate, octadecene and oleic acid at 200°C. Upon reaching the target temperature, the solution turned from a clear yellow solution to orange, to red and then to black: indicating the growth of the particles, moving through different confinement sizes. With the isolated and cleaned solution, we attempted to deposit films via the layer-by-layer (LbL) process as discussed in Chapter 1 using ligands with various functional groups: ethanedithiol (EDT),

mercaptopropionic acid (MPA) and ethylenediamine (EdAm) for thiols, carboxylic acids and amines respectively (Figure 2.1a). We found that EDT led to films that built up, as evidenced by darkening of the film, with increasing layers. This process however involved harsh conditions, at 20%v/v of the ligand in acetonitrile and at elevated temperatures, whereas for PbS-based devices the LbL process is conducted at room temperature at <1% v/v concentrations.[59]

We performed Fourier transform infrared spectroscopy (FTIR) to probe the extent of ligand exchange on these films by looking at the C-H stretching (Figure 2.1b and c). Much of the native ligands remain (we acknowledge that EDT also has some C-H stretching) even at more aggressive conditions of 80°C and 100°C (Figure 2.1b). This residue is present in the CIS film itself as the C-H stretching increases with increasing layers (Figure 2.1c). The difficulty of removing DDT on the surface has been noted by other groups[63,110], leading to further work on treating the surface to remove the organic shell[129] or to use shorter thiol ligands during synthesis.[130] It can be suggested that the difficulty of removing the thiol on the surface is due to the thiol participating in a crystal-bound or X-type ligand coordination mode[131,132]. In light of these results, we therefore found it vital to develop a NC synthesis that does not employ thiols as a ligand or sulfur source.

2.2 Developing a synthesis without DDT

In Chapter 1, we presented an overview of CIS NC technology and mentioned that DDT performs many roles in the synthesis: to act as solvent, to provide the sulfur source, to control the reactivities of Cu and In and to stabilize the nanocrystals in solution. In the hard soft acid base (HSAB) theory, the Cu ion is considered a soft acid and has strong affinity with trioctylphosphine (TOP). In fact, for cation-exchange reactions, TOP is used to facilitate the removal of Cu in nanocrystals[45]. We begin with a synthesis using copper iodide (CuI) and indium chloride (InCl$_3$) as the metal salts, TOP and oleylamine (OlAm) as ligands and octadecene (ODE) as the solvent with bis(trimethylsilyl) sulfide (TMS) as the sulfur source. Concomittantly, in a similar system, Allen and Bawendi[133], had reported a DDT-free synthesis, using TOP and OlAm and bis(trimethylsilyl) selenide for CuInSe$_2$.

With this as a starting point, we aimed to understand the effects of the TOP and OlAm on the synthesis. We found through control synthetic experiments that TOP inhibits the reactivity of copper (Figure 2.2a) while OlAm inhibits the reactivity of indium and uncontrolled NC growth (Figure 2.2b). When the amount of TOP is reduced, the material begins to show plasmonic absorption past the bulk bandgap (Figure 2.2a), indicative of increased free carrier absorption. It has been reported that copper-rich CIS are plasmonic[134] and that the incorporation of In atoms dampens the plasmon peak in Cu_2S nanoparticles[135]. Together with the fact that the absence of TOP results in the presence of $Cu_{2-x}S$ signals in the Raman spectrum (~470 cm^{-1}), these point to TOP controlling the reactivity of copper. As to the role of OlAm, indium-rich red particles around 200-400 nm in diameter, precipitate out of solution when OlAm is removed (Figure 2.2b). This occurs even when TOP is present or when oleic acid (OA) is used in its place. This points to OlAm as being crucial to control the reactivity of indium as well as the size of the particles and that the combination of TOP and OlAm provide a balance in the reactivities of Cu and In to form CIS nanoparticles.

Reduction of TOP content (a)   Reduction of Olam content (b)

	OATOP	TOP	TOP-Olam
Cu	0.25	0.18	0.50
In	1.51	1.42	1.36
S	2.24	2.39	2.14
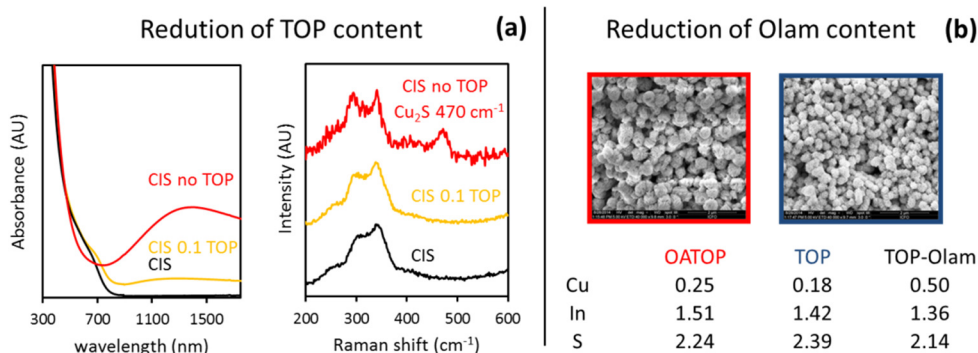
Figure 2.2 Effects of TOP and OlAm on CIS nanocrystals during synthesis. (a) UVVis and Raman spectra of CIS with different TOP content. The reduction of TOP leads to plasmonic and Cu_2S Raman features, indicating that TOP controls Cu reactivity. (b) SEM images and compositions by EDX of CIS with various TOP content. The absence of OlAm leads to larger and In-rich particles, suggesting that it controls that of In instead.

The as-synthesized crude product, which we can call CIS-OlAmTOP, however is chemically and colloidally unstable. Over time, it reduced in

24

photoluminescence lifetime, consequently the photoluminescence quantum yield (PLQY), and increased in free carrier absorption (Figure B1a, b). It has been known that excess oleylamine either etches the NCs[133] or promotes the catalytic oxidation of nanocrystals[110]. The excess oleylamine however cannot be removed from the solution as these particles become insoluble after multiple precipitation and redispersion.

To make these chemically stable and dispersible, we treated these particles with zinc oleate. The crude product is reacted at specific temperatures with a pre-prepared ODE solution of zinc oleate from zinc acetate dihydrate and oleic acid (Appendix A, Table A1). After this treatment, these particles, kept in a glovebox, remain soluble and show little loss in their PLQY even after a year (Table B1). Zinc treatment of CIS NCs has been known to blue-shift the absorption spectrum due to the formation of shells[136], to increase PLQY and lifetime by reduction of the short lifetime component by surface passivation[112] or to form alloys of copper indium zinc sulfide as seen in shifts in the X-ray diffractograms[137]. We see all of these effects in our nanocrystals: Zn-treated particles, CISZn-OA, have more pronounced blue-shifting for smaller nanoparticles (Figure B1c), PLQY increases from 10.8% to 24.4% (Figure B1d), and that X-ray diffraction peaks upshift (section 2.3).

In trying to omit DDT from the synthesis of CIS NCs, five molecules were introduced to substitute the functions it performed: ODE, as solvent; TOP and OlAm, as ligands to control the cation reactivities; TMS, as sulfur source; and OA (subsequent after Zn-post-treatment) as stabilizing ligand.

2.3 Control on the absorption and photoluminescence of CIS

Upon injection of the sulfur source, the reaction solution changes from clear to yellow, to orange, to red and then finally to black at injection temperatures of 170°C. Indeed, when we inject the sulfur source at lower temperatures, we are able to obtain the products at stages before they reach their bulk bandgap. The absorption and photoluminescence of CISZn-OA then can be controlled, shifting to shorter wavelengths with lower synthesis temperatures. The bandgap of these materials, calculated from the Tauc plot[110,111] (Figure B2a), can be tuned from its bulk value of 1.54 eV (synthesized at 170°C) to a confined value of 2.51 eV (50°C) (Figure 2.3a and b). For

completeness, other measures of the bandgap by other definitions, such as the excitonic peak[112] or the sharpest onset were calculated; a comparison of these values is shown in the Appendix (Figure B2). These absorption profiles have a broad excitonic peak[b] that appears as a shoulder. If intrinsically, NCs have sharp excitonic peaks, a wide size distribution would broaden these peaks. However, despite having narrow size distributions, CIS NCs have also been reported to lack an excitonic peak[110–112]. Other reasons as to the origin of this broad absorption peak can been attributed to (1) slight variations in nanocrystal shapes, (2) to differences in nanocrystal to nanocrystal composition or (3) to a distinct electronic feature inherent to CIS NCs due to an overlap of near edge transitions[110]. From theoretical models, Shabaev et. al. calculated that hole levels near the band edge in CIS contribute to long absorption tails which lessen for smaller NCs[138]. In this synthesis, we observe a distinguishable excitonic peak for materials synthesized at lower temperatures (Figure 2.3a). This supports the prediction by Shabaev or might simply mark a size regime of stronger quantum confinement—as CIS synthesized at 170°C has a bandgap close to its bulk value already.

These materials are luminescent, with full width at half maximum (FWHM) ~132 – 142 nm and large Stokes shifts in the range of 130 – 160 nm, having smaller shifts for smaller bandgaps (Figure 2.3c). Photoluminescence quantum yields (PLQY) can reach 24% (Table B1) with average PL lifetimes of 0.27 μs (Figure B3). While these NCs have quantum yields lower than the highest reported value of 80%[112], they exhibit one of the higher PL lifetimes among those previously reported (140-190 ns)[26,112]. Further, the photoluminescence excitation spectra of samples probed at short and long wavelengths of the emission spectrum (see Figure B3), overlap well with the absorption spectra. This suggests that the nanoparticle solution contains an emitting species with a single modal size distribution.

---

[b]   The position of the excitonic peak is calculated from the zero value of the first derivative of the absorption spectrum with wavelength or its absolute minimum if first derivative does not reach a zero value.
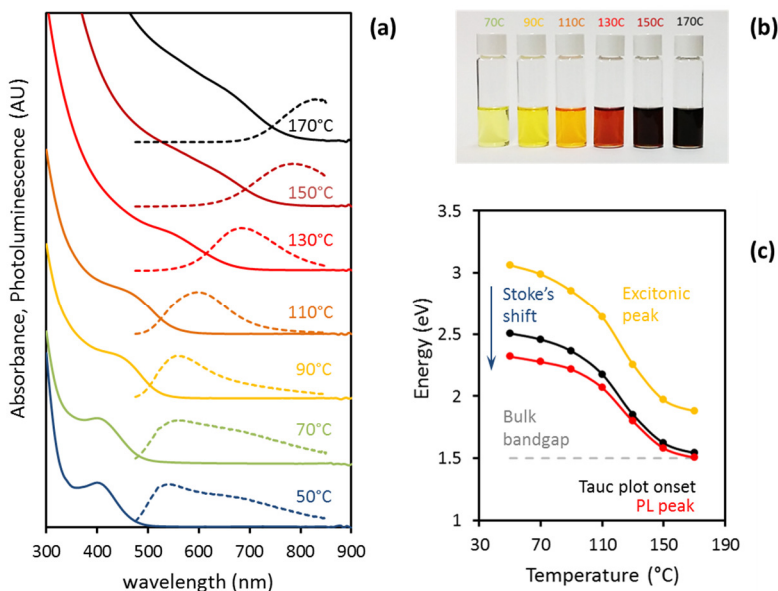
Figure 2.3 The optical properties of CIS quantum dots can be tuned. (b) The absorption (solid lines) and emission spectra (dashed lines) of CIS synthesized at different injection temperatures. The spectra are shifted for clarity. (b) Photograph of CIS-ZnOA nanocrystals showing changes in color. (c) Calculated bandgap from the Tauc plot onset, PL peak and excitonic peak positions showing Stoke's shifts.

The origin of the emission of CIS NCs is still highly disputed in the community[115,139]. Initially, due to broad emissions, large Stokes shifts and long PL lifetimes, the photoluminescence has been attributed to the emission via a donor-acceptor pair[110,140,141]. This argument has mostly been disregarded to date partly because of the extent that the emission peak position can be tuned (>1eV). It is likely that these photoluminescence properties, instead originate from donor-level to quantized-valence band[112], quantized-conduction band to acceptor-level transitions[142,143] or from the inherent band structure of chalcopyrites[138]. We will touch upon this topic again under further experimental evidence in the subsequent chapters.

2.4 Size distribution and crystallinity of products

CIS can occur in three crystal structures: hexagonal wurtzite WZ, cubic zincblende ZB and tetragonal chalcopyrite CP, with CP being the thermodynamically stable phase at room temperature in the bulk. Even so, WZ

and ZB phases have been reported to exist in nanocrystalline form[144,145]. This is possible as nanocrystals allow access to phases normally unstable at room temperature and pressure due to the amount of strain the nanocrystal is exposed to because of its size. The X-ray diffractograms of materials synthesized at different temperatures (Figure 2.3a[c]) indicate a crystal structure that is either cubic or tetragonal. It is difficult to distinguish between these crystal structures but we believe these particles are in the cubic phase as (1) these particles lack the reflection lower than 15 Å^{-1} (Figure B4[d]) which is a characteristic peak for chalcopyrite[145] (JCPDS 85-1575) and as (2) these particles have a marked off-stoichiometry than 1:1:2 for Cu, In and S, as will be covered in section 2.5. The cubic structure has equal lattice constants, and therefore allows for flexibility in stoichiometry, with Cu and In being randomly ordered in the cation sites.[144] These diffractograms also exclude the possibility of the formation of $Cu_{2-x}S$ and β-In_2S_3 in the product.   Notice that the line widths of the parent peak at (111) in wide angle X-Ray diffractograms, obtained using a synchrotron source (Figure 2.4a), increase with decreasing synthesis temperature. Using the Schrerrer equation:

$$D_p = \frac{2\pi\,K}{FWHM_Q}$$

where D_p is the crystallite diameter, K is a shape factor taken as 0.9 and $FWHM_Q$ is the FWHM of the diffraction peak, we obtain diameters ranging from 2.0 nm to 3.3 nm, coinciding with a size calculation of 3.2 nm from XRD data using a table top source.

These changes in size can also be seen in shifts in the small angle X-ray scattering (SAXS) diffractograms (Figure 2.4c), shown in d-spacing as $2\pi/Q$. As we move from higher to lower Q values, we move from smaller to larger lattice constants and consequently d-spacings. Therefore, when observing very

---

[c] shown in Q (Å^{-1}), where Q = 4π/λ *sinθ* with λ = 0.1 nm

[d] Figure 2.4a shows features at around 15 Å^{-1}, but these are artefacts of baseline correction as this is at the edge of the WAXS data collection.

small angles, as in SAXS, we probe large-scale ordering. The samples are drop-casted films so when dried, nanocrystals assemble into an ordered structure if these particles have a narrow size distribution. These peak positions therefore relate to changes in NC size and to an extent, the monodisperisity of samples.
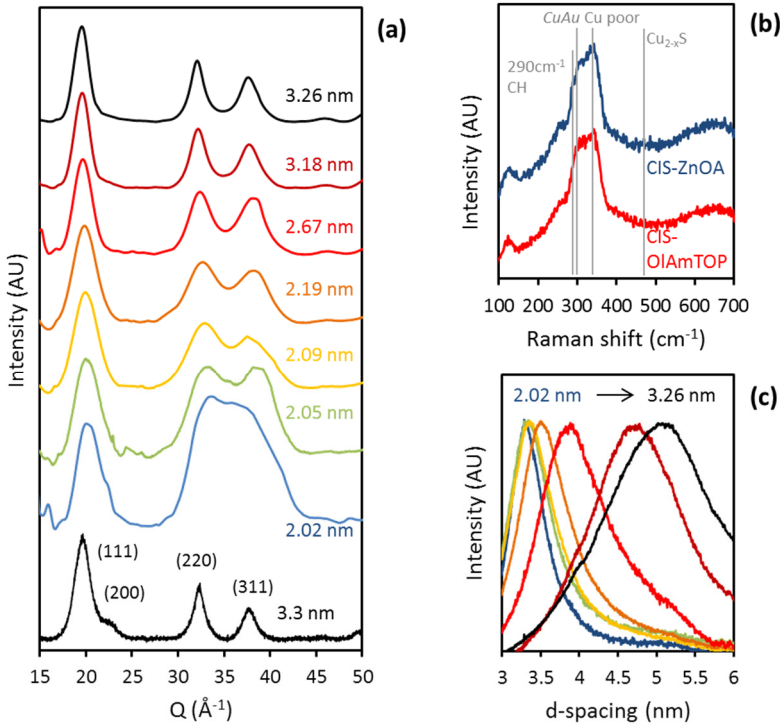
Figure 2.4 Structural properties of CuInS$_2$ nanocrystals. (a) XRD data from a synchrotron source and from a tabletop equipment (bottom-most) showing cubic peaks and peak broadening. Calculated diameters are placed in-figure and colors correspond to synthesis temperatures, from blue, 50°C to black, 170°C. (b) Raman spectra of as-synthesized and zinc-treated CIS nanocrystals. (c) SAXS diffractograms for materials synthesized at different temperatures.

These diffractograms also show that the effect of Zn at post-treatment varies with the NC size. The alloy Zn-CuInS$_2$ has a diffractogram that is upshifted from that of CuInS$_2$[137], given that the former has a smaller lattice parameter—Zn having a smaller ionic radius. In our Zn-treatment, we mentioned that blue-shifts in the absorption spectra (Figure B1c) and shifts to

29

higher Q values in XRD peak position (Figure 2.3a) occur more prominently with materials synthesized and Zn-treated at lower temperatures. This suggests that for smaller particles, alloying of Zn into the $CuInS_2$ core is more likely, whereas for larger particles, Zn exchanges at the surface aiding its colloidal stability.
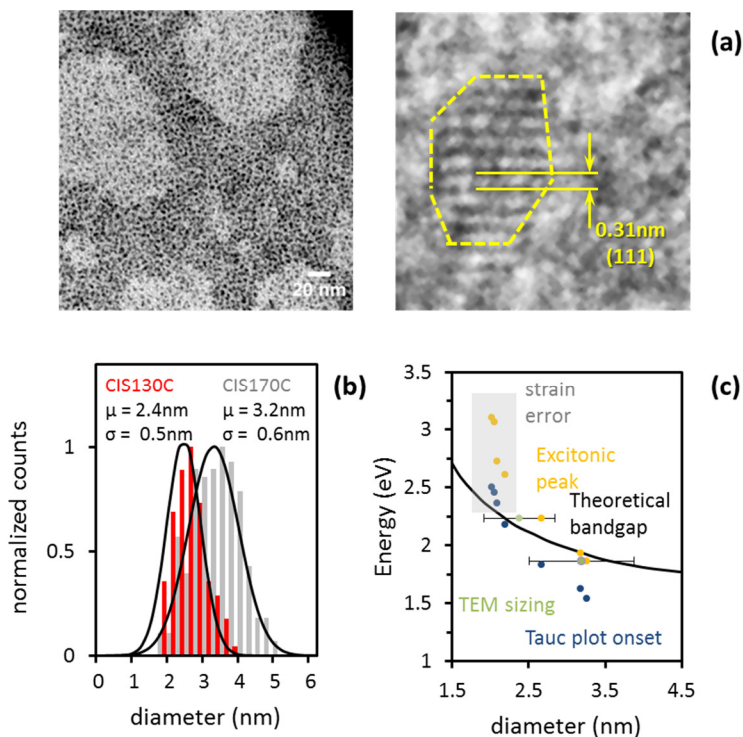
Figure 2.5 Nanocrystal size and bandgap. (a) TEM micrograph of CIS-ZnOA nanocrystals synthesized at 170°C, (111) planes shown. (b) Size distribution of CIS130°C and CIS170°C obtained using ImageJ software. The particles have around 20% deviation from the mean. (c) The difference between theoretical bandgap and experimental bandgap with varying size; excitonic peak and Tauc plot onsets have been plotted with XRD sizing while TEM sizing has been plotted with respect to excitonic peak positions.

The Raman spectra (Figure 2.3b) show main overlapped peaks at 305 cm^{-1} and 347 cm^{-1} modes. Unlike the synthesis without TOP (Figure 2.2a), these particles do not show any $Cu_{2-x}S$ peaks at around 470 cm^{-1}. These main overlapped peaks signify a disordered CIS with a copper deficient *CuAu* structure which is upshifted from the usual 290 cm^{-1} for chalcopyrites[146]. It is

30

however difficult to distinguish the presence of ZnS, resulting from the Zn-post-treatment as its peaks overlap with that of CIS. However, no distinguishable change is observed between CIS-OlAmTOP and CIS-ZnOA Raman spectra.

This calculated diameter of 3.3 nm agrees well with the average value of 3.2 nm from transmission electron microscopy (TEM) sizing (Figure 2.5a, b), showing clear (111) planes. The relationship of NC diameters and bandgap for selected ternary sulfides has been theoretically calculated using an effective mass approximation (EMA) with finite-depth wells by Omata et al[147] and Zhong et al[111], demonstrating good agreement with their experimental data from synthesized CIS NCs, taking the Tauc plot onset as the bandgap with exciton binding energies in the range of 32-95 meV[111]. Figure 2.5c shows the dependence of CISZn-OA diameters with the Tauc plot onset and how it deviates from the theoretical calculation. In fact, while the exciton Bohr diameter of CIS has been calculated to be 8 nm[114,148], we see that the bandgap of the materials presented in this work to be at their bulk value even at 3.3 nm.

We acknowledge that XRD sizing by the Schrerrer equation can however lead to an underestimation of sizes due to material strain and is more prone to error for much smaller sizes (as in Figure 2.5c). For sizes above 2.4 nm though, even as it seems that there would be a better fit to the EMA prediction using the excitonic peak as the definition for the bandgap, this EMA prediction is based on stoichiometric CIS while these particles are Cu-poor and Zn-alloyed and a much higher bandgap is expected: these particles possess much narrower bandgaps for their corresponding size. This discrepancy suggests large exciton binding energies, given that the exciton binding energy is the difference between the electronic bandgap with the optical bandgap[111].

2.5 Oxidation states of constituent elements and NC composition

Figure 2.6 shows the high resolution X-ray photoelectron spectra for Cu, In, Zn and S. Here, the metals and sulfur are in their correct oxidation states and agree well with the reported binding energies of CIS (NIST standard). The weak satellite peaks of Cu suggest that there is no Cu^{2+} species in the system, that Cu is in its Cu^{1+} state. Further, a better fit for the high resolution XPS spectrum of In and Zn is obtained if two species are introduced. These smaller

contribution- and downshifted species are likely to be M-O or M-carboxylate species, suggesting that the surfaces are In- and Zn-rich.
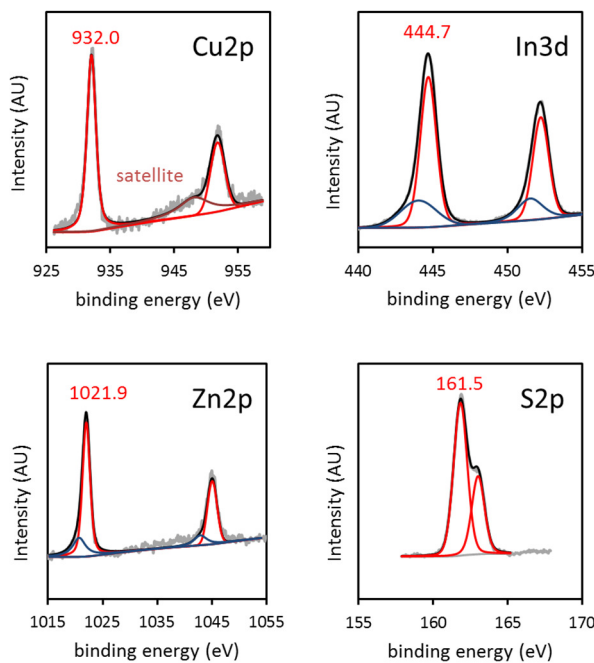
Figure 2.6 XPS spectra of CIS-ZnOA nanocrystals. X-ray photoelectron spectra of Zn-treated CIS nanocrystals demonstrating the constituent elements are in their correct oxidation states. Zn and In has two species present in the material, which can be interior and surface atoms.

As has been mentioned, these particles deviate from the usual stoichiometry of $CuInS_2$ (Table 2.1) as seen from energy-dispersive X-ray spectroscopy (EDX) and X-ray photoelectron spectroscopy (XPS) data. The EDX values are within 10% error. This off-stoichiometry is affirmed in the XPS data and the much higher Zn and In compared to the lower Cu values than EDX suggests the assertion that surfaces are zinc/indium rich. Further, it has been reported that the bandgap, emission peaks and PLQY of ternary nanocrystals can be tuned by changing the NC stoichiometry[149]. A question arises therefore as to whether the changes we see in absorption is also related to changes in stoichiometry, having indeed seen that the particles change in size with respect to injection temperatures in the previous section.

Table 2.1 Compositions of CIS for various synthesis temperatures and Zn treatments, using EDX and XPS. Values normalized to reach a sum of 4.

	90°C		130°C		170°C		XPS
	crude	Zn	crude	Zn	crude	Zn	Zn
Cu	0.23	0.20	0.30	0.33	0.50±1%	0.48±8%	0.35
Zn	-	0.94	-	0.56	-	0.43±12%	0.57
In	1.92	0.75	2.07	0.90	1.36±7%	0.98±6%	0.97
S	1.85	2.11	1.63	2.20	2.14±4%	2.12±2%	2.10

We observe that these particles maintain a near constant Cu/In replacement ratio, at 50% of Cu, throughout different synthesis temperatures and that it is their size that affects optical properties. With a model wherein a copper-deficient core is decorated by surface indium ions (calculation in the Appendix, Table B2), we see little variation in the calculated stoichiometry change through copper replacement by indium in the range of 90-170°C injection temperatures. Keeping the Cu/In replacement ratio constant, the decreasing Cu/In ratio with decreasing size seen in the EDX data is brought about by the influence of greater surface to volume ratio. The converse is verified as is also seen for copper rich particles[111]: instead an increase Cu/In ratio with decreasing size. This model is a logical assertion: (1) as $2V_{Cu}' + In_{Cu}^{\bullet\bullet}$ is a common defect formation in chalcopyrite materials, (2) as there is little change in the copper content after zinc-treatment and (3) as zinc replaces more indium for smaller particles, from 16% of indium for CIS synthesized at 170°C to 35% for that at 90°C.

From here, we can now therefore build a description of the material starting from its synthesis, as shown in Scheme 1 wherein a copper-deficient core, decorated with indium atoms is treated with zinc oleate. The scheme shows representation of the particle as viewed from the (100) plane.

This synthesis can also be used to make alloys of $CuInSe_2$ and $CuInS_2$ by using bis(trimethylsilyl) selenide in place of the sulfide and compositions

thereof (Table B3), although further characterization is needed to ascertain whether the products are homogenous and not mixtures of selenides and sulfides.

Scheme 2.1 Synthetic scheme and NC structure. Indium decorated copper-poor cores stabilized with TOP and OlAm are treated with zinc oleate.
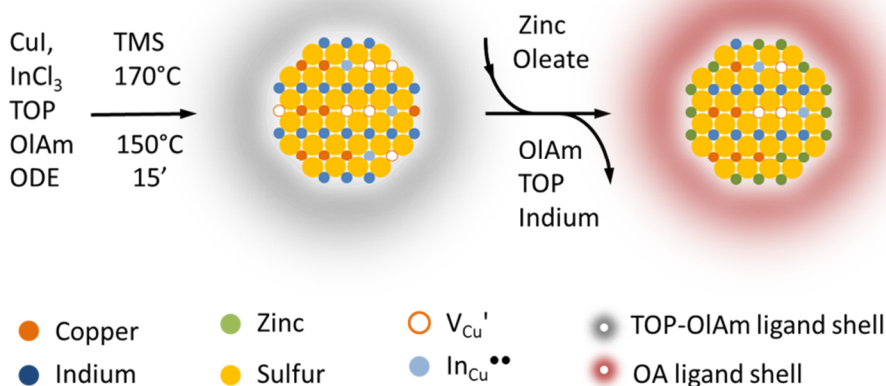
2.6 Ligand exchange strategy and phase transfer

Prior to Zn-treatment, these particles are coordinated with OlAm (Figure 2.7a), showing a characteristic N-H peak at 3360 cm^{-1}. TOP does not have any unique peak that could be assigned in the spectra apart from weak signals at 2663 cm^{-1}. However, we do see the presence of phosphorus in the EDX spectra of CIS-OlAmTOP (Figure B5). After zinc oleate treatment, N-H peaks in the FTIR spectra and phosphorus peaks from EDX vanish, whereas the symmetric and assymmetric C-O vibration modes appear, suggesting their replacement with a deprotonated OA. This OA binds in an ionic binding mode, inferred by comparing ν_{sym}- ν_{as} to its salt.

As before, by spin-coating the material on double-sided polished silicon and exposing the film to various ligands, we monitored the extent of ligand removal through the disappearance of the C-H vibration modes at 2700-3100 cm^{-1}. This goes in line with the reduction of the peak at $\nu > 3000$cm^{-1} with treatments, which is characteristic of C=C-H vibrations present in oleic acid. These

nanocrystals have mostly zinc and indium at the surface, whose ions are classified as hard acids according to the HSAB theory[49]. Hard ligands remove most of the native OA on the surface, with a 94% peak height reduction after a three-minute immersion in formic acid in room temperature (Figure 2.7b). In contrast, EDT being a soft base thiolate source results in a much weaker ligand replacement, retaining some residue of the C=C-H modes, while with ethylenediamine, being a harder ligand leads to an almost complete removal of native ligands, (Figure B7). This is in contrast with PbX (X = S, Se) nanocrystals, wherein soft ligands, such as thiols or iodides, preferentially bind on the surface[49].
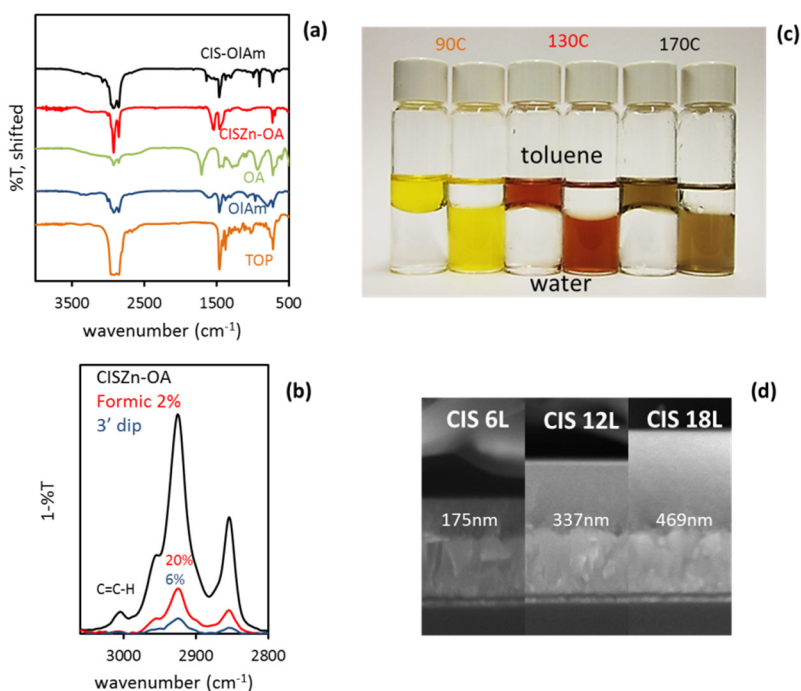
Figure 2.7 Ligand exchange and phase transfer of CIS NCs. (a) FTIR spectra of as-synthesized and Zn-treated nanocrystals along with ligands used during the synthesis. (b) The removal of oleic acid from the nanocrystal surface as seen through the reduction of the C-H and C=C-H peaks. (c) Image of phase transfer of various NCs into a polar solvent, using MPA and a base. (d) Cross-sectional SEM images of films from CIS170 using formic acid showing control on thicknesses.

With this understanding, it is possible to transfer these nanocrystals into a polar phase using a bifunctional molecule such as mercaptopropionic acid (MPA) for different NC sizes (Figure 2.7c). We wanted to monitor which functional group attaches to the NC surface, whether it is the thiol or the carboxylic acid. We used bifunctional ligands with the same functionalities a dithiol, a dicarboxylic acid and one with different functionalities, a thiol-carboxylic acid and observed the precipitation upon their addition (Figure B7). The dithiol does not lead to any precipitation while the diacid and the bifunctional ligand with a carboxylic acid led to particles settling at the interface. This confirms what we have concluded from the FTIR data, that the acid group binds to the surface of the nanocrystals. This leads us to conclude that during phase transfer the deprotonated thiol group is exposed to water. These polar solutions maintain their luminescent properties (Figure B7) and may cater to bio-labelling applications as a non-restricted alternative material, containing no toxic elements.

Using hard ligands such as formic acid, we can also build films with controllable thicknesses (Figure 2.7d). With a concentration of 25 mg/mL, NCs in toluene were deposited via the LbL process, resulting around 25 nm thick layers per cycle. This opens the way to utilizing these materials as colloidal quantum dot solids in optoelectronic devices.

In summary, we attempted to perform a ligand exchange process on thiol-synthesized CIS and found it difficult to remove long DDT ligands. These long organic molecules act as barriers for transport and are undesirable for electronic applications. We therefore designed a synthesis opting to omit DDT from the reaction, using different molecules to substitute for the functions it performed. This synthesis led to particles with tunable sizes and optical properties. We found that the products are Cu poor and decorated with Zn and In at the surface. This brought us to rationally choose the ligands to employ for ligand exchange, allowing us to perform the transfer of the NCs to a polar phase and to control the film thicknesses of CQD solids. The advances in performance in PbS started from the synthesis of high quality nanocrystals[64] which was deposited as functional optoelectronic films[51–53,59,65–67]. These results provide an important stepping stone in the realization of solid-state CIS CQD devices.

36

CHAPTER 3
CuInS$_2$ Colloidal Quantum Dot Solids: Properties and Optoelectronic Devices[e]

We have identified in Chapter 1 that for solar cell thin film materials, the following materials properties are important considerations for good device performance: carrier mobility, conductivity type and doping, band edge levels, absorption coefficient, trap density and carrier lifetime. On top of this, for colloidal quantum dot solar (CQD) cells, materials processability is a requirement for device fabrication. We have covered, in the previous chapter, the synthesis of thiol-free CuInS$_2$ (CIS) nanocrystals that can be processed into films with controllable thicknesses. This development allows us to incorporate CIS NCs in CQD optoelectronics. In this chapter, we will characterize the CIS CQD film, covering most of the thin film properties mentioned above, this allows us to design optoelectronic devices by choosing appropriate materials and device parameters. This chapter ends with a demonstration of, for the first time, an unannealed CIS CQD solar cell that is processed and measured at ambient conditions.

---

[e] This chapter has been reproduced in part from Ref. [170] with permission from the American Chemical Society, copyright 2015 and in part from Ref. [186] with permission from the Royal Society of Chemistry, copyright 2016.

3.1 NC-NC coupling: photoluminescence decay with ligand length.

The distance between nanocrystal to nanocrystal in an assembly controls the transport of charges in the CQD solid.[66,150] For example, conductivity was improved in PbSe CQD solids by shortening diacid chains[68] and that the short circuit current density (J_{sc}) in completed CuInSe$_2$ devices was increased when native ligands are exchanged for shorter inorganic ligands[151]. We begin this chapter by looking into the NC-NC coupling in CIS CQD films.
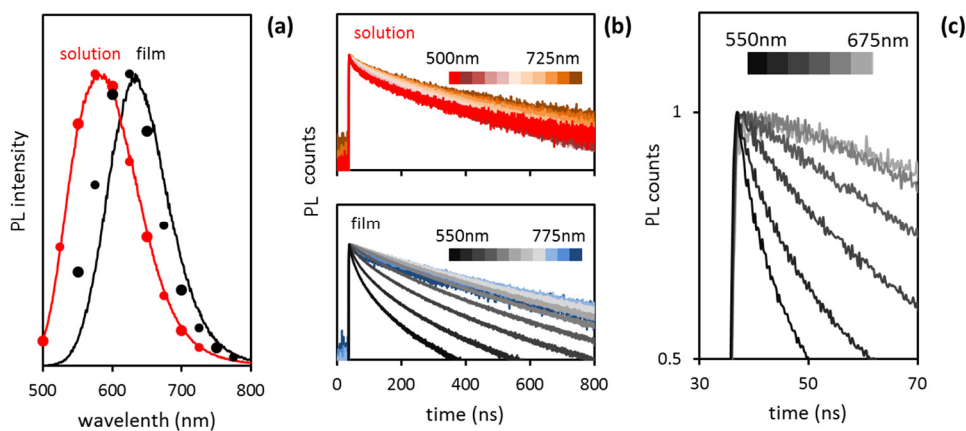
Figure 3.1 Photoluminescence of CIS NCs in solution and in the solid-state. (a) Steady-state PL of in-solution and dropcasted CIS110°C NCs. A significant redshift between for CIS nanocrystals synthesized at 110°C in solution and as a dropcast film. (b) Time-resolved photoluminescence probed at various points (short to long wavelength) in the emission spectra, this can be used to reconstruct (a). (c) TRPL of CIS NCs in solid-state at short time scales showing a characteristic rise time.

The effect of nanocrystal-to-nanocrystal distance on the PL properties was probed by looking at the steady-state and time resolved photoluminescence spectra of CIS, synthesized at 110°C, in (1) a dilute solution and in (2) a dried drop-casted film. There is a photoluminescence redshift of 50 nm from solution to the solid state (Figure 3.1a). PL redshifts have been noted in PbS films as an indication of good electronic coupling between NCs due to an overlap of wave functions between adjacent nanocrystals[68]. If we observe the time-resolved photoluminescence (TRPL) spectra of these samples, we see that the TRPL spectra of CIS in solution are invariant when probed at different

wavelengths in the emission spectrum; whereas for CIS as a film, photoluminescence decays are faster when probed at shorter wavelengths (Figure 3.1b). If we integrate these TRPL decay curves, we can reconstruct from Figure 3.1b, the steady-state PL in Figure 3.1a to good measure.

This change in PL lifetimes with respect to probe wavelength points to a possible energy transfer from smaller- to larger-sized crystals within a size distribution of a single sample[152]. Energy transfer, such as the Förster resonant energy transfer is a non-radiative energy transfer process through dipole-dipole coupling and is sensitive to distance between two participating species. Nanocrystals, as has been shown in the previous chapter, possess a certain size distribution with smaller and larger particles falling on either tail of a distribution. In solution, particles are much farther apart for significant energy transfer to occur, whereas in solid state films, this transfer is possible. Further proof of energy transfer can be seen by looking at short time scales[152] near the start of the PL decay (Figure 3.1c). If energy is being transferred into another species, the PL of this particular species will increase for a time and then decay when no further energy is being transferred. We saw a characteristic rise time in the PL decay in the form of a plateau (Figure 3.1c) when the emission was probed at longer wavelengths of the emission, supporting resonant energy transfer from within size distributions within the NC solid assembly.
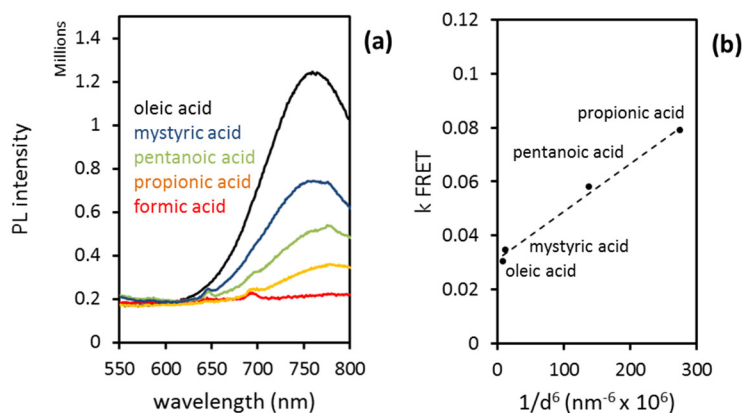
Figure 3.2 The effect of interparticle spacing on the photoluminescence of CIS assemblies. (a) The steady-state photoluminescence of films decreases with ligand length and (b) follows the Förster relationship.

To further elaborate this, we looked at the photoluminescence of films treated with carboxylic acids of various ligand lengths, keeping the same solution concentration for spin coating. Figure 3.2a shows the steady-state photoluminescence of CIS films exchanged with tetradecanoic, pentanoic, propionic and formic acid. A redshift in emission appears and photoluminescence decreases with the decrease in molecule length, and consequently NC to NC distance. Photoluminescence lifetimes decrease with ligand length, as also observed in PbS assemblies[153]. We found that the transfer rates ($k_{FRET} = 1/\tau_{film} - 1/\tau_{solution}$) of these CIS films decrease with ligand length following a linear trend with sixth power of distance (Figure 4d), agreeing with the Förster relationship:

$$k_{FRET} = k_{isolated} \ \left(\frac{R_0}{d}\right)^6$$

where $k_{isolated} = 1/\tau_{solution}$, d is the center to center distance between two species and R_0 is the Förster radius, where the energy transfer efficiency is defined to be 50%. For the same NC-NC distance, more efficient energy coupling is therefore attainable for larger Förster radii. A Förster radius of 5.8nm was calculated which is comparable to that reported for PbS, 5nm[154] and CdSe, 8nm[155].

Choi et. al. has proposed a model for transport in two NC-NC distance regimes in PbS assemblies—that for large distances, such as observed by Lingley et al, nonradiative resonant energy transfer dominates with low transfer rates and that for short distances, coherent tunneling dominates through the overlap of wavefunctions leading to higher transfer rates[152,153]. Apart from a reduction in NC spacing, coherent tunneling in NC assemblies is favored when a high coupling energy is matched with a low exciton binding energy arising from high dielectric constants. We do not see any transition between these two regimes in the range of distances studied, whereas Choi already noted a deviation from the Förster relationship at the shortest distance we have used. It is possible that this transition occurs at distances shorter than twice that of propionic acid, such as using formic acid. However, photoluminescence for films exchanged with formic acid is quite low to perform any TRPL measurements. The transition to a coherent charge transfer mechanism by

tunneling is perhaps limited by high exciton binding energies which deter the dissociation of carriers. Evidence of high exciton binding energies has been seen in the discrepancy in optical and theoretical bandgap (Figure 2.5c). Choi et al, for example asserted that coherent tunneling in CdSe films is hindered, in part due to its high exciton binding energy, at 300meV[156] for 3.3 nm particles while for PbS of the same size, with exciton binding energies of 100meV[154], for the same coupling energy, coherent tunneling is possible.

3.2 Transistor behavior, conductivity type and mobility of CIS CQD films

Despite this, we find that these films, after having been treated with formic acid, conduct albeit having low carrier mobilities and moderate carrier concentrations. With these films, we were able to fabricate bottom-gated staggered top-contacted thin film field effect transistors (FETs) (Figure 3.3a) to extract a measure of the carrier mobility. FETs are electronic switches that are controlled by the application of a field through a dielectric. In Figure 3.3a, the current flowing between the two gold contacts is modulated by the potential applied at the gate through the SiO_2 dielectric. If the semiconductor material is *p*-type, negative gate voltages turn the transistor on by the accumulation of holes at the dielectric-material interface; the converse happens for *n*-type materials. From the drain-source current (I_{DS}) vs gate voltage (V_G) curves, also called the transfer curves, it is possible to determine the carrier type and the majority carrier mobility. The carrier type can be determined by looking at which gate voltage the transistor turns on while the carrier mobility μ is proportional to the transconductance G_m by

$$\mu = \frac{G_m \, L}{W \, C \, V_{DS}}$$

where G_m is taken as slope in the linear region in the transfer curve, L is the channel length, W the channel width, C the gate capacitance per unit area and V_{DS}, the applied drain-source voltage. Carrier concentrations can be obtained by measuring the conductivities of films.

Figure 3.3b shows the transfer characteristics of CIS, synthesized at 170°C, 130°C and 90°C, NC-FETs with formic acid as the ligand. Modulation occurs at

negative gate voltages and indicates that the film has *p*-type conductivity which is expected for CIS semiconducting films. We obtained a hole carrier mobility of 1.9 x 10^{-5} cm^2 V^{-1}s^{-1} for CIS synthesized at 170°C. This mobility is two orders of magnitude lower than that for EDT-treated PbS films[66] and three orders lower than that made from chalcopyrite films containing Se[157]. These films show moderate carrier concentrations of 5.7 x 10^{16} cm^{-3} despite the large off-stoichiometry of the films. FET characteristics of devices from smaller nanocrystals demonstrate lower mobilities. Earlier reports have shown that mobility decreases with nanocrystal size for the same nanocrystal to nanocrystal distance, which has been ascribed to increased hopping phenomena[66]. However, Yazdani, et al[150] demonstrated that for small enough inter-nanoparticle spacing, significant overlap of wavefunctions will, on the contrary, lead to higher mobilities for assemblies from smaller particles. The decrease in mobility from smaller-sized particles, which is commonly observed, then is ascribed from increased trap density with size.
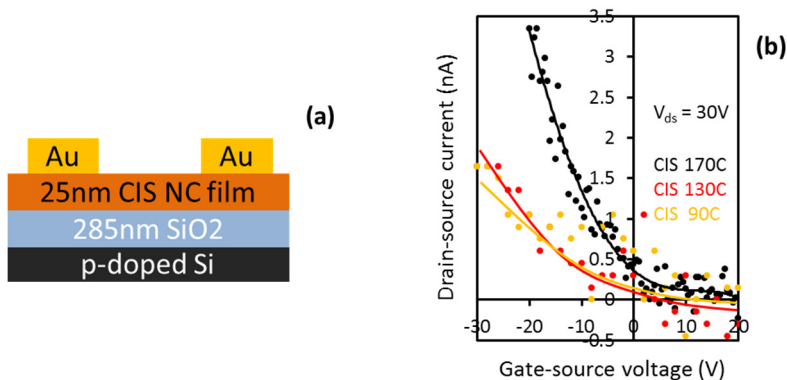
Figure 3.3 Transport properties of CIS NC films. (a) Device structure for bottom-gated top-contacted field effect transistors with 30µm channel length and 1mm channel width. (b) Transfer characteristics of CIS NC FET showing differences in the transconductance with size.

3.3 Photodetectors from CIS CQD solids

We further evaluated the optoelectronic properties of the films CIS synthesized at 170°C, by constructing photodetectors whose structure is shown in (Figure 3.4a). These photodetectors operate by having increased conductivity under the presence of light (photoconductance). We subjected the devices to 200s 635nm laser light pulses at varying light intensities (15-520µW/cm^2). The

42

measured photocurrent I is linear with light intensity P and follows the power law $I \propto P^b$ with a sublinear trend $b = 0.7$ (Figure 3.4b). For $0.5 < b < 1$, the electron-hole generation in the semiconductor is dominated by trapping and recombination[158]. Further, the responsivity R = I / P, tends to plateau at higher intensity. Without photoconductive gain, photodetectors at 100% quantum efficiency can only achieve a responsivity of 0.51 A/W.[f] Long-lived traps of one carrier provide gain for a photodetector by allowing the other carrier to cycle more than once before recombining. Thus at higher light intensities, the available number of trap states contributing to photoconductive gain is lowered due to trap filling[159], and thus responsivity saturates. We see in Figure 3.4b that the responsivity decreases with higher intensities and levels off at 250 μW/cm^2.
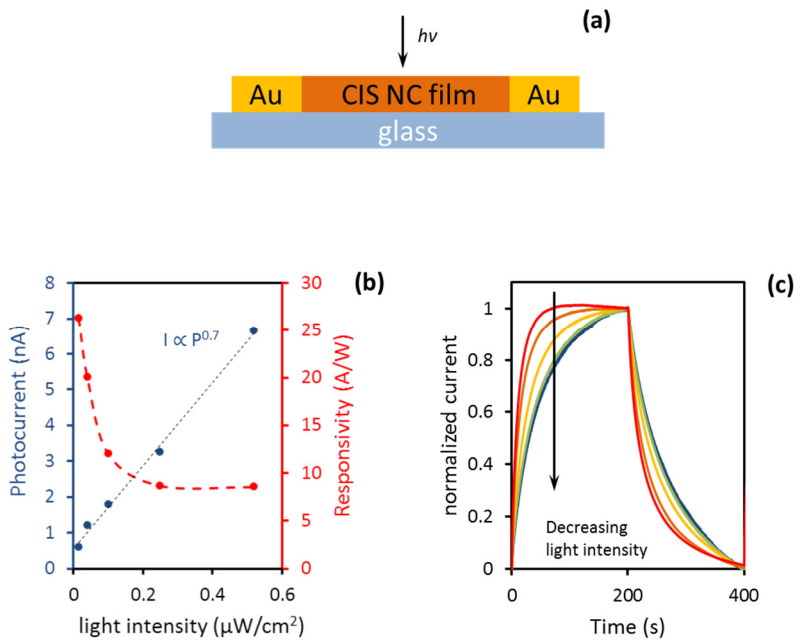
Figure 3.4 Photoconductive properties of CIS NC films. (a) Device structure for CIS (170°C) photodetectors, 3mm length and 50 μm width. (b) The material shows sublinear increase in photocurrent and a saturation of responsivity with light intensity. (c) Longer rise and decay times are observed for decreasing light intensity. Samples were illuminated with 200s 635nm laser light pulses (15-520μW/cm²).

---

[f] $R = \eta \frac{q}{hf} G$ where η is the quantum efficiency, q is the electron charge, h is Planck's constant, f the frequency of incident light and G is the photoconductive gain. For incident 635 nm light and no photoconductive gain ($G = 1$) the maximum possible R is 0.51.

We normalized the photocurrent to show the asymmetry in rise and decay response and the differences in rise and decay times at different intensities (Figure 3.4c). For materials which do not have traps, the rise and decay times should be invariant with light intensity. The presence of traps increases the rise and decay times, observed as when light intensity is decreased because trapped carrier density outweighs free carrier density when traps remain unfilled[160]. The sublinearity of photocurrent with light intensity, high responsivies which saturate at high intensities and long response times that increase with decreasing light intensity describe an NC solid film having a high trap density.

3.4 Band edge positions, Type II heterojunctions with TiO$_2$

To fabricate CQD solar cells, it is necessary to identify the band edge positions of semiconductor absorber films so as to appropriately choose a suitable complementary material with which to form a junction. We find that CIS NCs have band edges which match well with that of TiO$_2$, allowing for the formation of a Type II heterojunction (Figure 3.5a). Through ultraviolet photoelectron spectroscopy, these band edges can be obtained by locating the Fermi level from the cut-off energy of biased samples, and the valence band edge by adding the value of the onset of unbiased samples to the Fermi level (Figure C1). The band edges and Fermi level position of the smallest bandgap material (CIS 170°C) vary with other reports[111,161] but agree with that reported by Borchert[119]. We also see that for CIS of different sizes, the Fermi level remains fixed. This has been seen in other materials as an indication of high trap or defect density[162]. With changes in size, the valence band edge also remains roughly constant, with shifts being more apparent in conduction band edge positions. This has similarity with that of PbX and CdX (X=S, Se or Te)[163].

We deposited thin layers of CIS (CIS 130°C) onto TiO$_2$ and controlled the spacing between these materials by adsorbing bifunctional ligands of various lengths onto TiO$_2$. Because of the favorable band edge positions of TiO$_2$ and CIS, we see that the photoluminescence lifetime (excited at 636 nm, probed at 770 nm) systematically decreases with decreasing CIS-TiO$_2$ distance (Figure 3.5b). This decrease in PL lifetime with distance to an acceptor has also been observed for thinner ZnS shells[164], accounting for much efficient electron transfer to TiO$_2$ with shorter distances.

44
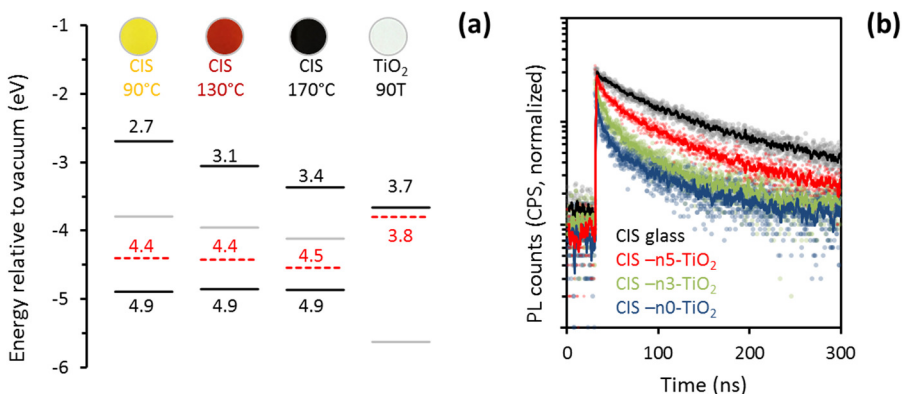
Figure 3.5 Band-edge positions and charge transfer processes to TiO₂. (a) Conduction band edges obtained from UPS, showing a type II heterojunction with TiO$_2$ and a near constant Fermi level for different NC sizes. (b) Transient photoluminescence of dilute CIS-130°C solution deposited on TiO$_2$ with various adsorbed diacids: n0, oxalic acid; n3, glutaric acid; n5, pimelic acid.

3.5 Colloidal quantum dot solar cells from CuInS₂ QDs

Knowing that CIS can transfer electrons to TiO$_2$, we can therefore fabricate solar cells with this heterostructure. Annealed CIS nanocrystals in contact with various materials have led to solar cells with various open circuit voltages (V$_{oc}$): CdS, 0.48-0.71 V[122–124]; ZnO, 0.40-0.46 V[117,118]; P3HT or PSiF-DBT, ~0.25-0.54 V[165,166]; with bulk CIS on TiO$_2$[167–169] giving a V$_{oc}$ of 0.49-0.57 V. When layers of CIS NCs are deposited via the ambient LbL process onto TiO$_2$, a heterojunction forms with a similar built-in potential of almost 0.6 V. Considering the UPS data, Au is a suitable hole extracting contact and was deposited via thermal evaporation. The structure of this solar cell is shown in Figure 3.6a.

When materials of opposing carrier types are placed in contact, carriers diffuse away and recombine, leaving a region that is depleted of carriers at the junction. This depleted region can be treated as a capacitor and characterized using Mott-Schottky analysis. Given that CIS has a lower carrier concentration that that of TiO$_2$, the depletion region will lie mostly on CIS and this analysis can be carried out to characterize the CIS layer. Completed devices show a near constant capacitance for low applied voltages (Figure 3.6b) indicating that they

45

are nearly depleted, which through Mott-Schottky analysis (see Appendix C) yields depletion widths of 125 nm, close to the absorber thickness (170 nm). In agreement with the previously reported carrier concentration for this material[170] as well as in using FET mobility and conductivity data as in section 3.2, we calculated a comparable carrier concentration of 2×10^{16} cm^{-3}.

The device performance is shown in Table 1[g]. For the material synthesized at 170°C, the performance is near identical to that reported for a CIS NC-ZnO bilayer heterojunction[117], showing low fill factors (FF) and short-circuit photocurrent densities (J_{sc}). For solar cells made from smaller particles, the series resistance increases most likely due to their lower mobility[170]. The spectral response of the external quantum efficiency (EQE) of the solar cells follows the absorption of the CIS QDs, showing the tunability of the photocurrent onset with size (Figure 3.6c). The V_{oc}, however, in line with the determined constant Fermi level positions, does not increase with size.
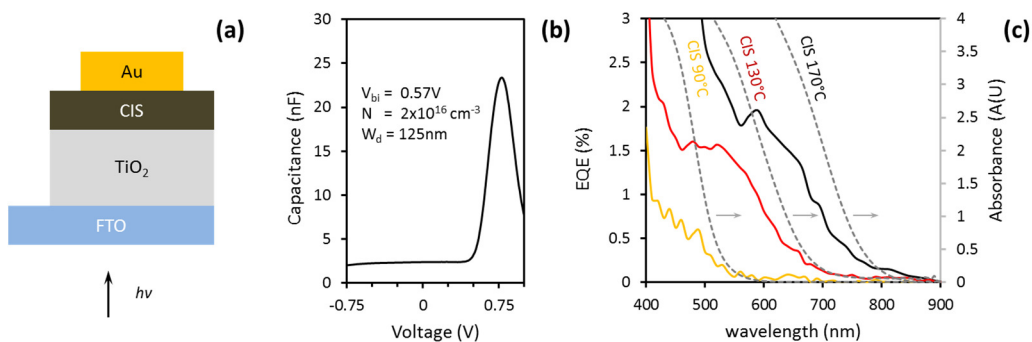
Figure 3.6 Solar cells from layers of CIS CQD solids and TiO₂. (a) The device structure of a CIS CQD solar cell. (b) The capacitance-voltage profile of a CIS-TiO₂ bilayer device showing a flat profile at low applied voltages. (d) EQE spectra of CIS-TiO₂ bilayer devices which correspond well with the absorption spectra (in grey) of the respective nanocrystals.

g Error values are shown in Appendix C.

Table 3.1 Device performance of CIS of various sizes, thicknesses and Zn content on flat-TiO_2

CIS	Zn	layers	V_{oc}	J_{sc}	FF	PCE
90°C	1.0	6	0.50	0.011	0.29	0.002
130°C	1.0	6	0.55	0.077	0.25	0.011
170°C	1.0	**6**	0.59	0.91	0.27	0.15
170°C	1.0	**12**	0.60	0.93	0.32	0.19
170°C	1.0	**18**	0.61	1.08	0.33	0.22
170°C	0.3	**6**	0.63	1.26	0.31	0.23
170°C	0.3	**12**	0.62	1.39	0.30	0.29
170°C	**0.3**	**18**	0.60	1.67	0.33	0.33
170°C	**0.1**	6	0.63	1.81	0.26	0.30

3.6 The effect of Zn reduction: mobility and optical properties

We aimed at improving charge transport in the CIS film by reducing Zn during post-treatment overcoating. For these nanocrystals, during post-treatment with Zn-oleate, we have proposed[170] that zinc incorporates itself through the surface, by adsorption and by replacement of indium which is rich on the surface. This zinc-rich shell could hinder transport in the NC film; recall that when the thickness of a ZnS shell is reduced, this had led to more efficient electron transfer.[164] We reduced the amount of zinc from its usual amount (1.0 Zn), to a third (0.3 Zn) and to a tenth of this content (0.1 Zn), maintaining all other amounts the same. In Table 3.2, we see a reduction in zinc and an increase in mobility corresponding with these modifications.

As well, in support of the model of the NC structure discussed in Chapter 2—that a copper-poor core is decorated by indium atoms, indium increases with decreasing zinc while copper and sulfur remain comparatively the same. This implies that zinc replaces indium mostly in the structure. The lower amount of zinc leads to a more red-shifted emission closer to that of untreated CIS nanocrystals (Figure 3.7a) and a lower PL quantum yield (Figure 3.7b). These changes go in line with the NC model we presented in Chapter 2.

Table 3.2 The reduction in zinc post-synthetically, shows marked reductions in Zn content as seen through EDX and a corresponding increase in indium and higher mobilities.

	1.0 Zn	0.3 Zn	0.1 Zn
Cu	0.47	0.45	0.44
Zn	0.44	0.35	0.30
In	0.97	1.03	1.08
S	2.12	2.18	2.18
μ (cm^{2}V^{-1}s^{-1})	1.9×10^{-5}	3.0×10^{-5}	5.2×10^{-4}
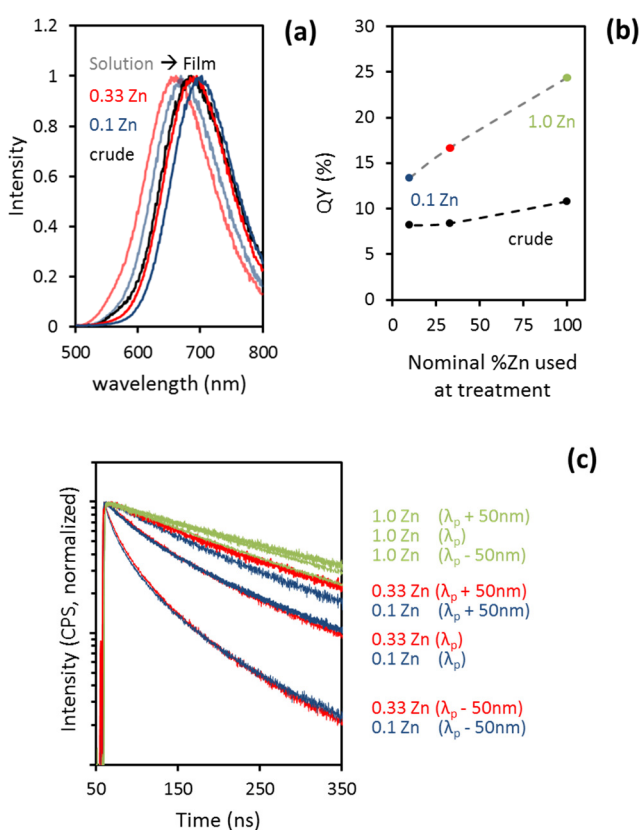
Figure 3.7 Effect of reduced Zn on the optical properties of CIS NCs. (a, b) PL of Zn-CIS with various Zn content. The reduction of Zn during post-synthetic treatment leads to (a) a more redshifted emission and (b) a lower photoluminescence quantum yield. (c) Time resolved PL of drop-casted films with different Zn content. Particles with reduced Zn have better interparticle coupling: faster PL decay probed at wavelengths lower than the PL peak.

For assembled solids with native ligands, using the similar experimental treatment as in section 3.1, we see that for the same shift from the photoluminescence peak λ_p, at λ_p + 50 nm, the PL decay is faster for nanocrystals with lower Zn content. This demonstrates improved coupling between nanocrystals in the ensemble. Correspondingly, for ligand-exchanged films this results in improved mobility (Table 3.2).

This increase in mobility with decreasing Zn content coincides with increase in J_{SC} (Table 3.1). In fact, the total J_{SC} can be increased to almost twice its value by lowering the zinc content at post-treatment (1.0 Zn) to a tenth of its value (0.1 Zn); unfortunately, going lower than this Zn value lessens the colloidal stability[170] of the material. While reducing Zn enhances J_{SC}, the FFs remain low at less than 50%. Despite the relatively high V_{OC}, we will see that devices have J_{SC}s far from their maximum expected values.

3.7 Predicted J_{sc} for various thickness, fitted IQEs

It might seem logical to increase the absorption of a CQD film, by increasing its thickness, in order to increase the J_{SC}. The absorption coefficient (Figure 3.8a) of CIS ligand-exchanged with formic acid in the solid state was obtained by measuring the transmission and reflection of three films of known thicknesses. This CIS CQD film has absorption coefficients which are comparable to previous reports[117] based on that of NCs yet much lower than that of bulk CIS[171], most possibly due to the CQD films, being composed of packed spheres, containing gaps. By assuming an internal quantum efficiency of unity and no optical losses, a predicted J_{SC} was calculated by taking the double-pass total absorbed AM 1.5G light[h] as the total current, leading to a maximum J_{SC} of 27.8 mA/cm^2 (Figure 3.8b) for a film of infinite thickness. A predicted J_{SC} of 14.9 mA/cm^2, for example is obtained for a film of 500 nm.

Clearly, the results from Table 1 indicate that the values we obtained are far from the predicted values. For example, a device of 6 layers of CIS deposited via LbL yields a J_{SC} of almost 1 mA/cm^2, whereas it should provide more than 5 mA/cm^2. It can also be noted that the J_{SC} does not scale in multiples

---

[h] Simulated sunlight wherein the sun is at 48° from the zenith, filtered by the atmosphere resulting in an intensity of 1000 W/m^2

accordingly to layer thicknesses, that at 12 and 18 layers, the J_{SC} is not even barely twice that of 6 layers. This might lead to a conclusion that the J_{SC} is independent of absorber thickness. However, when incoming light is filtered (400 nm) to exclude UV light, we see the J_{SC} increases with increasing thickness (Figure 3.8b). This points to the contribution of TiO_2 to the photocurrent and that for thinner films, more of the back reflected light reaches the front TiO_2 which balances the total J_{SC} resulting in final J_{SC}s which apparently does not vary much with thickness.
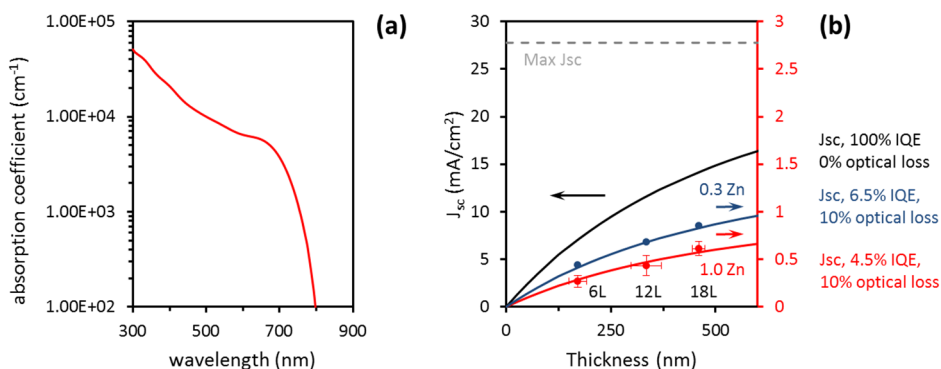
Figure 3.8 Absorption coefficient and the predicted J_{sc} with thickness. (a) Extinction coefficient of formic acid treated CIS 170°C films. (b) Thickness-dependent predicted J_{sc} (black) using obtained from extinction coefficient values. The J_{sc} (400nm bandpass-filtered) of solar cells of various NC absorber thicknesses (red), fitted with a predicted J_{sc} for devices with 4.5% IQE and 10% optical loss. The (400nm-filtered) Jsc of CIS 0.3 Zn devices with thickness (blue) fitted with 6.5% IQE and and 10% optical loss.

These data points can be fitted with an absorption-predicted J_{SC}, by assuming an internal quantum efficiency (IQE) of 4.5% and 10% optical loss for CIS treated with 1.0 Zn, while for CIS NCs treated with less Zn (0.3 Zn), the J_{sc} can be fitted assuming an IQE of 6.5% and 10% optical loss. We see that increasing the mobility increases the IQE only to a small extent, leaving issues on FF still unresolved. This low IQE signifies poor charge collection and transport in the absorber film. This most likely arises from traps which we have identified before in the previous sections, as PbS with a comparable mobility and at a particular adjusted absorption leads to a much higher J_{sc}.[172] This leads

us to look not only at mobility as the only deterrent for good device performance, but to address the problem of high trap density in the film as well.

In summary, we have shown that assemblies of CIS NCs couple to each other as seen in changes in PL lifetimes with distance. It is possible that due to high exciton binding energies, no coherent charge transfer occurs at particular distances. When particles are brought close together, these films conduct albeit having low mobilities and displaying features that signify high trap densities. The ability to form CIS NCs into solid-state CQDs has allowed us to fabricate optoelectronic devices such as transistors, photodetectors and solar cells. As absorbers in solar cells, CIS CQD solids have led to good V_{OC}s but low J_{SC}s and FFs. By taking the absorption coefficient of the CIS CQD solids, we found that the IQE of these devices, fitted from experimental J_{SC}s from devices of different thicknesses, are far below 10%. These highlight the importance of addressing the high trap density in the quantum dot solid.

Bulk Heterojunction Solid-State Colloidal CuInS$_2$ Quantum Dot Solar Cells[i]

In the previous chapter, we have covered the fabrication of a room-temperature-fabricated CIS CQD solar cell, with a PCE of 0.15% for that with the usual amount of Zn (1.0 Zn) and 0.30% for that with a reduced Zn (0.1 Zn). Mainly, we identified that the low performance comes from a low J_{SC} and FF. This low J_{SC} is far below the predicted values as purely taken from absorption leading to IQE predictions of around 4.5% to 6.5%. We attributed this to poor transport and collection of photogenerated charges in the CIS CQD film. Thus, it is important to develop an understanding as to the cause of this poor transport and design ways to alleviate it.

For materials with poor electrical properties, most works have turned to using a blended architecture to overcome hindrances to photovoltaic performance. A well-known example of this is in the field or organic solar cells[22]. In Chapter 1, we mentioned that organic solar cells are excitonic solar cells wherein photogenerated excitons need an interface to split them into free charges. Blends therefore are beneficial for organic solar cells as excitons are

---

[i] This chapter has been reproduced in part from Ref. [[186]] with permission from the Royal Society of Chemistry, copyright 2016.

much closer to an interface than their diffusion length[25]. For inorganic nanocrystalline solar cells, largely based on PbS, the formation of a blend or interpenetrated architecture provides many benefits.

For example, in a blend with Bi_2S_3 nanocrystals, it allowed for improved charge extraction as Bi_2S_3 is prone to electrical loss due to its high trap density[86]. It has also been shown that in a blend with ZnO nanocrystals the passivation of traps was achieved by compensating charges from ZnO[87] and it had led to overcome the short diffusion lengths of PbS NCs[84,173,174]. For CIS, in the bulk, improvements in the current and/or fill factor were achieved by incorporating it in porous TiO_2[167], in ZnO nanowires[175] and in a PbS NC solid[176]. It is also noteworthy to realize that in QD-sensitized solar cells, this blended architecture is implicitly attained and bypasses charge transport in the absorber. This most likely is an underlying reason why there is a gap between the performance of CIS NCs used as sensitizers and those used as an assembled unannealed solid.

In this final chapter, we discuss the fabrication of a blend of CIS NCs and TiO_2 by incorporating CIS NCs into a porous oxide structure, taking note of the changes in photovoltaic performance. We describe the recombination mechanisms in two device architectures, the bilayer and the bulk heterojunction (BHJ), by collating insight gleaned from transient photovoltage and photocurrent techniques, absorption, external quantum efficiency and photoluminescence data. This work ends with a proposal on the mechanisms that led to changes the performance with respect to device architecture.

4.1 Infiltration of CIS into a porous TiO_2 network

Solar cells discussed in the previous section were fabricated using 90T-TiO_2 sourced from DyeSol. This material comes as a paste comprised of TiO_2 nanocrystals of around 20nm, a structure-directing agent acting as a soft sacrificial template such as Pluronic F127 and a binder such as ethylcellulose. This paste is coated on substrates and then annealed to burn off the organics: Pluronic F127 and ethylcellose. This leaves a porous structure that is suitable for small molecule adsorption as in dye-sensitized solar cells.

In using this material, we investigated whether the nanocrystals infiltrate the 90T-TiO_2 network, given that dyes have much smaller sizes than nanocrystals. In Figure 4.1, we see that CIS builds up on the surface of the TiO_2 (Figure 4.1a)

54

in the same growth rate as that deposited on flat FTO substrates (Figure 4.1b). This shows that the 90T-TiO$_2$ network acts like a flat surface for the deposition of CIS NCs.
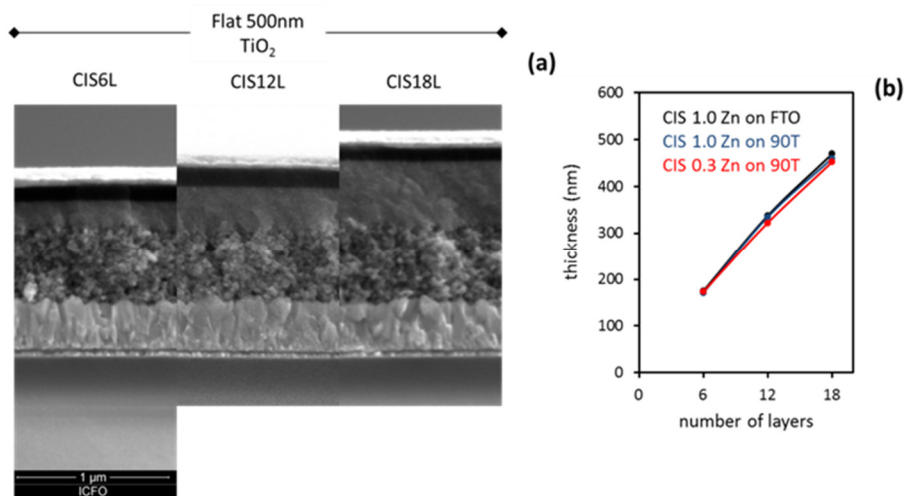
Figure 4.1 CIS and 90T-TiO$_2$ forming a bilayer structure. (a) SEM images of different number of layers of CIS deposited on 90T-TiO$_2$ showing that thickness increases with increasing layers and that no infiltration occurs for 90T-TiO$_2$. (b) Thickness with number of layers of various CIS treatments and substrates. These absorber thicknesses, of CIS 1.0 Zn as deposited on 90T (blue) and of CIS 0.3 Zn as deposited on 90T (red) have similar deposition growth as that of CIS 1.0 Zn as deposited on FTO (black).

We added excess ethylcellulose into the 90T solution, and found that it introduced large volumes of larger pore sizes as can be seen in the Barrett-Joyner-Halenda (BJH) transformation of the Brunauer-Emmett-Teller (BET) adsorption isotherm (Figure 4.2a). In BET, inert adsorbates such as nitrogen are adsorbed to measure the surface area of a mesoporous material; the BJH transformation uses the Kelvin equation to relate the amount of adsorbates removed with changes in pressure to pore sizes. In the pore-size distribution, we see that the features from nanocrystalline TiO$_2$ interstices (around 10 nm) and the mesopores from the native porogen Pluronic F127 (around 30 nm) are preserved at the addition of ethylcellulose. Larger pores, at around 50 nm peak value with pores reaching larger than 100 nm, appear with the addition of excess ethylcellulose. Ethylcellulose also acts to increase viscosity, leading to increased thickness during spincoating. For a particular modification, half

dilution in ethanol of F52C, (see Appendix A), having half the TiO_2 content as that of an unmodified paste, the resulting film thickness remains the same. Apart from the BET data, this intuitively means that modified TiO_2 films have larger total pore volumes.
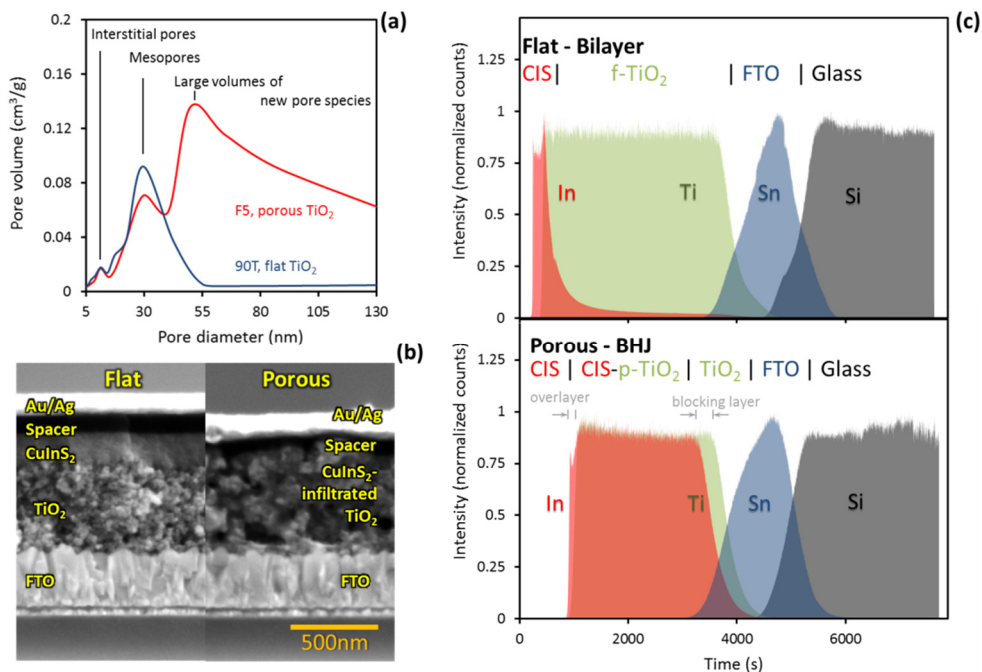
Figure 4.2 Increase in TiO_2 porosity and the infiltration of CIS QDs. (a) Pore diameter distribution (BJH transformation of BET curves) showing large volumes of new pore species. (b) Cross-sectional SEM images of a CIS on flat-TiO_2 device (left) and a CIS-infiltrated porous TiO_2 device (right). (c) Secondary ion mass spectra of flat (top) and porous (bottom), highlighting key elements in each layer. This shows deep infiltration in porous devices.

Even when the nanocrystals have small sizes (3.2 nm), no infiltration occurs when pores are 30 nm or less in size. In Figure 4.2b, cross-sectional images of completed devices reveal that for the unmodified 90T paste, a thick NC absorber rests on top of an assembly of particles as in Figure 4.1. When excess ethylcellulose is added, no thick absorber layer forms and an assembly of particles with more rounded features is seen. These more rounded features are TiO_2 coated with CIS NCs. We probed the extent of CIS infiltration by depth analysis of key elements via secondary ion mass spectrometry (SIMS). In SIMS,

primary ions are focused onto the sample surface to sputter out ions of the material. These sputtered ions are separated by their masses and collected over time; species can be identified by their mass spectra. We see that indium (from CIS) are not detected simultaneously with titanium (TiO_2) in flat devices while for CIS in porous TiO_2, indium is detected alongside titanium and remains constant. This signifies that the infiltration is uniform. Note that the titanium signal falls off later than indium. This accounts for the thin (~50 nm) TiO_2 blocking layer which we have placed to prevent shorting of CIS with FTO.
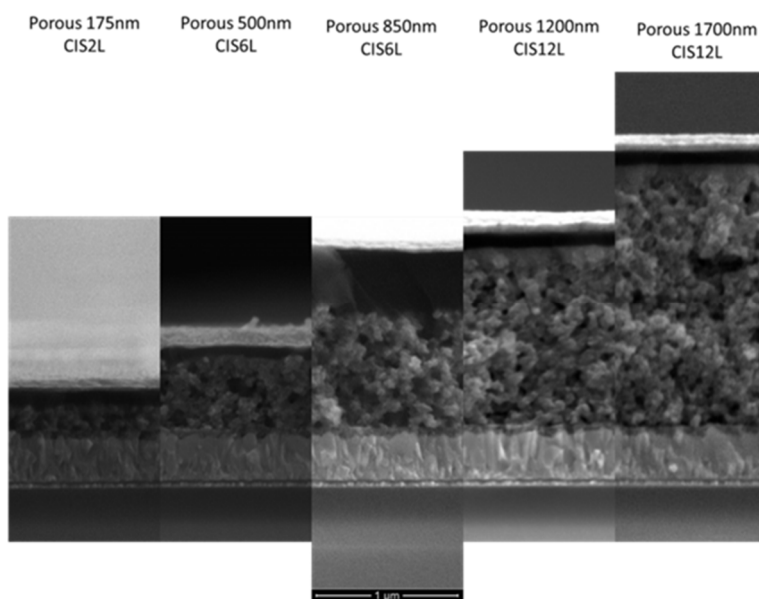
Figure 4.3 Thickness control of the TiO₂ porous network. Cross-sectional SEM images of various thicknesses of porous TiO_2. The thickness of the porous TiO_2 network can be tuned by dilution of the F52C solution: 1 : 3 vol. F52C with ethanol, 175 nm; 1 : 1 vol., 500 nm; 1 : 0.3 vol., 850 nm; 1 : 0.15 vol., 1200 nm; undiluted, 1700nm. Thicker films are more prone to delamination and cracking.

These new larger pores allow for the infiltration of CIS and enable us to form blends of both materials. We can control the thickness of these blends by varying the viscosity of the modified TiO_2 solution, through higher concentrations of ethylcellulose and TiO_2. Keeping the ratio of added ethylcellulose to TiO_2 content constant, we can vary the thickness of TiO_2

porous network from 175 nm to 1700 nm. At least for porous TiO_2 with a thickness of 850 nm, CIS penetrates until the blocking layer (Figure D1). With thicker porous layers however, films suffer from cracking and delamination.

4.2 From bilayer to BHJ solar cells: improvements on device performance

We used these films to fabricate bilayer (flat TiO_2) and BHJ (porous TiO_2) devices. In contrast to devices in Chapter 3, we have included spiro-MeO-TAD to act as a spacer between the CIS layer and the gold contact. It might appear that these solar cells show the same structure as solid-state semiconductor-sensitized solar cells, but solar cells without it have the same performance (See Figure D2), and this layer has been added as a practicality solely to reduce shorting particularly in BHJ devices. BHJ devices have improved IV characteristics (Figure 4.4a) showing an improved FF, J_{SC}, V_{OC} (Table 4.2) and no cross-over in the dark and light curves. This crossover in the current-voltage curve (IV) has been attributed to high charge barriers in CIGS devices[177]. In the previous chapter, devices with thinner CIS films have similar total J_{SC} with those having thicker CIS films, which we have attributed due to TiO_2 having a greater contribution to the photocurrent in thinner CIS film devices. And it might be argued that BHJ devices have improved photocurrent contribution from TiO_2. But we find this to be not the case, as when devices have been illuminated with 400 nm-filtered light, the J_{SC} increase in the BHJ architecture becomes even more stark, at more than twice the photocurrent under full sun and at more than 5 times under filtered light.

The BHJ architecture allows us to exceed a PCE of more than 1% whereas for bilayers, we were limited to PCEs below 0.5% (Table 4.2). This is brought about by an increase in the J_{SC} and the FF. In Figure 4.4b, the J_{SC}s of BHJ devices are statistically higher than those of bilayer devices for different zinc contents. In Chapter 3, we found that the J_{SC} increased with decreasing zinc content but found a limitation that zinc contents lower than 0.1 Zn posed dispersibility issues. In BHJs, even without lowering the zinc content, J_{SC}s are already higher than that of 0.1 Zn CIS bilayer devices. In addition, we mentioned in the previous chapter that despite the effects of Zn on J_{SC}, FFs remain low, at around 30%. This poor performance is overcome in BHJ devices with FFs having an average of 50%.
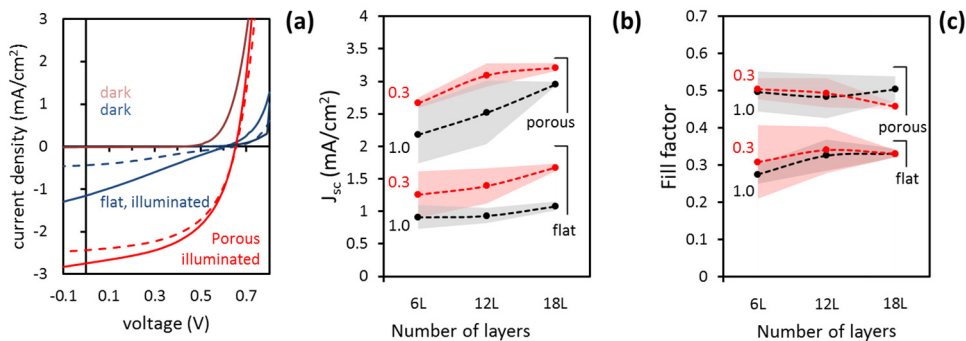
Figure 4.4 Improvements in device performance with respect to device architecture. (a) Dark and illuminated current-voltage curves of CIS 0.3 Zn on flat bilayer (blue) and porous TiO$_2$ BHJ (red) devices. Dashed lines correspond to current-voltage characteristics under 400nm-filtered light. (b) J$_{sc}$ and (c) FF of devices with different numbers of deposited CIS layers (6L, 12L, 18L), Zn content (1.0, 0.3 Zn) and types of titania (flat, porous), error bars shown as shaded regions.

Table 4.1 Device performance of CIS with different Zn content in bilayer and porous devices (f-TiO$_2$, flat TiO$_2$; p-xxx, porous TiO$_2$ xxx nm thick)

Zn	layers	TiO$_2$	V$_{oc}$	J$_{sc}$	FF	PCE
1.0	6	f-TiO$_2$	0.59	0.91	0.27	0.15
1.0	6	p-500	0.60	2.18	0.50	0.65
0.33	6	f-TiO$_2$	0.63	1.26	0.31	0.23
0.33	6	p-500	0.65	2.66	0.52	0.87
0.33	12	p-850	0.67	3.83	0.39	1.01
0.33	12	p-850	0.70	4.32	0.38	1.16[a]
0.1	6	f-TiO$_2$	0.63	1.81	0.26	0.30
0.1	6	p-500	0.67	1.82	0.36	0.44

[a]champion device

59
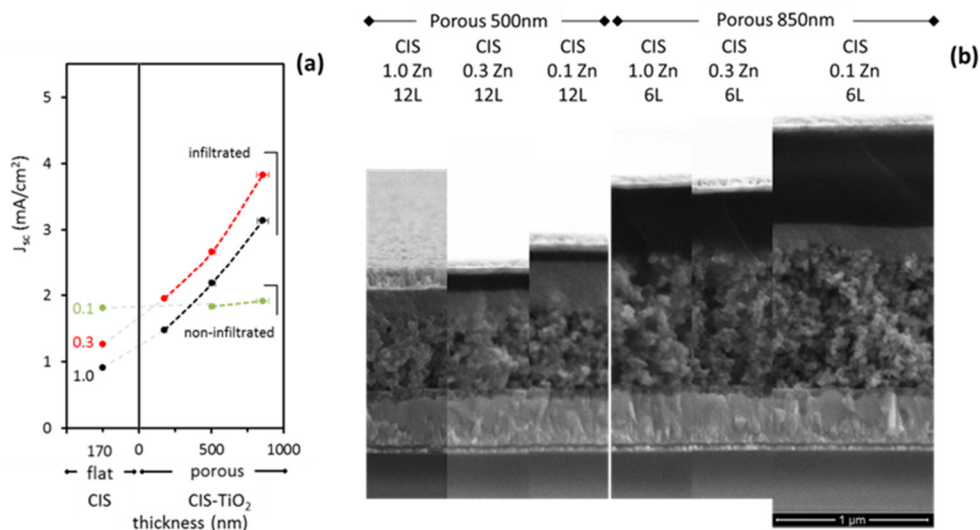
Figure 4.5 Effect of BHJ thickness and Zn-content. (a) The J_{sc} of devices from CIS of various Zn content (1.0 Zn, 0.3 Zn and 0.1 Zn) deposited on flat TiO_2 and infiltrated into porous TiO_2 of at different TiO_2 thicknesses. (b) CIS 1.0 Zn and CIS 0.3 Zn similarly infiltrate the porous TiO2 resulting in comparable overlayer formation. CIS 0.1 Zn does not infiltrate the porous material, seen for two thicknesses (CIS 0.1 Zn 12L on 500nm porous TiO2 and CIS 0.1 Zn 6L on 850nm porous TiO2) and and is seen resting on top of the structure.

We have shown that we can engineer the CIS CQD solar cell architecture: by being able to vary the Zn content of NCs, by regulating the thickness of CIS absorber layers and by controlling the thickness of blend layers through porous-TiO_2 thicknesses. With these parameters, we aimed to optimize the device performance. We see that the short circuit density increases with the thickness of this blended material (Figure 4.5a) for CIS with 1.0 Zn and 0.3 Zn. This increase in current is already evident for CIS-TiO_2 blend thicknesses of only 175 nm. For 0.1 Zn however, while we expected that it would lead to optimum conditions having displayed the highest J_{SC} in a bilayer device, it does not benefit from TiO_2 porosity. In fact, J_{SC} is invariant with porous TiO_2 thickness (Figure 4.5a).

From cross-sectional SEM (Figure 4.5b), CIS 1.0 Zn and CIS 0.3 Zn infiltrate the TiO_2 network comparably, forming similar overlayer thicknesses. CIS 0.1 Zn however does not infiltrate the porous network: rather it just builds up on its surface, resulting in a thickness as if it were grown on flat substrates.

60

These confirm that it is not the porosity of TiO_2 but that the infiltration of CIS in this network results in better device performance.
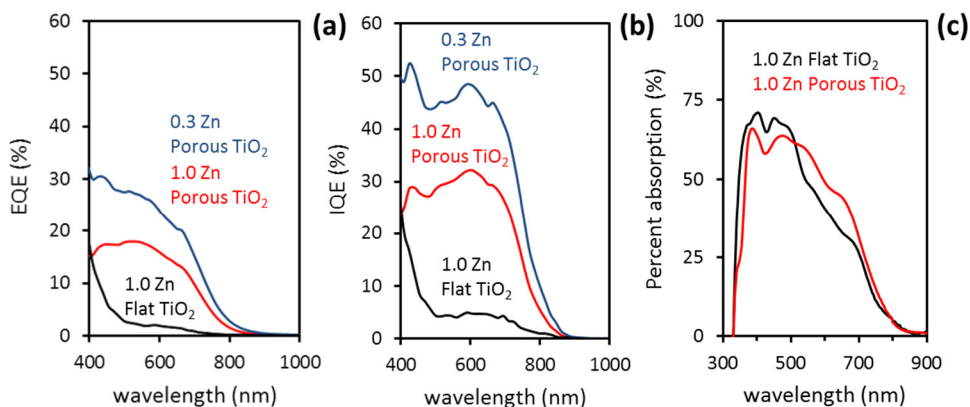
Figure 4.6 Absorption and spectral quantum efficiency of devices. The (a) EQE and (b) IQE spectra of devices based on 1.0 Zn CIS on flat TiO_2 (black), 1.0 Zn CIS on 500nm-porous TiO_2 (red) and 0.3 Zn CIS on 500nm-porous TiO_2 (blue). (c) Total device absorption of flat and porous devices showing comparable absorption.

In bilayer devices, we predicted an internal quantum efficiency (IQE) of 4.5% (section 3.7) and attributed this to poor charge collection in the CIS CQD solid absorber layer. This IQE is confirmed in Figure 4.6. BHJ devices, having higher currents demonstrate higher external quantum efficiencies (EQE) as in Figure 4.6a. These EQEs result in higher predicted short-circuit currents than what is observed under full sun[j], most probably resulting from an intensity dependence of the J_{SC}. A blend thickness of 500 nm leads to comparable full device absorption as that of a bilayer device with 180 nm CIS absorber thickness (Figure 4.6c); this results in a ten-fold increase in IQE. The IQE improvement reveals that the increase in J_{SC} is not due to an increase in device absorption but rather an improved charge collection from the CIS absorber layer over bilayer devices.

---

[j] The predicted Jsc from the EQE of 1.0 Zn CIS flat TiO_2, 1.0 Zn CIS porous TiO_2 and 0.3 Zn porous TiO_2 are 0.58, 3.34 and 5.27 mA/cm² respectively—being much higher than the J_{sc} at 400nm-filtered illumination: 0.27, 2.13, 2.43 mA/cm² respectively.

We have not commented extensively on the stability of these devices as this lies out of the scope of this work. We do observe that BHJ devices are more stable than bilayer ones under illumination: the J_{sc} of BHJs increasing and saturating to an additional 30% of its initial value at $t = 0$, while that of bilayers continually decrease until 60% of its original value (Figure D3). Comparisons for the performance throughout this work has been taken at $t = 0$ for both bilayer and BHJ devices.

4.3 Performance increase from reduced trap-assisted recombination

The improved performance of the blended architecture of CIS-infiltrated TiO_2 is caused by reduced trap-assisted recombination. By illuminating the devices at different intensities (suns) and probing the V_{OC} (Figure 4.7a) and the J_{SC} (Figure 4.7b), we see that bilayer and BHJ devices exhibit different behaviors. The Suns-V_{OC} curve (Figure 4.7a) can give a value of the light ideality factor n_{id}, through the Shockley relation

$$V_{OC} = \frac{n_{id}\, kT}{q} \ln(\varphi) + C$$
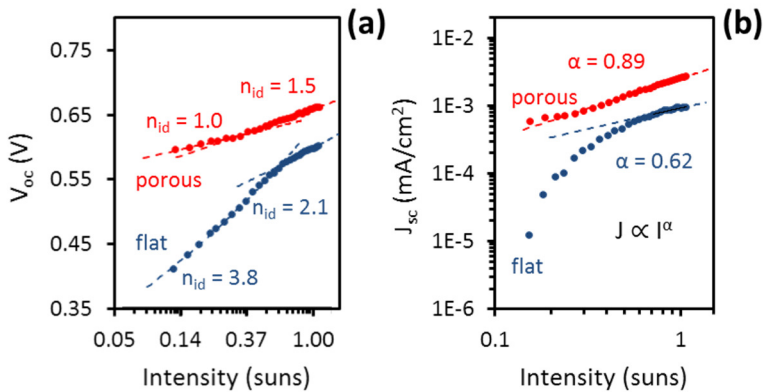
Figure 4.7 Intensity dependence of V_{oc} and J_{sc} (Suns-V_{oc}, Suns-J_{sc}). The (a) suns-V_{oc} and (b) suns-J_{sc} of CIS 0.3 Zn in a bilayer with TiO_2 and in a BHJ showing enhancement in ideality factor and a power law dependence closer to unity.

where k, T, q, φ and C are the Boltzmann constant, temperature, electron charge, light intensity and constant respectively. The ideality factor n_{id} is proportional then to the slope of the natural logarithm of the intensity against V_{OC}. Ideality factors n_{id} close to unity indicates band to band recombination is dominant and with $n_{id}>1$, trap-assisted recombination.
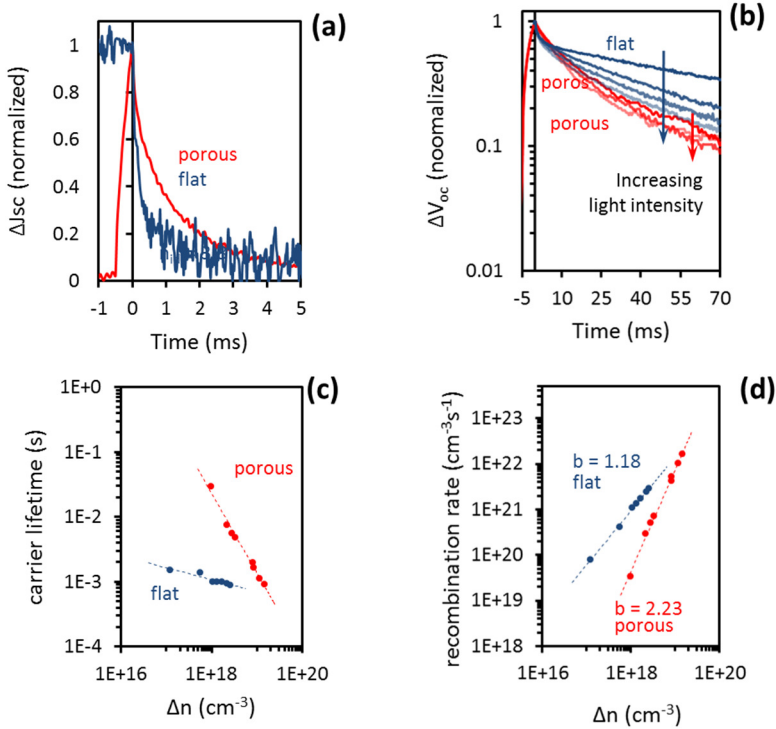
Figure 4.8 Transient photocurrent and photovoltage characteristics. (a) Normalized transient photocurrent and (b) transient photovoltage of flat and porous devices at select bias light intensities. Porous devices have longer J_{sc} decay and V_{oc} decay and are single exponential and do not show any long-lived trapped features in the 25-70 ms range. The Voc decay time is taken from the short time scales, 0-10ms. (c) Carrier lifetime and (d) recombination rate vs excess charge carrier density of bilayer and BHJ devices giving two clearly different slopes which relate to their recombination order b.

Two regimes appear in both bilayer and BHJ devices: at low intensity conditions and at conditions close to 1 sun. In both these regimes, the BHJ device demonstrates near-invariant n_{id}s (low, 1.0; high, 1.5) that are much closer to 1. Bilayer devices show n_{id}s hinger than 2 and much poorer n_{id} at low light

intensity (low, 3.8; high, 2.1). This large deviation from unity points to trap-assisted recombination being dominant in bilayer devices. Furthermore, the suns-J_{SC} (Figure 4.7b), can also be used to gain insight into the device operation, by fitting it with a power law,

$$J \propto I^{\alpha}$$

with the power law exponent α close to 1 being a mark of ideal generation-limited solar cells, 0.75 for space-charge-limited recombination and 0.5 for trap assisted recombination routes[178]. Again, we see that two regimes appear, one for low light and another for close to 1 sun conditions and that for BHJ devices, there is little difference in these regimes. BHJ devices give a close to ideal $\alpha = 0.89$, while bilayer devices yield $\alpha = 0.62$, agreeing with the suns-V_{OC} finding that bilayer devices suffer from trap-assisted recombination.

Transient photocurrent, TPC (Figure 4.8a) and photovoltage, TPV measurements (Figure 4.8b) further support these claims. The transient photovoltage (Figure 4.8b) of bilayer devices shows a bi-exponential decay, having a short lifetime from 0-10 ms and an extremely long one from 25 ms onwards. This extremely long exponential decay, whose contribution to the transient photovoltage lessens with decreasing light intensity, we attribute to trapped carriers which maintain the quasi-Fermi level difference for a much longer time. In BHJ devices, having a longer lifetime in the 0-10 ms range, the transient photovoltage is near single exponential for all light intensities. This longer photovoltage decay coupled with the longer photocurrent decay of BHJ devices (Figure 4.8a) leads to the observed improved current density. From the TPC and TPV curves, it is possible to calculate the carrier lifetime, recombination rate, excess charge carrier density generated by the laser pulse and the Urbach energy (see Appendix D). For a given excess charge carrier density, the carrier lifetime in BHJ devices is higher, which consequently leads to a much lower recombination rate (Figure 4.8c, d). From Figure 4d, the slope in the double-log plot predicts the recombination order of the device, the recombination rate being proportional to orders of excess carrier concentration:

$$R \propto K_1(\Delta n) + K_2(\Delta n)^2 + K_3(\Delta n)^3$$

with K_n being recombination constants. The first order pertains to trap-assisted recombination; the second, radiative recombination and the third, Auger recombination. Bilayer devices devices have a recombination order b close to 1 while BHJ devices have a b value close to 2 (Figure 4.8d). Consistent with the results presented thus far, we see a shift from a device performance experiencing loss from trap-assisted recombination in flat devices to a more ideal solar cell seen in BHJ devices.

4.4 A lower E_U for extracting holes in deep tail states: a proposed model

These traps leading to poorer performance in bilayer devices can be treated as a density of tail states in the CIS energy gap. We propose that the available density of these states shifts in the presence of TiO_2. Before collection or transport, when photogenerated charges relax into these states, an activation energy E_U or the Urbach energy is needed to be overcome to bring them to an energy E_t that would allow for transport. Likewise this Urbach energy is the mean energy of the exponential distribution of available states beyond the band edges. We have calculated the Urbach energy (Figure 4.9a) by fitting the tail region of the EQE[179,180]. As well, alternative estimations of the Urbach energy can be obtained from the carrier lifetime and excess carrier density against open-circuit voltage[181] (see Appendix D). We see that bilayer devices require much higher activation energies (~160 meV) to remove charges from these tail states than in BHJ devices (80 meV). While the calculation of E_U values through different methods[182] leads to different values, the trend is similar using other E_U estimations (Appendix D)—that the BHJ devices show lower E_U than flat ones.

This difference in E_U is supported by looking at the photoluminescence in these devices. We performed micro-Raman-photoluminescence to look into the emission of thin layers (~25-75 nm) of CIS deposited on flat and porous TiO_2 (Figure 4.9b). When the CIS layer is thin (~25 nm), the emission peaks at 847 nm in both flat and porous devices. However, when slightly thicker CIS (~75 nm) is deposited, flat devices have a peak that is farther into the infrared at 886 nm, whereas that from porous devices remains unchanged. This PL shift corresponds to a 64meV difference and agrees well with the difference in we have seen from the Urbach energy.
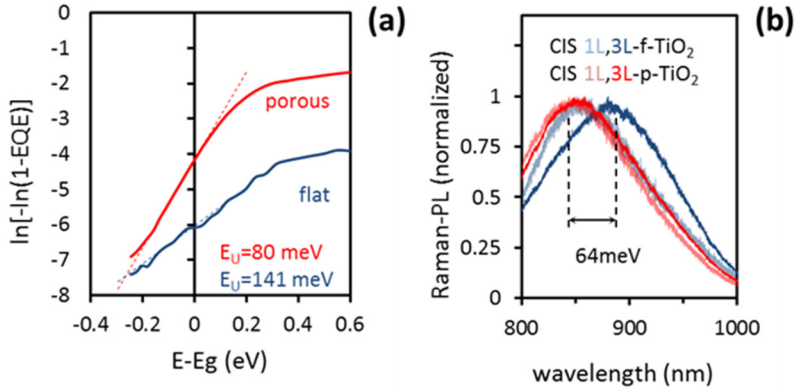
Figure 4.9 Urbach energy and photoluminescence shifts. (a) Urbach energies as calculated from the EQE spectra, with porous devices show lower E_U. This change in the Urbach energy is seen in the photoluminescence shift in the (b)Raman-PL of completed devices.

We suspect that TiO_2 provides non-photogenerated electrons to quench holes which enter the deep tail states in CIS. We posit that these tail states are close to the valence band. Shabaev et. al. calculated from theoretical models that hole levels near the degenerate valence band contribute to long absorption tails[138]. This model however implies that the unique photoluminescence of CIS is inherent to its band structure and not due to defect states. We have mentioned that there is still no clear consensus on the PL mechanism in CIS[139]: as donor-acceptor emission, as quantum-confined conduction band to acceptor level transition, as donor level to quantum-confined valence band transition, or as an inherent property due to the band structure. We believe though that the nanocrystals emit through a transition between quantum-confined conduction band to acceptor level, considering the extent to which the emission can be tuned[170] and that the conduction band minimum shifts to a greater extent than the valence band maximum with changes in size (Figure 3.5a). Further, in completed CIS devices, Halpert, et. al. suggested that deep trapping of holes[123] could be responsible for low fill factors. In support of this, it was suggested that upon the photogeneration of carriers, holes become delocalized through self-trapping[183]. Whether it be due to inherent long tails or dense trap levels forming a distribution, we find it reasonable to place these tail/dense trap states near the valence band of the CIS CQD solid (Scheme 4.1).

66

Because of poor transport and a built-in field that resists the injection of electrons into CIS, TiO$_2$ can only provide electrons for a finite thickness which is at least 25 nm into the CIS film (Figure 4.9b). In BHJ devices where the pore size has a mode around 50 nm (Figure 4.2a), CIS will be easily accessed by TiO$_2$ for injection. These injected electrons quench holes which enter the deeper tail states. In turn, this shifts the mean of the distribution (E$_U$) of occupied tail states much closer to the valence band, lowering the activation energy needed to remove carriers from these states and would shift the photoluminescence to higher energies.

Scheme 4.1 Quenching of holes CIS by TiO$_2$. TiO$_2$ fills tail states near the valence band of CIS more effectively in BHJ devices, leading to improved carrier extraction due to a lower Urbach energy.
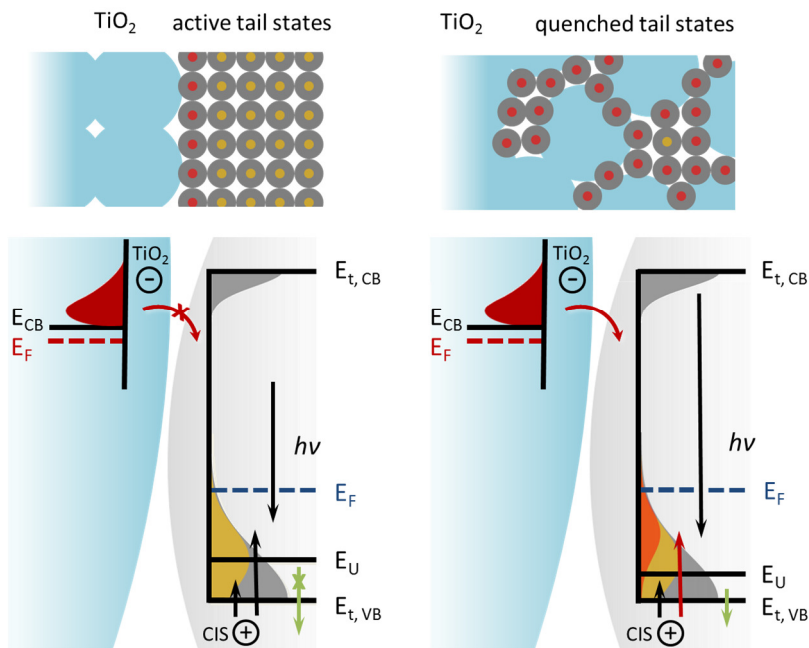
We consider two other plausible models, exciton splitting and field extraction, to describe the device operation. It has been suggested in Chapters 2 and 3 that CIS might have high binding energies. While it is possible that the interface provides energy to split excitons and that in BHJ devices there is a

higher interface area, we find that the J_{SC} increases with increasing thickness (Figure 3.8b) and that there is no reduction in the photoluminescence in porous devices (Figure 4.9b). As well, it might be argued that the high built-in field would provide sufficient energy to drive out trapped carriers; however, because of lower fields at lower intensities this would entail a turnover in the photovoltage decay characteristics from being 2-exponential at low intensities to 1-exponential at higher ones, whereas we see that it is single-exponential for all intensities in BHJ devices (Figure 4.8b, low intensities shown). The proposed model of shifting of the distribution of occupied tail states through electron injection is different from passivation by ligands wherein adsorbed static molecules render trap states inaccessible. This provides a dynamic cycling of non-photogenerated charges to quench deep tail states in the energy gap.

In summary, we have fabricated non-annealed bulk heterojunction solar cells of colloidally synthesized CIS nanocrystals with nanocrystalline TiO_2 by increasing the pore size of the TiO_2 network. This leads to uniform and deep infiltration of the CIS NCs. By using a BHJ architecture, we improved the performance of CIS CQD solar cells: mainly from an increase in J_{SC} and FF leading to a six-fold increase in efficiency from initially at 0.15% to 1.16% PCE. From analysis of Suns-V_{OC}, J_{SC} and TPV, TPC measurements, we have identified that BHJ devices have less trap-assisted recombination and a lower activation energy (E_U) for hole extraction. We suggested that BHJ devices allow for better quenching of deeper tail states in CIS by the transfer of electrons from TiO_2.

CONCLUSIONS AND OUTLOOK

Solar energy conversion technology will revolutionize the energy market but is currently faced with obstacles for its wide scale deployment: cost, operational lifetime, power conversion efficiency (PCE), material abundance and toxicity. Solid-state solution-processed nanocrystalline solar cells are newcomers in the field dominated by silicon, but has already shown efficiencies of more than 10% PCE in a little over a decade. Solution-processing allows this technology to be adaptable to almost any surface and allows facile control over film properties and device morphology. This technology is still based on PbS and the field requires us to look for less toxic nanocrystal alternatives.

Copper indium sulfide (CIS) nanocrystals (NCs) are promising materials that have proven high PCEs in the bulk as annealed thin films and in sensitized solar cells as adsorbed absorbers. There is still a gap between the performance of CIS NCs in these devices and in colloidal quantum dot (CQD) solar cells. This work aimed to be a significant step closer in filling this gap by addressing the following issues which we have identified at the start of this thesis:

Processability of CIS NCs: High quality films are necessary for CQD solar cells. The conventional synthesis of CIS NCs leads to the formation of an organic shell, dodecanethiol, that is difficult to remove, posing a hindrance to carrier transport in the assembled NC solid. We introduced a synthetic scheme that does not incorporate dodecanethiol. We tuned the synthetic scheme,

selecting appropriate ligands and precursors, reaction times and isolation protocols, leading to materials with controlled size and optical properties. By performing a thorough characterization on the structure of the product, we proposed that it is a copper-poor material and is decorated by zinc and indium. This allowed us to rationally plan a ligand exchange strategy using hard ligands to form solid-state CQD films. This is an important step for fabricating optoelectronic devices from colloidal NCs.

Device architecture for CIS CQD solar cells: Solid-state CIS-based solar cells still borrow heavily from device architectures in thin film chalcogenide solar cells, using CdS as a buffer layer. We found that CIS NCs form a heterojunction with TiO_2 with large depletion widths. Being solution-processed, we gain access to different device architectures easily: such as the bilayer, as two distinct material-layers in contact and the bulk heterojunction (BHJ), as having a layer with intimately mixed material-components. The BHJ structure was achieved by increasing the pore sizes of TiO_2. The shift from a bilayer to a BHJ structure had led to drastic increase in short circuit photocurrent densities (J_{sc}s) and fill factors (FFs). Through optimization, we increased the efficiency from 0.15% PCE in bilayer devices to 1.16% in BHJ devices.

Limitations of the CIS CQD solar cell: Much of the advancement in CQD PV has been brought about by an understanding of the device operation and the properties of the CQD film. We have shown that assemblies of CIS NCs couple to each other as seen in changes in PL lifetimes with distance. We fabricated thin film field effect transistors and photodetectors to look into the charge transport in the CQD film. These films have low mobilities (~10^{-5} $cm^2V^{-1}s^{-1}$) and show features which signify high trap densities. Bilayer devices were seen to suffer from trap-assisted recombination and from high activation energy for charge

extraction. The poor transport of carriers is confirmed by the low internal quantum efficiency of bilayer devices. We overcome this issue through the use of a BHJ architecture. We suggested that BHJ devices allow for better quenching of these trap states, treated as deeper tail states from the valence band of CIS, by the transfer of electrons from TiO_2.

In this work, we have started from synthetic precursors, to analyzing the formation, structure and surface of formed CIS NCs. We have formed films which allowed us to fabricated devices: field effect transistors, photodetectors, bilayer and BHJ solar cells. In each step, we have identified material, film and device properties which will be necessary for good device performance. Ultimately this work aims to stimulate new interest in further development of CIS CQD solar cells.

Copper indium sulfide NCs are candidate materials which could possibly compete with PbS NCs as in CQD solar cells if the optoelectronic quality of solution-processed films, whose deposition we have already shown to be possible through a thiol-free synthesis, can be improved, in particular with respect to trap densities and carrier mobilities. As with PbS, the control on surface ligands can be a route for tuning both these properties.[59] Further, it has been shown that in CZTS, a similar system to CIS, Ag alloying[184] leads to reduced band tailing and a smaller Urbach energy. Apart from the formation of the Zn:CIS alloy which we have also discussed in this work, no alloying or heterovalent doping has been reported for CIS nanocrystals. An alloying or doping strategy then that would suppress the formation of states near the valence band, which is most likely from V_{Cu}, will be beneficial.

The bulk heterojunction is a useful platform for utilizing materials with poorer electronic properties, and we have proposed a new scheme by which it can be advantageous for CQD solar cells. This structure still depends on the mobility of individual materials and an infinite layer thickness is not possible. Efficient structuring with ordered and monodisperse pores and a thick crack-free film will improve performance by preventing occlusions.

While this work has focused on CIS NCs, other non-toxic materials are set to expand the repertoire of NC materials for photovoltaics. In particular, $AgBiS_2$ NCs as a CQD solid absorber has debuted, already with a PCE of more than 5%. This material is exciting as thicknesses are just below 50 nm. However, like CIS NCs, much still has to be investigated—such as characterizing film properties, identifying passivation strategies and device operation—in order for its use in competitive CQD solar cells based on non-toxic elements.

APPENDIX A
Materials and Methods

Chemicals and stock solutions. Copper(I) iodide (CuI) 99.999%, indium(III) chloride (InCl$_3$) 99.999%, zinc(II) acetate dihydrate (Zn(OAc)$_2$ · 2H$_2$O) 98%, bis(trimethylsilyl) sulfide (TMS) synthesis grade, trioctylphosphine (TOP) 97%, oleylamine (OlAm) 70%, oleic acid (OA) 90%, 1-octadecene (ODE) 90%, formic acid 90%, mercaptopropionic acid (MPA) ≥99%, propionic acid 99.5%, pentanoic acid 99% and tetradecanoic acid 99%, ethylcellulose: 46 cP (5 % in 80:20 toluene/ethanol), oxalic acid 99%, glutaric acid 99%, pimelic acid 98%, titanium tetrachloride (TiCl$_4$) 99%, titanium isopropoxide 97%, bis(trifluoromethane)sulfonimide lithium salt (LiTFSI) 99.95%, anhydrous chlorobenzene 99.8% and 4-tert-butylpyridine (TBP) 96% were purchased from Sigma Aldrich Co. LLC. Apart from OlAm and ODE, all chemicals were used without further purification. OlAm and ODE were dried by heating the chemicals under vacuum at 80°C for more than six hours and afterwards kept in a drybox along with TMS for future use. Reagent grade sodium hydroxide, isopropanol, ethanol, acetone, methanol, acetonitrile, toluene and concentrated hydrochloric acid (HCl), were purchased from Panreac Quimica SLU; 90T titania paste from Dyesol Ltd.; spiro-MeO-TAD livilux™ SHT-263 from Merck & Co. Inc.

Various stock solutions were prepared beforehand and are described as follows. 1M TiCl$_4$ stock solution: 125mL deionized water and 20.85mL

concentrated HCl were placed in a flask in an ice bath. Under stirring, 27.5mL TiCl$_4$ was added dropwise. The solution was stirred until it was clear and stored and kept below 0°C until future use. TiO$_2$ blocking layer: a weakly acidic solution of titanium isopropoxide was prepared by mixing 369µL titanium isopropoxide into 2.53mL isopropanol. To this, 2.53mL isopropoxide with 35µL 2M aqueous HCl was added dropwise. This solution was used fresh. F52C stock solution (90T and ethylcellulose): equal volumes of diluted 90T paste (1:1.25wt 90T with ethanol) and 10%wt ethylcellulose in ethanol were combined and vortexed. Spiro-MeO-TAD solutions: a 45mg/mL spiro-OMeTAD in chlorobenzene was prepared. 800µL of this solution was combined with a dopant solution containing 15µL 85mg/mL LiTFSI in acetonitrile and 10µL TBP.

Synthesis of CIS-Zn-OA 3.2-nm diameter nanocrystals. 1.5mmol CuI (0.285g) and 1.5mmol InCl$_3$ (0.330g) were weighed inside a glovebox and placed in a sealed flask. To this, 7.5mL TOP, 15mL ODE and 9mL OlAm were added and the flask was connected to a Schlenk line outside the glovebox. This was allowed to react for 30 minutes at 95°C under vacuum to form a clear solution. The flask environment was switched to that of argon and was raised to 170°C. At this temperature, 1.5mmol TMS (310µL) in 7.5mL ODE was injected. Upon injection of the sulfur precursor, the color changed from clear, to yellow, to orange, to red and finally to black. The flask temperature naturally lowered to 150°C and the reaction was continued for 15 minutes at that temperature. To separate the product, CIS-OlAmTOP, from the reaction, 5mL toluene and then 70mL ethanol were injected into the flask. This mixture was centrifuged at 3500 RPM for 5 minutes. The supernatant was decanted and the pellet redispersed in 6mL toluene.

In another flask, 3mmol Zn(OAc)$_2$ · 2H$_2$O (0.659g), 6mL ODE and 3mL OA were heated to 100°C for 30 minutes under vacuum forming a clear solution. The flask environment was switched to that of argon and 6mL of the isolated CIS-OlAmTOP NC solution was injected. The environment was returned to vacuum and the solution was reacted for 30 minutes at 100°C. To separate the product, CISZn-OA NCs, from the reaction, 5mL toluene and then 40mL acetone were injected. The mixture was centrifuged at 3500 RPM for 5 minutes. The supernatant was decanted and the pellet was redispersed in 4mL

74

toluene. This solution was again centrifuged after which the supernatant instead was collected and the pellet discarded. To this, 10mL of methanol was added and the mixture centrifuged. Next, the supernatant was discarded and the pellet was redispersed in 2mL toluene and then precipitated with 5mL methanol. After centrifuging, the supernatant was discarded and the pellet dried with a stream of nitrogen, redispersed in 2mL toluene and centrifuged. Afterwards, the supernatant was kept. This usually results in solutions at 85 mg/mL concentrations.

Synthesis of CIS-Zn-OA Nanocrystals with diameters smaller than 3.2-nm. Keeping the same quantities of reagents and reaction times, we reduced the particle size by lowering the injection temperature of the sulfur precursor. These injection temperatures ranged from 50°C to 150°C, at 20°C intervals and resulted in final solutions which were light yellow to dark red. At lower injection temperatures, the nanocrystals were grown at the temperature where the solution naturally cools at injection and were treated with zinc oleate at their growth temperature if this temperature was less than 100°C. Being smaller particles, the products were isolated by a higher non-solvent to solvent ratio. The quantities used are tabulated in Table A1.

Porous and dense TiO$_2$ electrodes. Densely packed TiO$_2$ nanocrystalline electrodes were fabricated by spincoating a diluted solution of 90T paste (1:2.5 wt. 90T with ethanol) on cleaned, masked 12mm x 12mm FTO-coated glass (Pilkington TEC 15, Xop Glass) at 3000RPM using a Specialty Coating Systems 6800 series spin-coater system for 30 seconds. These films were then annealed in air starting at 100°C with 100°C increments, holding for 15 minutes at each increment. At 500°C, the film was annealed for an hour at that temperature and then allowed to cool naturally. To improve the connectivity between the TiO$_2$ nanocrystals, the annealed films were immersed for 20 minutes in a 70°C bath of 40mM TiCl$_4$, prepared by aqueous dilution from a 1M TiCl$_4$ stock solution. The films were then dried and annealed using the previously described annealing profile.

Table A1 Experimental details for the synthesis of $CuInS_2$ nanocrystals of different sizes

Injection	Growth	Growth	Isolation	dispersion	Coating	Coating	isolation	1st wash	2nd wash	dispersion
50°C	45°C	15min	3mL tol 105mL EtOH	6mL tol	45°C	30min	2.5mL tol 40mL acet	4mL tol 20mL MeOH	2mL tol 10mL MeOH	2mL tol
70°C	60°C	15min	3mL tol 90mL EtOH	6mL tol	60°C	30min	2.5mL tol 40mL acet	4mL tol 20mL MeOH	2mL tol 10mL MeOH	2mL tol
90°C	75°C	15min	3mL tol 75mL EtOH	6mL tol	75°C	30min	3mL tol 40mL acet	4mL tol 16mL MeOH	2mL tol 8mL MeOH	2mL tol
110°C	90°C	15min	4mL tol 90mL EtOH	6mL tol	90°C	30min	3mL tol 40mL acet	4mL tol 10mL MeOH	2mL tol 5mL MeOH	2mL tol
130°C	110°C	15min	5mL tol 90mL EtOH	6mL tol	100°C	30min	4mL tol 40mL acet	4mL tol 10mL MeOH	2mL tol 5mL MeOH	2mL tol
150°C	130°C	15min	5mL tol 80mL EtOH	6mL tol	100°C	30min	5mL tol 40mL acet	4mL tol 10mL MeOH	2mL tol 5mL MeOH	2mL tol
170°C	150°C	15min	5mL tol 70mL EtOH	6mL tol	100°C	30min	5mL tol 40mL acet	4mL tol 10mL MeOH	2mL tol 5mL MeOH	2mL tol

Porous TiO$_2$ nanocrystalline electrodes were fabricated by first spincoating (3000RPM, 30s) on cleaned FTO-coated glass a weakly acidic solution of titanium isopropoxide which was then annealed using the previous annealing profile to deposit a dense 50nm-TiO$_2$ blocking layer. On top of this blocking layer, a combined solution (F52C) of diluted 90T paste and an ethanolic solution of ethylcellulose was spincoated (3000RPM, 30s) and annealed. This paste (F52C) was diluted accordingly to control the thickness of the porous layer, with a 50% dilution in ethanol leading to a thickness of 500nm. A densification step was performed to improve the connectivity between the TiO$_2$ nanocrystals; the annealed films were immersed for 20 minutes in a 50°C bath of 10mM TiCl$_4$, prepared by aqueous dilution from a 1M TiCl$_4$ stock solution. The films were then dried and annealed.

Ligand exchange and phase transfer. Films of this material were deposited via a layer-by-layer (LbL) solid state ligand exchange process on various substrates such as glass, 285nm thermally grown silica on degenerately p-doped silicon (Si-Mat) or interdigitated gold electrodes on glass cleaned by sequential 15-minute sonication in soapy water, acetone and isopropanol and dried with a stream of nitrogen. The nanocrystal solutions were diluted to a concentration of 25mg/mL. The layer started by spincoating the material on selected substrates at 2000 RPM for 30 seconds using a Specialty Coating Systems 6800 series spincoater system. Then whilst spinning, a drop of 2%vol formic acid in methanol was reacted with the film for another 30 seconds. The layer ended with 5 drops of methanol and 5 drops of toluene, resulting in 30nm thick films. Thinner films were achieved by reducing the nanocrystal concentrations.

Solutions can be transferred from a non-polar solvent, such as toluene, to a polar solvent such as water by exchanging the oleic acid on the surface with MPA. In a typical process, 1mL of 1mg/mL of CISZn-OA NCs was mixed with 0.1-1mL MPA and shaken for 10 minutes, leading to partial flocculation. To this, 1mL basic water (0.4g NaOH in 50mL water) was added and was again shaken vigorously. It was then centrifuged and led to a clear, colored polar phase. This was cleaned by two cycles of precipitation with 4mL acetone, centrifugation and re-dispersion in 1mL deionized water.

Nanocrystal and Materials Properties Characterization. The optical properties of materials were determined by absorption (Cary 5000 UV-Vis-NIR spectrophotometer) and steady-state and time-resolved photoluminescence spectroscopy (Horiba FL1057) of dilute solutions (1mg/mL). Different thicknesses, determined by sample cross section (scanning electron microscopy, FEI SEM FEG Inspect) of CIS were deposited on FTO and the absorption (Cary 5000 UV-Vis-NIR spectrophotometer) was taken to get the absorption coefficient. Photoluminescence transients of TiO_2 and adsorbed CIS nanocrystals were measured (Horiba FL1057) using a 636nm laser excitation. The TiO_2 film was immersed in a 1M methanol solution of the diacids for 2 days and rinsed with methanol before the adsorption of CIS. The photoluminescence of ligand-exchanged films and those in contact with TiO_2 is small. We measured the emission of ligand-exchanged CIS of various layers on different TiO_2 substrates by micro-Raman spectroscopy (Renishaw InVia), exciting the sample with a 785nm laser and probing the high Raman shift regions which corresponded to the luminescence range of the material.

Structural properties were elucidated by powder X-ray diffraction from a table top source (PANalytical X'Pert PRO) or from a synchrotron source (ALBA, Spain), by Raman spectroscopy (Renishaw InVia) of drop-casted films and by high-resolution transmission electron microscopy (JEOL JEM 2011) of dilute solutions deposited on carbon-coated Cu grids (Ted Pella Inc).

A chemical description of the material was obtained by combining information from the chemical composition of CISZn-OA of various sizes through energy-dispersive x-ray spectroscopy (FEI SEM FEG Inspect), the oxidation states of constituent elements through x-ray photoelectron spectroscopy (ICN2, Spain) analyzed using XPSPeak and the signatures of organic groups at various stages of material processing through Fourier transform infrared spectroscopy (Agilent Cary 600 series).

The Fermi level and band edge positions of ligand-exchanged films and of annealed TiO_2 were determined using ultra-violet photoelectron spectroscopy (SPECS PHOIBOS 150 electron spectrometer HeI, 21.2 eV. ICN2, Spain).

The changes in film porosity was analysed through Brunauer-Emmett-Teller adsorption (TriStar 3000, CCiT-UB). Large quantities of densified TiO_2

substrates based on 90T and its modification were fabricated and carefully scraped to form a powder. Samples were heated to 450°C for at least 3 hours prior to the measurement to remove adsorbed moisture. The pore size distribution was obtained by performing Barrett-Joyner-Halenda analyses on the adsorption isotherm.

To determine the extent of CIS infiltration into TiO_2, the depth profile of devices without contacts was analyzed using time-of-flight secondary ion mass spectrometry (Ion TOF IV, IBEC, Spain) under positive polarity, probing key elements in each layer (CIS, In; TiO_2, Ti; SnO_2:F, Sn; SiO_2, Si).

Device fabrication and characterization. Field effect transistors (FETs) were fabricated by depositing 30nm of the material via the LbL process onto 285 nm thermally-grown silica on p-doped silicon. The 50nm gold source and drain contacts were thermally-evaporated (Kurt J Lesker Nano 36) through masks with 1 mm channel widths and 30 µm channel lengths (Ossila evaporation mask). The gate was contacted by scratching the silica layer to reach the p-doped silicon. Individual transistors were isolated from neighboring transistors by scratching away the deposited material. Mobility and majority carrier type of the NC solid were determined from the transfer characteristics (Agilent B1500A) of the FETs.

Photoconductive photodetectors were made by depositing 60nm of the material onto interdigitated gold electrodes. The photodetector was illuminated by a pulsing 635nm laser light of various intensities 15-520µW/cm^2 (Thorlabs 4-Channel Fiber-Coupled Laser Source, Kiethley 3390 function generator) and the transient rise and decay was recorded (Agilent B1500A).

For solar cells, TiO_2 films were rinsed with methanol and toluene before the deposition of CIS. A solution of 25mg/mL CIS in toluene was allowed to settle on the surface of the TiO_2 electrode for 30s, and afterwards was spun at 2000RPM for 30s. Whilst spinning, a drop of 2%vol formic acid in methanol was reacted on the film and finally was rinsed with methanol and toluene. This cycle constitutes one layer of the layer-by-layer (LbL) deposition process. Multiple layers were deposited, starting from 6 layers up until 18 layers. Optionally, spiro-OMeTAD solutions were spincoated (2000RPM, 30s) on top of the final layer as a way of preventing shorts. All devices were fabricated in air.

Top electrodes of 75nm Au and 100nm Ag were consecutively thermally evaporated (Kurt J Lesker Nano 36) through masks with 2mm diameter holes.

The current voltage characteristics of completed devices in the dark and under simulated sunlight (100 mW cm^{-2} AM1.5G, Oriel Sol3A) were recorded using a Keithley 2400 sourcemeter controlled by in-house developed LabView programs. The spectrally-resolved external quantum efficiency was obtained by measuring the short circuit current of devices illuminated with monochromatic light (Newport Oriel apex) of known intensity (Newport 818-UV photodiode). Capacitance-voltage profiling of solar cells was performed on an Agilent B1500A semiconductor parameter analyser.

Transient photovoltage (TPV) and photocurrent (TPC) of the devices were measured with an in-house-built set-up, comprised of a xenon arc lamp, a 637-nm laser (Vortran Stradus) and an Agilent 4000X oscilloscope. The white lamp provided for the steady open circuit voltage (V_{OC}) of the device, whose intensity was controlled by an external applied voltage and was attenuated with a metal-mesh when needed. The laser with a frequency of 10 Hz and pulse width of 500 µs was controlled by a function generator; its intensity was controlled to keep the voltage transient amplitude not more than 5% of the steady state light bias. The oscilloscope recorded the data using a 1 MΩ input impedance for the TPV measurement and a 50 Ω input for the TPC measurement. In the same set-up, the intensity-dependent V_{OC} and J_{SC} were measured with a Xenon arc lamp calibrated with Newport 818-UV power meter and an Agilent 4000X oscilloscope. The accuracy of this measurement was estimated to be within ±8%. All electrical characterization of the devices was performed in air.

Supplementary Information for Chapter 2
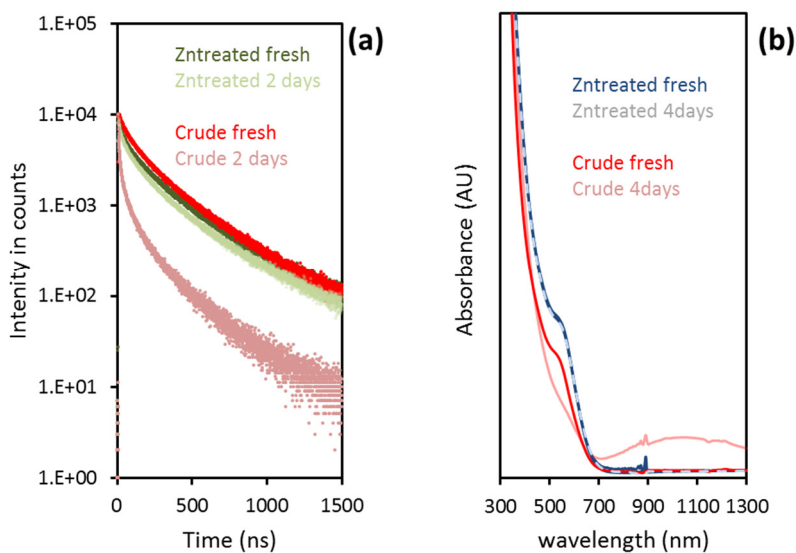
Figure B1 (a-b) Effects of Zn-post-treatment on the optical properties of CIS NCs. (a) Normalized time-resolved PL of crude and treated particles with aging. Zn treatment maintains transient PL properties; unshelled materials have increased short PL lifetime component. (b) UVVis spectra of crude and treated particles with aging: increased free carrier absorption in crude materials.
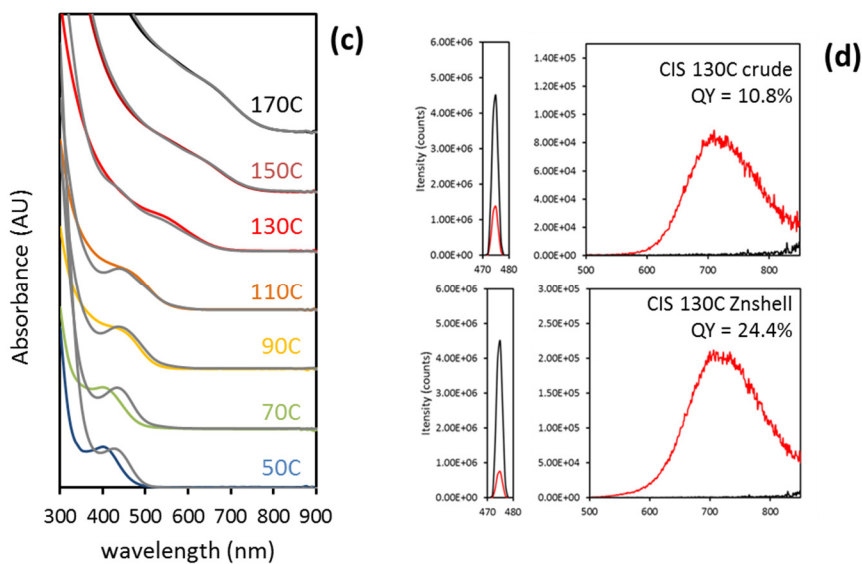
Figure B1 (c-d) Effects of Zn-post-treatment on the optical properties of CIS NCs. (c) Absorption spectra of crude (grey) and treated (colored) NCs. Zn treatment causes a blue-shift, being a more pronounced for smaller particles (c). (d) PLQY of shelled materials is higher.

Table B1. PLQY of different sized QDs using two methods (using the integrating sphere and rhodamine 6G as standard).and measurements days, roughly a year apart.

	shelled			crude	
	Feb092015 integsphere	Feb062015 Rhod6G std	Mar072014 integ sphere	Mar072014 integ sphere	Feb062015 Rhod6G std
CIS 130	17.23	19.7	24.4	10.8	0.7
CIS 110	9.53	9.5			
CIS 90	4.99	5.1	4.9	0.7	0.4
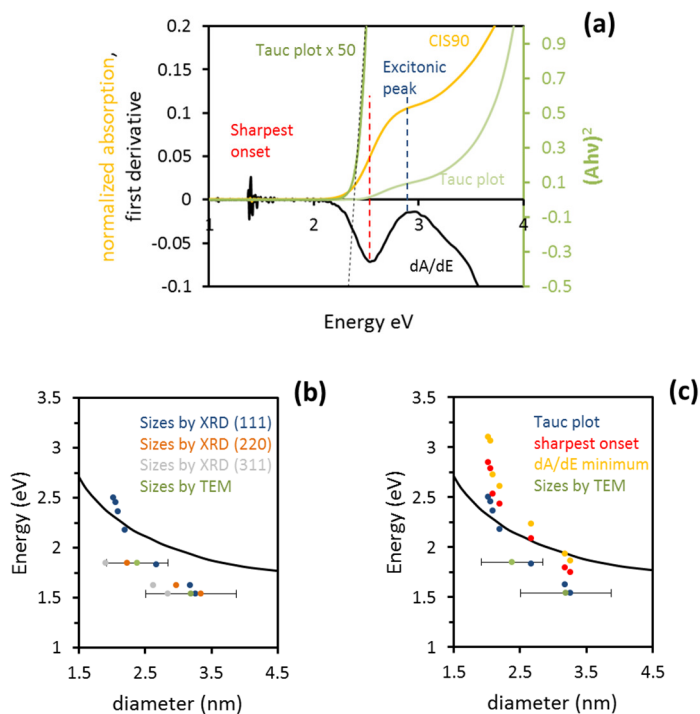
Figure B2 Bandgap calculations and relationships with size. There are three ways (a) to calculate the bandgap from the absorption spectrum, using the Tauc plot (green), the sharpest onset (red) and the excitonic peak (blue). The bandgap calculated from these are overlaid on the absorption spectrum (yellow). As there is no clear excitonic peak, the first derivative will not have a zero value, instead, the first minimum is taken. (b) Sizing by XRD was performed on secondary diffraction peaks which fall in the range of the size dispersion by TEM sizing. The bandgaps for these sizes is taken to from the Tauc plot. (c) Bandgap vs NC size (XRD) comparing different definitions of the bandgap, using the Tauc plot, the sharpest onset and the excitonic peak.
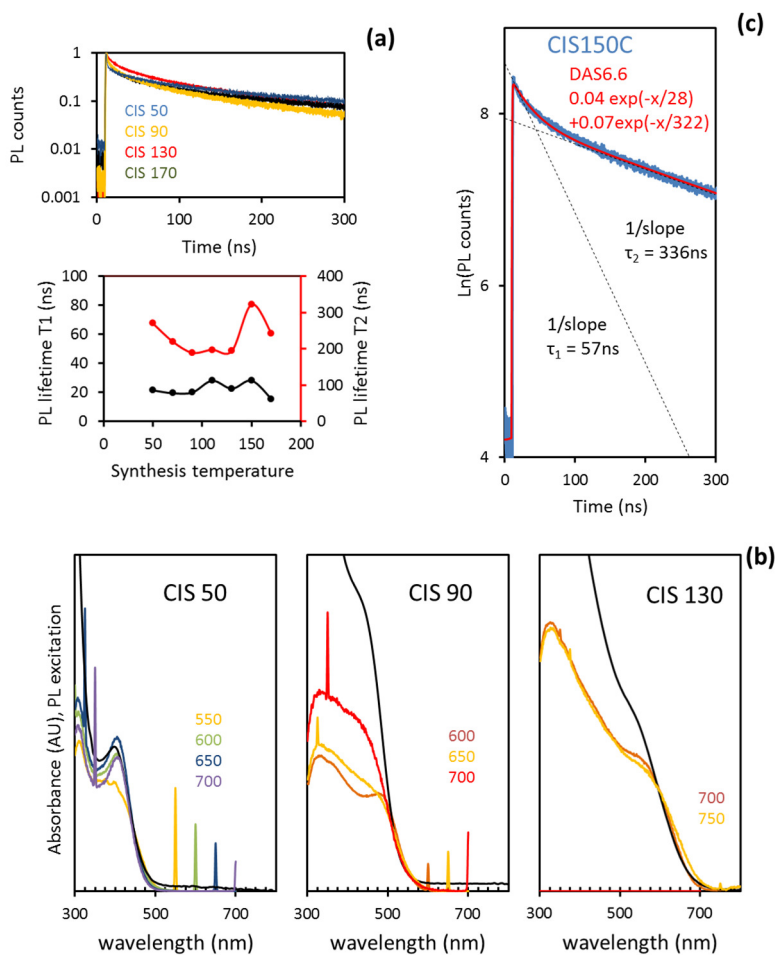
Figure B3 Photoluminescence properties of CIS-ZnOA. (a) Transient photoluminescence curves of CIS synthesized at different temperatures, excited at 475nm and probed at their PL maximum, showing a biexponential decay. (b) Photoluminescence excitation (PLE) spectra of CIS 50, CIS 90, CIS 130 at various probe wavelengths. The absorption onset of the corresponding material is overlaid in black. (c) Measurement of PL lifetime by using a software, DAS6.6 Horiba Jovin Yvon. Other values can be fitted by taking the inverse of the slope of at short and long decay decay times in natural logarithm. These two give comparable results especially for long decay times. The former was used for the calculation of the decay times
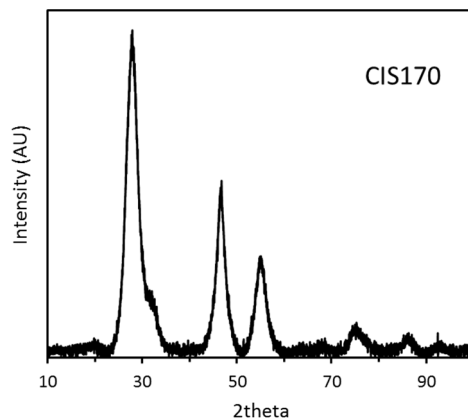
Figure B4 Extended XRD diffractogram of CIS-ZnOA. Extended XRD diffractogram of CIS170 with the absence of the peak between 10-20 2theta (lower than 15 Å^{-1}), which is characteristic of tetragonal CuInS$_2$ (JCPDS 85-1575). This spectrum instead matches the structure of cubic zincblende CuInS$_2$.
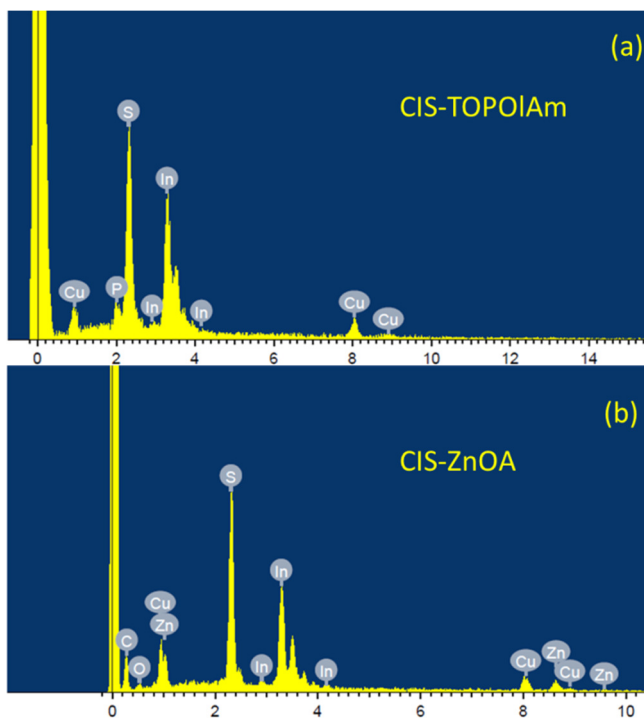
Figure B5 EDX spectra of CIS-OlAmTOP and CIS-ZnOA. (a) EDX spectra of CIS170 showing the presence of phosphorus in CIS-TOPOlAm, and (b) the disappearance of phosphorus and appearance of Zn with the treatment of ZnOA.
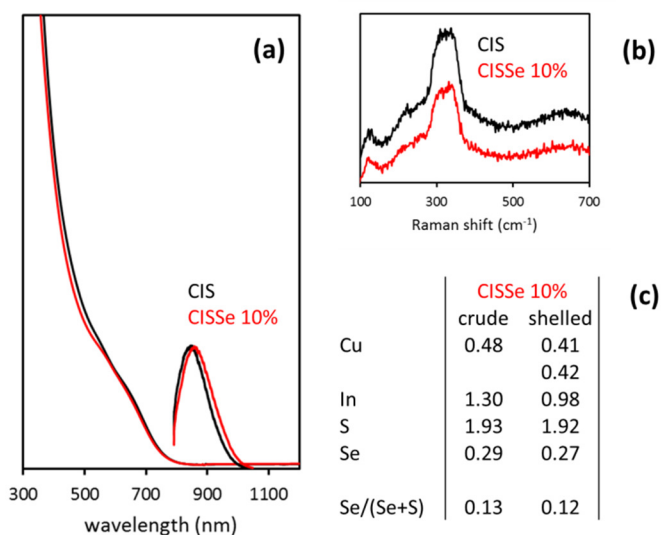
Figure B6 Use of mixtures of TMS₂Se and TMS₂S to form CISₓSe₂₋ₓ. (a) UVVis and photoluminescence spectra of CIS and CISSe at 10% nominal Se molar content. (b) Raman spectra of CIS and CISSe10% showing no formation of binary sulfides. (c) Compositions of CIS and CISSe10% obtained by EDX, showing little change in Se/(Se+S) ratio before and after shelling.
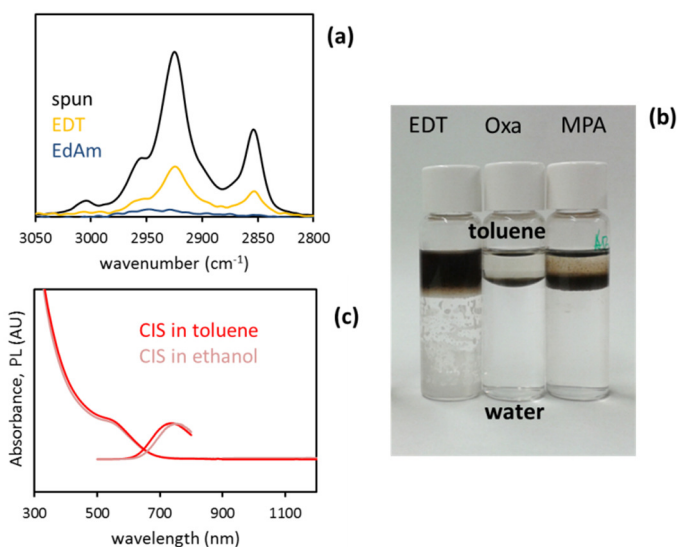
Figure B7 Ligand exchange studies for CIS NCs. (a) FTIR spectra of the C-H stretching for various ligands, EDT and EdAm. (b) In testing which functional group attaches to the NC surface, various bifunctional molecules were used. No flocculation was seen with EDT. (c) These particles are still emissive after phase transfer in a polar solvent.

86

Table B2. Calculation of copper replacement with indium in the crude material and indium replacement with zinc in the treated material using the model described in the text.

CRUDE

	Ideal	Defect	adjusted	crude170	excess	difference	
S	2	2	2.17	2.17		2.17	
Cu	1	0.5	0.5	0.50		0.50	#formulas
Zn							$= Z*NC_{vol}/U_{vol}$
In	1	1.17	1.17	1.34	0.17	1.34	= 205
net	0	0	-0.34	0.17	0.51	0.17	

$2V_{cu}{}'+ In_{Cu}{}^{\bullet\bullet}$

VB+0.10, CB-0.13

50% Cu replaced, "$CuIn_{2.3}S_4$"
60% Cu replaced, "$CuIn_3S_5$"
75% Cu replaced, "$CuIn_5S_8$"

820 atoms,
35 excess Indium
atoms on the surface

SHELLED

	Defect	adjusted	shelled	excess	difference	
S	2	2.12	2.12		2.12	depthZn penetration
Cu	0.48	0.48	0.48		0.48	= rNC- rcore
Zn	0.31	0.31	0.43	0.12	0.43	$= 1.6-r(V_{NC}-\%Zn*V_{NC})$
In	0.98	0.98	0.98		0.98	= 0.11nm
net	0	-0.22	0.03	0.25	0.03	

Cu^{1+} = 91 pm
In^{3+} = 94 pm   19.5% of In replaced
Zn^{2+} = 88 pm

r_{unit} = 0.08 nm
30 excess Zn
atoms on the surface

The column in red is the EDX data for CIS 170 crude and the treated one. The top panel shows the calculation for the crude material and the bottom one for the treated one.

For the crude: the calculation starts off with the ideal 2:1:0:1 stoichiometry for S:Cu:Zn:In, leading to a net zero charge. Next, maintaining the charge neutrality, we look for the amount of copper which will match the EDX data leading to Cu at 0.5 and In at 1.15. The amount of sulfur is matched with EDX data. With the size of the nanocrystal known, we can calculate the number of CIS formulas. This gives us a rough approximation of the number of indium atoms on the surface. For the treated materials: Following the model that mostly indium gets replaced with Zn, as suggested that the surface is more indium rich, we look for the percent of In that matches the EDX data maintaining charge neutrality, leading to 19.5% replacement. The same calculation can be done for CIS130 and CIS90.

Supplementary Information for Chapter 3
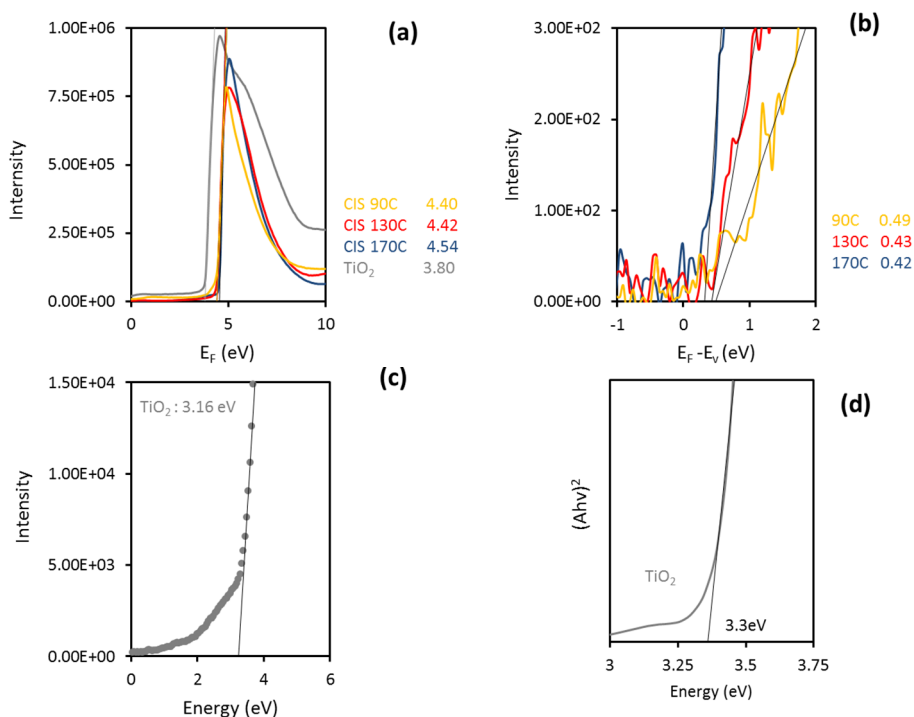
Figure C1. The UPS spectra (excitation of 21.21eV) of CIS and TiO$_2$. (a) The UPS spectra (excitation of 21.21eV) of CIS and TiO$_2$ used for the calculation of the Fermi level showing the cut-off region of samples biased at -5V and (b, c) the valence band onset. (d) Tauc plot of nanocrystalline TiO$_2$ film (90T, 500nm).

The Fermi level was obtained by extrapolating the x-intercept of the sharp cut-off region in biased samples (-10V and -5V) excited by 21.21eV (HeI). The Fermi level was calculated by

$$E_F = E_{intercept} - 21.21 - V_{bias}.$$

The average of the results from the two bias-voltages was taken. The valence band edge was calculated by taking the onset in unbiased samples and subtracting this from the obtained E_F. The conduction band edge was obtained by adding the bandgap calculated from the Tauc plot onset to the valence band edge.
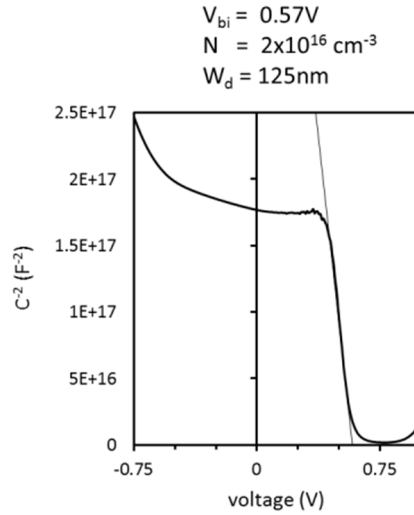
Figure C2. 1/C² vs voltage plot of CIS-flat TiO₂ devices. Values for the V_{bi}, N and W_d were calculated using Mott-Schottky analysis.

The carrier concentration, N, was calculated using the Mott Schottky equation:

$$N = -\frac{2}{q\varepsilon_r\varepsilon_o A^2}\left(\frac{dC^{-2}}{dV}\right)^{-1}$$

where q is the elementary charge (1.602×10^{-19} C), ε_o is the permitivitty of free space (8.54×10^{-12} C V^{-1} m^{-1}), ε_r is the relative permitivitty (5.5^{185}), A is the device area (3.14×10^{-6} m²) and d(C^{-2})/dV is the slope of the linear region shown in Figure C2. The V_{bi} is taken from the x-intercept of this extrapolation. We find that N = 2×10^{16} cm^{-3} and V_{bi} = 0.57 V.

90

With N and V_{bi}, we can calculate the depletion width W using:

$$W = \sqrt{\frac{2\varepsilon_r \varepsilon_o V_{bi}}{qN}}$$

We calculated a depletion width of 125nm at $V_{applied} = 0$.

Table C1. Device performance of various sizes of CIS, thicknesses and Zn content on flat-TiO2 (90T).

CIS	Zn	layers	V_{oc}	J_{sc}	FF
90°C 1.0		6	0.50±0.02	0.011±0.005	0.29±0.02
130°C 1.0		6	0.55±0.03	0.077±0.02	0.25±0.02
170°C 1.0		**6**	0.59±0.05	0.91±0.19	0.27±0.03
170°C 1.0		**12**	0.60±0.04	0.93±0.12	0.32±0.04
170°C 1.0		**18**	0.61±0.01	1.08±0.08	0.33±0.01
170°C 0.3		**6**	0.63±0.04	1.26±0.36	0.31±0.09
170°C 0.3		**12**	0.62±0.05	1.39±0.27	0.30±0.06
170°C **0.3**		**18**	0.60±0.01	1.67±0.06	0.33±0.01
170°C **0.1**		6	0.63±0.01	1.81±0.55	0.26±0.01

CIS	Zn	layers	PCE	R_s (kΩ)	R_{sh} (kΩ)
90°C 1.0		6	0.002±0.0005	30.29±2.56	2259.5±477
130°C 1.0		6	0.011±0.003	24.20±3.39	225.8±10.88
170°C 1.0		**6**	0.15±0.04	1.72±0.54	25.65±13.5
170°C 1.0		**12**	0.19±0.02	1.41±0.244	35.33±13.9
170°C 1.0		**18**	0.22±0.01	1.08±0.04	25.97±2.17
170°C 0.3		**6**	0.23±0.05	1.53±0.72	18.16±86.5
170°C 0.3		**12**	0.29±0.09	1.35±0.67	24.42±6.79
170°C **0.3**		**18**	0.33±0.02	0.514±0.07	18.91±0.38
170°C **0.1**		6	0.30±0.09	1.74±0.64	22.3±7.29

Supplementary Information for Chapter 4
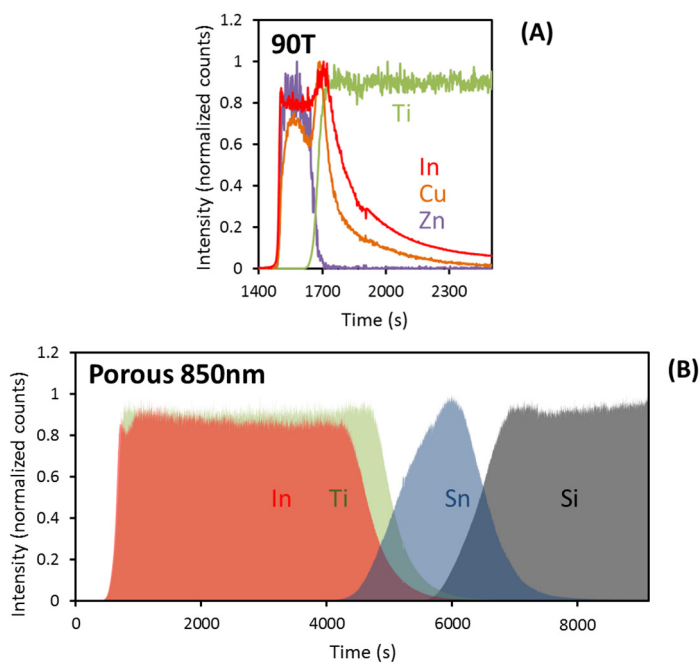
Figure D1. Additional SIMS spectra of CIS-infiltrated TiO$_2$. (a) Secondary ion mass spectra of CIS on flat TiO$_2$ focusing on the first few moments of ion bombardment showing the differences in ionization probabilities as metal ratios are different from that obtained from EDX. The x-axis has been retained on the time scale as each layer will have different sputter rates. (b) Infiltration of 6 layers of CIS in porous-TiO2 (850nm) is deep. At 6 layers, no overlayer is formed.

Table D1. IV characteristics of CIS 0.3 Zn in flat and porous TiO$_2$ under full sun and 400nm-filtered light.

TiO$_2$	CIS	layers	filter	Voc	Jsc	FF	PCE
flat	CIS 0.3 Zn	6L		0.64	1.15	0.23	0.17
flat	CIS 0.3 Zn	6L	UV	0.65	0.44	0.28	0.08
p-500	CIS 0.3 Zn	6L		0.65	2.74	0.52	0.94
p-500	CIS 0.3 Zn	6L	UV	0.65	2.43	0.55	0.87

	Voc	Jsc	FF	η
CIS6L-BL no spiro	0.56	0.87	0.35	0.17
CIS6L-90T no spiro	0.56	1.1	0.29	0.18
CIS6L-90T w/ spiro	0.59 ± 0.05	0.91 ± 0.19	0.27±0.03	0.15±0.04

CIS6L blocking TiO$_2$	CIS6L Flat TiO$_2$	CIS6L Porous TiO$_2$
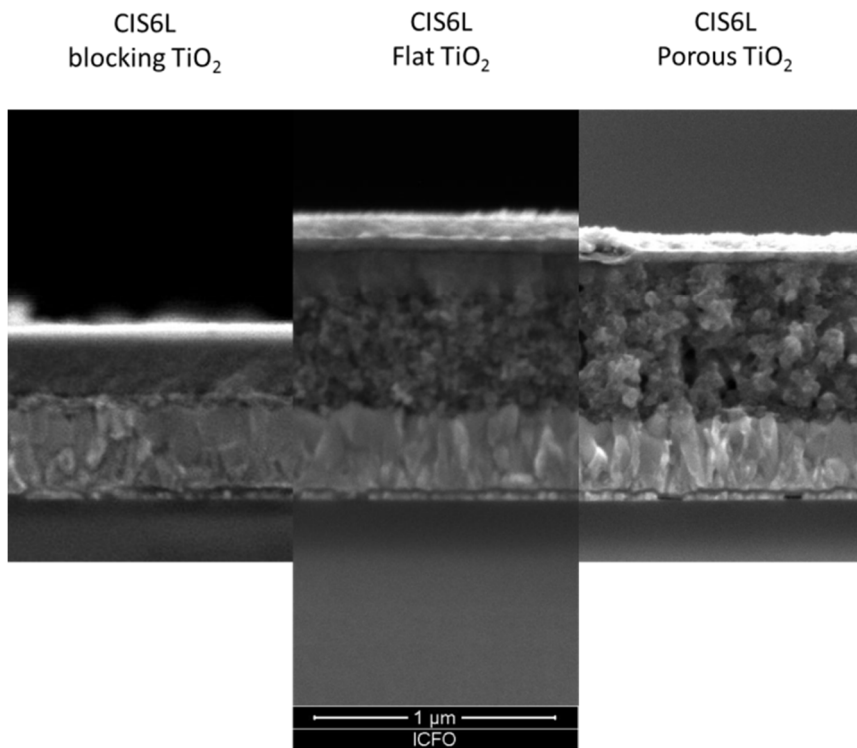
Figure D2. The effect of Spiro-MeO-TAD. (Top) IV characteristics of devices made from CIS 1.0 Zn on TiO$_2$ blocking layer without a Spiro spacer, from CIS 1.0 Zn on 90T without a Spiro spacer and from CIS 1.0 Zn on 90T with a Spiro spacer have similar performance. (Bottom) Cross-sectional SEM images of CIS devices without Spiro.

Table D2. Device performance of CIS with different Zn content on various TiO$_2$ substrates (f-TiO$_2$, flat TiO$_2$; p-xxx, porous TiO$_2$ xxx nm thick).

Zn	layers	TiO$_2$	V_{oc}	J_{sc}	FF
1.0	6	f-TiO$_2$	0.59±0.05	0.91±0.19	0.27±0.03
1.0	6	p-500	0.60±0.03	2.18±0.46	0.50±0.06
0.33	6	f-TiO$_2$	0.63±0.04	1.26±0.36	0.31±0.09
0.33	6	p-500	0.65±0.02	2.66±0.09	0.52±0.03
0.33	12	p-850	0.67±0.02	3.83±0.52	0.39±0.01
0.1	6	f-TiO$_2$	0.63±0.01	1.81±0.55	0.26±0.01
0.1	6	p-500	0.67±0.03	1.82±0.53	0.36±0.03

Zn	layers	TiO$_2$	PCE	R_s	R_{sh}
1.0	6	f-TiO$_2$	0.15±0.04	1.72±0.54	25.65±13.5
1.0	6	p-500	0.65±0.18	0.31±0.14	41.53±18.9
0.33	6	f-TiO$_2$	0.23±0.05	1.53±0.72	18.16±86.5
0.33	6	p-500	0.87±0.07	0.43±0.16	35.51±8.9
0.33	12	p-850	1.01±0.15	0.98±0.07	13.14±1.39
0.1	6	f-TiO$_2$	0.30±0.09	1.74±0.64	22.3±7.29
0.1	6	p-500	0.44±0.13	2.97±0.68	22.5±7.40
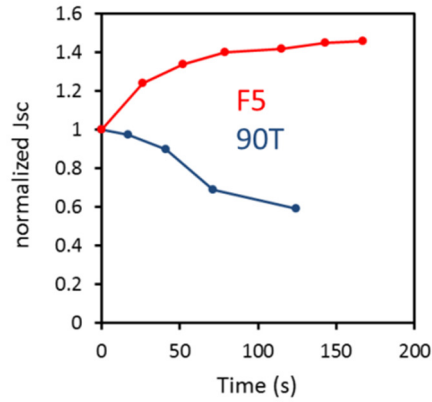
Figure D3. Performance of BHJ and bilayer devices under illumination. The normalized J_{sc} with time under light shows that the J_{sc} of BHJ devices reach a saturation point after a minute while that of bilayer devices decreases with time. Comparisons in device performance are always reported at time $t = 0$.
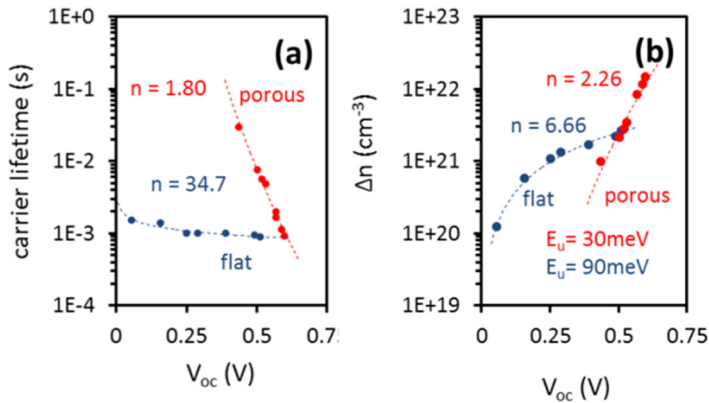
Figure D4. Urbach energy and ideality factors from carrier liteime, Δn and V_{oc}. (a) Carrier lifetime and (b) excess charge carrier density vs V_{oc} of flat and porous devices have completely different behavior. Calculated Urbach energies are shown.
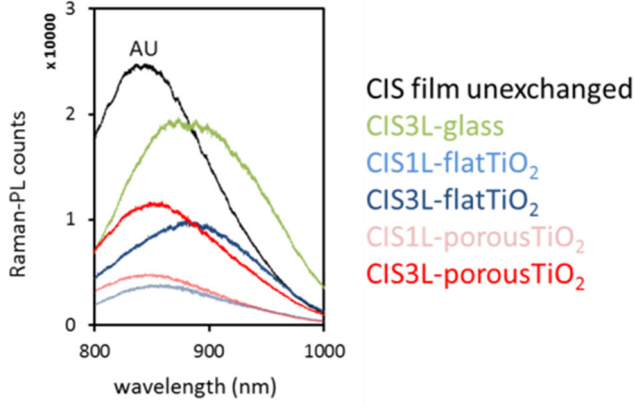
Figure D5. Raman PL of CIS devices. Raman-photoluminescence spectra of CIS films, untreated and treated, on glass, flat TiO$_2$ and porous TiO$_2$ showing a decrease in PL when placed with TiO$_2$.

Calculation of recombination rate:

The recombination rate R was calculated with the relation:

$$R = \frac{\Delta n}{\tau}$$

where Δn is the excess carrier concentration calculated from the transient techniques and τ is the recombination decay time calculated from fitting TPV curve using the relation:

$$\Delta V_{OC}(t) = \sum_{k=1}^{x} A_k \left\{ \exp\left(\frac{-t}{\tau_k}\right) \right\}$$

where A_k is a weighting parameter. For flat devices we find that $x = 2$ and for porous devices, $x = 1$. We took the lifetime as the short time scales of the decay curve.

The generalised recombination rate (R) is related to the excess carrier concentration (Δn) with the following equation,

$$R \propto K_1(\Delta n) + K_2(\Delta n)^2 + K_3(\Delta n)^3$$

97

where K_1, K_2 and K_3 stand for the recombination rate constant for the trap induced (first order b=1), radiative (second order b=2) and Auger recombination (third order b=3) respectively.

Urbach tail energy relation is taken from Foertig et al[181]:
The exponential distribution of the trap states is given as,

$$N(E) = N_0 \exp\left(\frac{-|E-E_B|}{E_U}\right)$$

where N_0 is the effective density of states, E_B is the band edge and EU is the Urbach tail energy.

It can be calculated using Shockley equation ideality factor (n_n) for charge carrier density given by,

$$n = n_0 \exp\left(\frac{qV_{OC}}{\eta_n kT}\right)$$

The relation between E_U and n_n is given by,

$$E_U = \frac{n_n kT}{2}$$

The ideality factors are related with the equation,

$$\frac{1}{n_R} = \frac{1}{n_n} + \frac{1}{n_\tau}$$

where n_τ is given by the equation,

$$\tau = \tau_0 \exp\left(\frac{-qV_{OC}}{\eta_\tau kT}\right)$$

and $n_R \approx n_{id.}$

The recombination order $\lambda+1$ is defined by

98

$$\lambda + 1 = \frac{1 n_n}{n_\tau} + 1$$

These values are summarized in Table S4.

The V_{OC} decay curves were fitted with exponential decay to find the recombination time. The TPC curve was integrated to get the charge generated (ΔQ) in the devices due to the laser pulse. The capacitance (C) was calculated from the C= $\Delta Q/\Delta V_{OC}$ relation. The total charge carrier was calculated from the integration of C vs V_{OC} plot. Charge carrier density was calculated by dividing the total charge carriers with the device volume.

Table D3. Comparison of various ideality factors, power law exponents and Urbach energy calculations for flat and porous devices.

	flat	porous
n_τ	34.7	1.8
n_n	6.7	2.3
$\lambda+1$	1.2	2.3
n_R	5.6	1.0
b	1.2	2.2
n_{id}	2.1 to 3.8	1 to 1.5
$E_{U, EQE}$	141	80
$E_{U, nn}$	83.4	28.2

100

BIBLIOGRAPHY

(1)   Owen, N. A.; Inderwildi, O. R.; King, D. A. The Status of Conventional World Oil reserves—Hype or Cause for Concern? *Energy Policy*, **2010**, *38*, 4743–4749.

(2)   *World Energy Statistics and Balances*; Agency, (IEA) International Energy, Paris: OECD/IEA, **2014**.

(3)   REN21. **2015**. *Renewables 2015 Global Status Report*.

(4)   Hermann, W. A. Quantifying Global Exergy Resources. *Energy* **2006**, *31*, 1685–1702.

(5)   Lewis, N. S.; Crabtree, G. Basic Research Needs for Solar Energy Utilization: Report of the Basic Energy Sciences Workshop on Solar Energy Utilization, April 18-21, 2005. **2005**.

(6)   Luque, A. (Antonio); Hegedus, S. *Handbook of Photovoltaic Science and Engineering*; Wiley, **2011**.

(7)   Atwater, H. A.; Polman, A. Plasmonics for Improved Photovoltaic Devices. *Nat. Mater.* **2010**, *9*, 865–865.

(8)   Centers for Disease Control and Prevention. Immediately Dangerous to Life or Health Concentrations http://www.cdc.gov/niosh/idlh/intridl4.html. Accessed April 15, 2016.

(9)   EUR-Lex - 32002L0095 - EN. *Off. J. L 037 , 13/02/2003 P. 0019 - 0023;*

.

(10)   Becquerel, E. Comptes Rendus Hebdomadaires Des Séances de l'Académie Des Sciences / Publiés... Par MM. Les Secrétaires Perpétuels. **1839**.

(11)   Chapin, D. M.; Fuller, C. S.; Pearson, G. L. A New Silicon P-N Junction Photocell for Converting Solar Radiation into Electrical Power. *J. Appl. Phys.* **1954**, *25*, 676.

(12)   NREL. Best Research Cell Efficiencies. http://www.nrel.gov/ncpv/ Accessed June 10, 2016.

(13)   Green, M. A.; Emery, K.; Hishikawa, Y.; Warta, W.; Dunlop, E. D. Solar Cell Efficiency Tables (Version 47). *Prog. Photovoltaics Res. Appl.* **2016**, *24*, 3–11.

(14)   Philipps, S.; Warmuth, W. *Photovoltaics Report*; **2016**.

(15)   Nelson, J. *The Physics of Solar Cells*; Imperial College Press World scientific Publishing Co., **2003**.

(16)   Pearson, G. L.; Bardeen, J. Electrical Properties of Pure Silicon and Silicon Alloys Containing Boron and Phosphorus. *Phys. Rev.* **1949**, *75*, 865–883.

(17)   Green, M. A.; Keevers, M. J. Optical Properties of Intrinsic Silicon at 300 K. *Prog. Photovoltaics Res. Appl.* **1995**, *3*, 189–192.

(18)   Chopra, K. L.; Paulson, P. D.; Dutta, V. Thin-Film Solar Cells: An Overview. *Prog. Photovoltaics Res. Appl.* **2004**, *12*, 69–92.

(19)   Han, S.-H.; Hermann, A. M.; Hasoon, F. S.; Al-Thani, H. A.; Levi, D. H. Effect of Cu Deficiency on the Optical Properties and Electronic Structure of $CuInSe_2$ and $CuIn_{0.8}Ga_{0.2}Se_2$ Determined by Spectroscopic Ellipsometry. *Appl. Phys. Lett.* **2004**, *85*, 576.

(20)   Ullal, H. S. Polycrystalline Thin-Film Solar Cell Technologies: Preprint. **2009**.

(21)   Hariskos, D.; Spiering, S.; Powalla, M. Buffer Layers in $Cu(In,Ga)Se_2$ Solar Cells and Modules. *Thin Solid Films* **2005**, *480*, 99–109.

(22)   Lu, L.; Zheng, T.; Wu, Q.; Schneider, A. M.; Zhao, D.; Yu, L. Recent Advances in Bulk Heterojunction Polymer Solar Cells. *Chem. Rev.* **2015**, *115*, 12666–12731.

(23)   Brabec, C. J.; Gowrisanker, S.; Halls, J. J. M.; Laird, D.; Jia, S.; Williams, S. P. Polymer-Fullerene Bulk-Heterojunction Solar Cells. *Adv. Mater.* **2010**, *22*, 3839–3856.

(24)   Yu, G.; Gao, J.; Hummelen, J. C.; Wudl, F.; Heeger, A. J. Polymer Photovoltaic Cells: Enhanced Efficiencies via a Network of Internal Donor-Acceptor Heterojunctions. *Science (80-.).* **1995**, *270*.

(25)   Blom, P. W. M.; Mihailetchi, V. D.; Koster, L. J. A.; Markov, D. E. Device Physics of Polymer:Fullerene Bulk Heterojunction Solar Cells. *Adv. Mater.* **2007**, *19*, 1551–1566.

(26)   Bundgaard, E.; Hagemann, O.; Manceau, M.; Jørgensen, M.; Krebs, F. C. Low Band Gap Polymers for Roll-to-Roll Coated Polymer Solar Cells. *Macromolecules* **2010**, *43*, 8115–8120.

(27)   Krebs, F. C. *Stability and Degradation of Organic and Polymer Solar Cells*; Wiley, **2012**.

(28)   Hagfeldt, A.; Boschloo, G.; Sun, L.; Kloo, L.; Pettersson, H. Dye-Sensitized Solar Cells. *Chem. Rev.* **2010**, *110*, 6595–6663.

(29)   Grätzel, M. Dye-Sensitized Solar Cells. *J. Photochem. Photobiol. C Photochem. Rev.* **2003**, *4*, 145–153.

(30)   O'Regan, B.; Grätzel, M. A Low-Cost, High-Efficiency Solar Cell Based on Dye-Sensitized Colloidal TiO2 Films. *Nature* **1991**, *353*, 737–740.

(31)   Park, N.-G. Perovskite Solar Cells: An Emerging Photovoltaic Technology. *Mater. Today* **2015**, *18*, 65–72.

(32)   Jung, H. S.; Park, N.-G. Perovskite Solar Cells: From Materials to Devices. *Small* **2015**, *11*, 10–25.

(33)   Kojima, A.; Teshima, K.; Shirai, Y.; Miyasaka, T. Organometal Halide Perovskites as Visible-Light Sensitizers for Photovoltaic Cells. *J. Am. Chem. Soc.* **2009**, *131*, 6050–6051.

(34) Eperon, G. E.; Burlakov, V. M.; Docampo, P.; Goriely, A.; Snaith, H. J. Morphological Control for High Performance, Solution-Processed Planar Heterojunction Perovskite Solar Cells. *Adv. Funct. Mater.* **2014**, *24*, 151–157.

(35) Stranks, S. D.; Eperon, G. E.; Grancini, G.; Menelaou, C.; Alcocer, M. J. P.; Leijtens, T.; Herz, L. M.; Petrozza, A.; Snaith, H. J. Electron-Hole Diffusion Lengths Exceeding 1 Micrometer in an Organometal Trihalide Perovskite Absorber. *Science* **2013**, *342*, 341–344.

(36) Miyata, A.; Mitioglu, A.; Plochocka, P.; Portugall, O.; Wang, J. T.-W.; Stranks, S. D.; Snaith, H. J.; Nicholas, R. J. Direct Measurement of the Exciton Binding Energy and Effective Masses for Charge Carriers in Organic–inorganic Tri-Halide Perovskites. *Nat. Phys.* **2015**, *11*, 582–587.

(37) Leijtens, T.; Eperon, G. E.; Pathak, S.; Abate, A.; Lee, M. M.; Snaith, H. J. Overcoming Ultraviolet Light Instability of Sensitized TiO2 with Meso-Superstructured Organometal Tri-Halide Perovskite Solar Cells. *Nat. Commun.* **2013**, *4*.

(38) Noel, N. K.; Stranks, S. D.; Abate, A.; Wehrenfennig, C.; Guarnera, S.; Haghighirad, A.-A.; Sadhanala, A.; Eperon, G. E.; Pathak, S. K.; Johnston, M. B.; *et al.* Lead-Free Organic–inorganic Tin Halide Perovskites for Photovoltaic Applications. *Energy Environ. Sci.* **2014**, *7*, 3061.

(39) Hao, F.; Stoumpos, C. C.; Cao, D. H.; Chang, R. P. H.; Kanatzidis, M. G. Lead-Free Solid-State Organic–inorganic Halide Perovskite Solar Cells. *Nat. Photonics* **2014**, *8*, 489–494.

(40) Singh, S.; Ryan, K. M. Occurrence of Polytypism in Compound Colloidal Metal Chalcogenide Nanocrystals, Opportunities, and Challenges. *J. Phys. Chem. Lett.* **2015**, *6*, 3141–3148.

(41) Burda, C.; Chen, X.; Narayanan, R.; El-Sayed, M. A. Chemistry and Properties of Nanocrystals of Different Shapes. *Chem. Rev.* **2005**, *105*, 1025–1102.

(42) Talapin, D. V.; Lee, J.-S.; Kovalenko, M. V.; Shevchenko, E. V. Prospects of Colloidal Nanocrystals for Electronic and Optoelectronic Applications. *Chem. Rev.* **2010**, *110*, 389–458.

(43) Rivest, J. B.; Jain, P. K. Cation Exchange on the Nanoscale: An Emerging Technique for New Material Synthesis, Device Fabrication, and Chemical Sensing. *Chem. Soc. Rev.* **2013**, *42*, 89–96.

(44) Beberwyck, B. J.; Surendranath, Y.; Alivisatos, A. P. Cation Exchange: A Versatile Tool for Nanomaterials Synthesis. *J. Phys. Chem. C* **2013**, *117*, 19759–19770.

(45) De Trizio, L.; Manna, L. Forging Colloidal Nanostructures via Cation Exchange Reactions. *Chem. Rev.* **2016**, acs.chemrev.5b00739.

(46) Stavrinadis, A.; Konstantatos, G. Strategies for the Controlled Electronic Doping of Colloidal Quantum Dot Solids. *ChemPhysChem* **2016**, *17*, 632–644.

(47) Yin, Y.; Alivisatos, A. P. Colloidal Nanocrystal Synthesis and the Organic–inorganic Interface. *Nature* **2005**, *437*, 664–670.

(48) Kwon, S. G.; Hyeon, T. Formation Mechanisms of Uniform Nanocrystals via Hot-Injection and Heat-Up Methods. *Small* **2011**, *7*, 2685–2702.

(49) Angshuman Nag, Maksym V. Kovalenko, Jong-Soo Lee, Wenyong Liu, Boris Spokoyny, and D. V. T. Metal-Free Inorganic Ligands for Colloidal Nanocrystals: S^{2-}, HS^-, Se^{2-}, HSe^-, Te^{2-}, HTe^-, TeS_3^{2-}, OH^-, and NH^{2-} as Surface Ligands. *J. Am. Chem. Soc.* **2011**, *133*, 10612–10620.

(50) Murray, C. B.; Norris, D. J.; Bawendi, M. G. Synthesis and Characterization of Nearly Monodisperse CdE (E = Sulfur, Selenium, Tellurium) Semiconductor Nanocrystallites. *J. Am. Chem. Soc.* **1993**, *115*, 8706–8715.

(51) Brown, P. R.; Kim, D.; Lunt, R. R.; Zhao, N.; Bawendi, M. G.; Grossman, J. C.; Bulovic, V. Energy Level Modification in Lead Sulfide Quantum Dot Thin Films through Ligand Exchange. *ACS Nano* **2014**, *8*, 5863–5872.

(52) Ip, A. H.; Thon, S. M.; Hoogland, S.; Voznyy, O.; Zhitomirsky, D.; Debnath, R.; Levina, L.; Rollny, L. R.; Carey, G. H.; Fischer, A.; *et al.* Hybrid Passivated Colloidal Quantum Dot Solids. *Nat. Nanotechnol.* **2012**, *7*, 577–582.

(53)   Jeong, K. S.; Tang, J.; Liu, H.; Kim, J.; Schaefer, A. W.; Kemp, K.; Levina, L.; Wang, X.; Hoogland, S.; Debnath, R.; *et al.* Enhanced Mobility-Lifetime Products in PbS Colloidal Quantum Dot Photovoltaics. *ACS Nano* **2012**, *6*, 89–99.

(54)   Beard, M. C.; Luther, J. M.; Semonin, O. E.; Nozik, A. J. Third Generation Photovoltaics Based on Multiple Exciton Generation in Quantum Confined Semiconductors. *Acc. Chem. Res.* **2013**, *46*, 1252–1260.

(55)   Kairdolf, B. A.; Smith, A. M.; Stokes, T. H.; Wang, M. D.; Young, A. N.; Nie, S. Semiconductor Quantum Dots for Bioimaging and Biodiagnostic Applications. *Annu. Rev. Anal. Chem.* **2013**, *6*, 143–162.

(56)   Wood, V.; Bulović, V. Colloidal Quantum Dot Light-Emitting Devices. *Nano Rev. Exp.* **2010**, *1*.

(57)   Yang, Y.; Zheng, Y.; Cao, W.; Titov, A.; Hyvonen, J.; Manders, J. R.; Xue, J.; Holloway, P. H.; Qian, L. High-Efficiency Light-Emitting Devices Based on Quantum Dots with Tailored Nanostructures. *Nat. Photonics* **2015**, *9*, 259.

(58)   Mora-Seró, I.; Bisquert, J. Breakthroughs in the Development of Semiconductor-Sensitized Solar Cells. *J. Phys. Chem. Lett.* **2010**, *1*, 3046–3052.

(59)   Carey, G. H.; Abdelhady, A. L.; Ning, Z.; Thon, S. M.; Bakr, O. M.; Sargent, E. H. Colloidal Quantum Dot Solar Cells. *Chem. Rev.* **2015**, *115*, 12732–12763.

(60)   Nozik, A. J. Nanoscience and Nanostructures for Photovoltaics and Solar Fuels. *Nano Lett.* **2010**, *10*, 2735–2741.

(61)   Kamat, P. V. Quantum Dot Solar Cells. Semiconductor Nanocrystals as Light Harvesters [†]. *J. Phys. Chem. C* **2008**, *112*, 18737–18753.

(62)   Du, J.; Du, Z.; Hu, J.-S.; Pan, Z.; Shen, Q.; Sun, J.; Long, D.; Dong, H.; Sun, L.; Zhong, X.; *et al.* Zn–Cu–In–Se Quantum Dot Solar Cells with a Certified Power Conversion Efficiency of 11.6%. *J. Am. Chem. Soc.* **2016**, *138*, 4201–4209.

(63)   Pan, Z.; Mora-Seró, I.; Shen, Q.; Zhang, H.; Li, Y.; Zhao, K.; Wang, J.;

Zhong, X.; Bisquert, J. High-Efficiency "Green" Quantum Dot Solar Cells. *J. Am. Chem. Soc.* **2014**, *136*, 9203–9210.

(64)   Hines, M. A.; Scholes, G. D. Colloidal PbS Nanocrystals with Size-Tunable Near-Infrared Emission: Observation of Post-Synthesis Self-Narrowing of the Particle Size Distribution. *Adv. Mater.* **2003**, *15*, 1844–1849.

(65)   Chuang, C.-H. M.; Brown, P. R.; Bulović, V.; Bawendi, M. G. Improved Performance and Stability in Quantum Dot Solar Cells through Band Alignment Engineering. *Nat. Mater.* **2014**, *13*, 1–6.

(66)   Liu, Y.; Gibbs, M.; Puthussery, J.; Gaik, S.; Ihly, R.; Hillhouse, H. W.; Law, M. Dependence of Carrier Mobility on Nanocrystal Size and Ligand Length in Pbse Nanocrystal Solids. *Nano Lett.* **2010**, *10*, 1960–1969.

(67)   Zhang, J.; Tolentino, J.; Smith, E. R.; Zhang, J.; Beard, M. C.; Nozik, A. J.; Law, M.; Johnson, J. C. Carrier Transport in PbS and PbSe QD Films Measured by Photoluminescence Quenching. *J. Phys. Chem. C* **2014**, *118*, 16228–16235.

(68)   Zarghami, M. H.; Liu, Y.; Gibbs, M.; Gebremichael, E.; Webster, C.; Law, M. P-Type PbSe and PbS Quantum Dot Solids Prepared with Short-Chain Acids and Diacids. *ACS Nano* **2010**, *4*, 2475–2485.

(69)   Tang, J.; Kemp, K. W.; Hoogland, S.; Jeong, K. S.; Liu, H.; Levina, L.; Furukawa, M.; Wang, X.; Debnath, R.; Cha, D.; *et al.* Colloidal-Quantum-Dot Photovoltaics Using Atomic-Ligand Passivation. *Nat. Mater.* **2011**, *10*, 765–771.

(70)   Lhuillier, E.; Scarafagio, M.; Hease, P.; Nadal, B.; Aubin, H.; Xu, X. Z.; Lequeux, N.; Patriarche, G.; Ithurria, S.; Dubertret, B. Infrared Photodetection Based on Colloidal Quantum-Dot Films with High Mobility and Optical Absorption up to THz. *Nano Lett.* **2016**, *16*, 1282–1286.

(71)   Zhitomirsky, D.; Voznyy, O.; Levina, L.; Hoogland, S.; Kemp, K. W.; Ip, A. H.; Thon, S. M.; Sargent, E. H. Engineering Colloidal Quantum Dot Solids within and beyond the Mobility-Invariant Regime. *Nat. Commun.* **2014**, *5*.

(72)   Cao, Y.; Stavrinadis, A.; Lasanta, T.; So, D.; Konstantatos, G. The Role

of Surface Passivation for Efficient and Photostable PbS Quantum Dot Solar Cells. *Nat. Energy* **2016**, *1*, 16035.

(73) Ip, A. H.; Thon, S. M.; Hoogland, S.; Voznyy, O.; Zhitomirsky, D.; Debnath, R.; Levina, L.; Rollny, L. R.; Carey, G. H.; Fischer, A.; *et al.* Hybrid Passivated Colloidal Quantum Dot Solids. *Nat. Nanotechnol.* **2012**, *7*, 577–582.

(74) Carey, G. H.; Levina, L.; Comin, R.; Voznyy, O.; Sargent, E. H. Record Charge Carrier Diffusion Length in Colloidal Quantum Dot Solids via Mutual Dot-To-Dot Surface Passivation. *Adv. Mater.* **2015**, *27*, 3325–3330.

(75) Stavrinadis, A.; Rath, A. K.; de Arquer, F. P. G.; Diedenhofen, S. L.; Magén, C.; Martinez, L.; So, D.; Konstantatos, G. Heterovalent Cation Substitutional Doping for Quantum Dot Homojunction Solar Cells. *Nat. Commun.* **2013**, *4*, 2981.

(76) McDonald, S. a; Konstantatos, G.; Zhang, S.; Cyr, P. W.; Klem, E. J. D.; Levina, L.; Sargent, E. H. Solution-Processed PbS Quantum Dot Infrared Photodetectors and Photovoltaics. *Nat. Mater.* **2005**, *4*, 138–142.

(77) Yuan, M.; Liu, M.; Sargent, E. H. Colloidal Quantum Dot Solids for Solution-Processed Solar Cells. *Nat. Energy* **2016**, *1*, 16016.

(78) Gao, J.; Zhang, J.; van de Lagemaat, J.; Johnson, J. C.; Beard, M. C. Charge Generation in PbS Quantum Dot Solar Cells Characterized by Temperature-Dependent Steady-State Photoluminescence. *ACS Nano* **2014**, *8*, 12814–12825.

(79) Pattantyus-Abraham, A. G.; Kramer, I. J.; Barkhouse, A. R.; Wang, X.; Konstantatos, G.; Debnath, R.; Levina, L.; Raabe, I.; Nazeeruddin, M. K.; Grätzel, M.; *et al.* Depleted-Heterojunction Colloidal Quantum Dot Solar Cells. *ACS Nano* **2010**, *4*, 3374–3380.

(80) Piliego, C.; Protesescu, L.; Bisri, S. Z.; Kovalenko, M. V.; Loi, M. A. 5.2% Efficient PbS Nanocrystal Schottky Solar Cells. *Energy Environ. Sci.* **2013**, *6*, 3054.

(81) Strasfeld, D. B.; Dorn, A.; Wanger, D. D.; Bawendi, M. G. Imaging Schottky Barriers and Ohmic Contacts in PbS Quantum Dot Devices.

Nano Lett. **2012**, *12*, 569–575.

(82)   Luther, J. M.; Law, M.; Beard, M. C.; Song, Q.; Reese, M. O.; Ellingson, R. J.; Nozik, A. J. Schottky Solar Cells Based on Colloidal Nanocrystal Films. *Nano Lett.* **2008**, *8*, 3488–3492.

(83)   Clifford, J. P.; Johnston, K. W.; Levina, L.; Sargent, E. H. Schottky Barriers to Colloidal Quantum Dot Films. *Appl. Phys. Lett.* **2007**, *91*, 253117.

(84)   Barkhouse, D. A. R.; Debnath, R.; Kramer, I. J.; Zhitomirsky, D.; Pattantyus-Abraham, A. G.; Levina, L.; Etgar, L.; Grätzel, M.; Sargent, E. H. Depleted Bulk Heterojunction Colloidal Quantum Dot Photovoltaics. *Adv. Mater.* **2011**, *23*, 3134–3138.

(85)   Kawawaki, T.; Wang, H.; Kubo, T.; Saito, K.; Nakazaki, J.; Segawa, H.; Tatsuma, T. Efficiency Enhancement of PbS Quantum Dot/ZnO Nanowire Bulk-Heterojunction Solar Cells by Plasmonic Silver Nanocubes. *ACS Nano* **2015**, *9*, 4165–4172.

(86)   Rath, A. K.; Bernechea, M.; Martinez, L.; de Arquer, F. P. G.; Osmond, J.; Konstantatos, G. Solution-Processed Inorganic Bulk Nano-Heterojunctions and Their Application to Solar Cells. *Nat. Photonics* **2012**, *6*, 529–534.

(87)   Rath, A. K.; Pelayo Garcia de Arquer, F.; Stavrinadis, A.; Lasanta, T.; Bernechea, M.; Diedenhofen, S. L.; Konstantatos, G. Remote Trap Passivation in Colloidal Quantum Dot Bulk Nano-Heterojunctions and Its Effect in Solution-Processed Solar Cells. *Adv. Mater.* **2014**, *26*, 4741–4747.

(88)   Zhou, H.; Hsu, W.-C.; Duan, H.-S.; Bob, B.; Yang, W.; Song, T.-B.; Hsu, C.-J.; Yang, Y.; Ginley, D.; Green, M. A.; *et al.* CZTS Nanocrystals: A Promising Approach for next Generation Thin Film Photovoltaics. *Energy Environ. Sci.* **2013**, *6*, 2822.

(89)   Steinhagen, C.; Panthani, M. G.; Akhavan, V.; Goodfellow, B.; Koo, B.; Korgel, B. A. Synthesis of Cu_2ZnSnS_4 Nanocrystals for Use in Low-Cost Photovoltaics. *J. Am. Chem. Soc.* **2009**, *131*, 12554–12555.

(90)   Guo, Q.; Hillhouse, H. W.; Agrawal, R. Synthesis of Cu_2ZnSnS_4 Nanocrystal Ink and Its Use for Solar Cells. *J. Am. Chem. Soc.* **2009**, *131*,

11672–11673.

(91)   van Embden, J.; Chesman, A. S. R.; Della Gaspera, E.; Duffy, N. W.; Watkins, S. E.; Jasieniak, J. J. $Cu_2ZnSnS_XSe_{4-X}$ Solar Cells from Polar Nanocrystal Inks. *J. Am. Chem. Soc.* **2014**, *136*, 5237–5240.

(92)   Guo, Q.; Ford, G. M.; Yang, W.-C.; Walker, B. C.; Stach, E. A.; Hillhouse, H. W.; Agrawal, R. Fabrication of 7.2% Efficient CZTSSe Solar Cells Using CZTS Nanocrystals. *J. Am. Chem. Soc.* **2010**, *132*, 17384–17386.

(93)   Yang, S.; Zhao, P.; Zhao, X.; Qu, L.; Lai, X.; InP and Sn:InP Based Quantum Dot Sensitized Solar Cells. *J. Mater. Chem. A* **2015**, *3*, 21922–21929.

(94)   Chang, J. A.; Rhee, J. H.; Im, S. H.; Lee, Y. H.; Kim, H.; Seok, S. Il; Nazeeruddin, M. K.; Gratzel, M. High-Performance Nanostructured Inorganic−Organic Heterojunction Solar Cells. *Nano Lett.* **2010**, *10*, 2609–2612.

(95)   Wu, Y.; Wadia, C.; Ma, W.; Sadtler, B.; Alivisatos, A. P. Synthesis and Photovoltaic Application of Copper(I) Sulfide Nanocrystals. *Nano Lett.* **2008**, *8*, 2551–2555.

(96)   Martinez, L.; Bernechea, M.; de Arquer, F. P. G.; Konstantatos, G. Near IR-Sensitive, Non-Toxic, Polymer/Nanocrystal Solar Cells Employing Bi_2S_3 as the Electron Acceptor. *Adv. Energy Mater.* **2011**, *1*, 1029–1035.

(97)   Martinez, L.; Stavrinadis, A.; Higuchi, S.; Diedenhofen, S. L.; Bernechea, M.; Tajima, K.; Konstantatos, G. Hybrid Solution-Processed Bulk Heterojunction Solar Cells Based on Bismuth Sulfide Nanocrystals. *Phys. Chem. Chem. Phys.* **2013**, *15*, 5482.

(98)   Martinez, L.; Higuchi, S.; MacLachlan, A. J.; Stavrinadis, A.; Miller, N. C.; Diedenhofen, S. L.; Bernechea, M.; Sweetnam, S.; Nelson, J.; Haque, S. A.; *et al.* Improved Electronic Coupling in Hybrid Organic–inorganic Nanocomposites Employing Thiol-Functionalized P3HT and Bismuth Sulfide Nanocrystals. *Nanoscale* **2014**, *6*, 10018.

(99)   Bernechea, M.; Miller, N. C.; Xercavins, G.; So, D.; Stavrinadis, A.; Konstantatos, G. Solution-Processed Solar Cells Based on Environmentally Friendly $AgBiS_2$ Nanocrystals. *Nat. Photonics* **2016**.

110

(100) Luber, E. J.; Mobarok, M. H.; Buriak, J. M. Solution-Processed Zinc Phosphide (α-Zn_3P_2) Colloidal Semiconducting Nanocrystals for Thin Film Photovoltaic Applications. *ACS Nano* **2013**, *7*, 8136–8146.

(101) Wadia, C.; Alivisatos, A. P.; Kammen, D. M. Materials Availability Expands the Opportunity for Large-Scale Photovoltaics Deployment. *Environ. Sci. Technol.* **2009**, *43*, 2072–2077.

(102) Wadia, C.; Wu, Y.; Gul, S.; Volkman, S. K.; Guo, J.; Alivisatos, A. P. Surfactant-Assisted Hydrothermal Synthesis of Single Phase Pyrite FeS_2 Nanocrystals. *Chem. Mater.* **2009**, *21*, 2568–2570.

(103) Puthussery, J.; Seefeld, S.; Berry, N.; Gibbs, M.; Law, M. Colloidal Iron Pyrite (FeS_2) Nanocrystal Inks for Thin-Film Photovoltaics. *J. Am. Chem. Soc.* **2011**, *133*, 716–719.

(104) Cabán-Acevedo, M.; Kaiser, N. S.; English, C. R.; Liang, D.; Thompson, B. J.; Chen, H.-E.; Czech, K. J.; Wright, J. C.; Hamers, R. J.; Jin, S. Ionization of High-Density Deep Donor Defect States Explains the Low Photovoltage of Iron Pyrite Single Crystals. *J. Am. Chem. Soc.* **2014**, *136*, 17163–17179.

(105) Shukla, S.; Xing, G.; Ge, H.; Prabhakar, R. R.; Mathew, S.; Su, Z.; Nalla, V.; Venkatesan, T.; Mathews, N.; Sritharan, T.; *et al.* Origin of Photocarrier Losses in Iron Pyrite (FeS_2) Nanocubes. *ACS Nano* **2016**, *10*, 4431–4440.

(106) Steinhagen, C.; Harvey, T. B.; Stolle, C. J.; Harris, J.; Korgel, B. A. Pyrite Nanocrystal Solar Cells: Promising, or Fool's Gold? *J. Phys. Chem. Lett.* **2012**, *3*, 2352–2356.

(107) Aldakov, D.; Lefrançois, A.; Reiss, P. Ternary and Quaternary Metal Chalcogenide Nanocrystals: Synthesis, Properties and Applications. *J. Mater. Chem. C* **2013**, *1*, 3756.

(108) Siemer, K.; Klaer, J.; Luck, I.; Bruns, J.; Klenk, R.; Bräunig, D. Efficient $CuInS_2$ Solar Cells from a Rapid Thermal Process (RTP). *Sol. Energy Mater. Sol. Cells* **2001**, *67*, 159–166.

(109) Lany, S.; Zunger, A. Anion Vacancies as a Source of Persistent Photoconductivity in II-VI and Chalcopyrite Semiconductors. *Phys. Rev.*

B **2005**, *72*, 35215.

(110) Xie, R.; Rutherford, M.; Peng, X. Formation of High-Quality I−III−VI Semiconductor Nanocrystals by Tuning Relative Reactivity of Cationic Precursors. *J. Am. Chem. Soc.* **2009**, *131*, 5691–5697.

(111) Zhong, H.; Lo, S. S.; Mirkovic, T.; Li, Y.; Ding, Y.; Li, Y.; Scholes, G. D. Noninjection Gram-Scale Synthesis of Monodisperse Pyramidal CuInS$_2$ Nanocrystals and Their Size-Dependent Properties. *ACS Nano* **2010**, *4*, 5253–5262.

(112) Li, L.; Pandey, A.; Werder, D. J.; Khanal, B. P.; Pietryga, J. M.; Klimov, V. I. Efficient Synthesis of Highly Luminescent Copper Indium Sulfide-Based Core/Shell Nanocrystals with Surprisingly Long-Lived Emission. *J. Am. Chem. Soc.* **2011**, *133*, 1176–1179.

(113) Stolle, C. J.; Harvey, T. B.; Pernik, D. R.; Hibbert, J. I.; Du, J.; Rhee, D. J.; Akhavan, V. A.; Schaller, R. D.; Korgel, B. A. Multiexciton Solar Cells of CuInSe$_2$ Nanocrystals. *J. Phys. Chem. Lett.* **2014**, *5*, 304–309.

(114) Kolny-Olesiak, J.; Weller, H. Synthesis and Application of Colloidal CuInS$_2$ Semiconductor Nanocrystals. *ACS Appl. Mater. Interfaces* **2013**, *5*, 12221–12237.

(115) van der Stam, W.; Berends, A. C.; de Mello Donega, C. Prospects of Colloidal Copper Chalcogenide Nanocrystals. *ChemPhysChem* **2016**, *17*, 559–581.

(116) Liu, S.; Su, X. The Synthesis and Application of I–III–VI Type Quantum Dots. *RSC Adv.* **2014**, *4*, 43415–43428.

(117) Scheunemann, D.; Wilken, S.; Parisi, J.; Borchert, H. Towards Depleted Heterojunction Solar Cells with CuInS2 and ZnO Nanocrystals. *Appl. Phys. Lett.* **2013**, *103*, 133902.

(118) Scheunemann, D.; Wilken, S.; Parisi, J.; Borchert, H. Investigation of the Spatially Dependent Charge Collection Probability in CuInS$_2$/ZnO Colloidal Nanocrystal Solar Cells. *ACS Photonics* **2015**, *2*, 864–875.

(119) Borchert, H.; Scheunemann, D.; Frevert, K.; Witt, F.; Klein, A.; Parisi, J. Schottky Solar Cells with CuInS2 Nanocrystals as Absorber Material. *Zeitschrift für Phys. Chemie* **2015**, *229*, 191–203.

(120) Panthani, M. G.; Stolle, C. J.; Reid, D. K.; Rhee, D. J.; Harvey, T. B.; Akhavan, V. A.; Yu, Y.; Korgel, B. A. $CuInSe_2$ Quantum Dot Solar Cells with High Open-Circuit Voltage. *J. Phys. Chem. Lett.* **2013**, *4*, 2030–2034.

(121) Guo, Q.; Ford, G. M.; Hillhouse, H. W.; Agrawal, R. Sulfide Nanocrystal Inks for Dense $Cu(In_{1-X}Ga_x)(S_{1-Y}Se_Y)_2$ Absorber Films and Their Photovoltaic Performance. *Nano Lett.* **2009**, *9*, 3060–3065.

(122) Azimi, H.; Heumüller, T.; Gerl, A.; Matt, G.; Kubis, P.; Distaso, M.; Ahmad, R.; Akdas, T.; Richter, M.; Peukert, W.; *et al.* Relation of Nanostructure and Recombination Dynamics in a Low-Temperature Solution-Processed $CuInS_2$ Nanocrystalline Solar Cell. *Adv. Energy Mater.* **2013**, *3*, 1589–1596.

(123) Halpert, J. E.; Morgenstern, F. S. F.; Ehrler, B.; Vaynzof, Y.; Credgington, D.; Greenham, N. C. Charge Dynamics in Solution-Processed Nanocrystalline $CuInS_2$ Solar Cells. *ACS Nano* **2015**, *9*, 5857–5867.

(124) Li, L.; Coates, N.; Moses, D. Solution-Processed Inorganic Solar Cell Based on in Situ Synthesis and Film Deposition of $CuInS_2$ Nanocrystals. *J. Am. Chem. Soc.* **2010**, *132*, 22–23.

(125) Jeong, S.; Lee, B.-S.; Ahn, S.; Yoon, K.; Seo, Y.-H.; Choi, Y.; Ryu, B.-H. An 8.2% Efficient Solution-Processed $CuInSe_2$ Solar Cell Based on Multiphase $CuInSe_2$ Nanoparticles. *Energy Environ. Sci.* **2012**, *5*, 7539.

(126) McDaniel, H.; Fuke, N.; Pietryga, J. M.; Klimov, V. I. Engineered $CuInSe_XS_{2-X}$ Quantum Dots for Sensitized Solar Cells. *J. Phys. Chem. Lett.* **2013**, *4*, 355–361.

(127) Jara, D. H.; Yoon, S. J.; Stamplecoskie, K. G.; Kamat, P. V. Size-Dependent Photovoltaic Performance of $CuInS_2$ Quantum Dot-Sensitized Solar Cells. *Chem. Mater.* **2014**, *26*, 7221–7228.

(128) Knowles, K. E.; Hartstein, K. H.; Kilburn, T. B.; Marchioro, A.; Nelson, H. D.; Whitham, P. J.; Gamelin, D. R. Luminescent Colloidal Semiconductor Nanocrystals Containing Copper: Synthesis, Photophysics, and Applications. *Chem. Rev.* **2016**, acs.chemrev.6b00048.

(129) Akdas, T.; Distaso, M.; Kuhri, S.; Winter, B.; Birajdar, B.; Spiecker, E.;

Guldi, D. M.; Peukert, W. The Effects of Post-Processing on the Surface and the Optical Properties of Copper Indium Sulfide Quantum Dots. *J. Colloid Interface Sci.* **2015**, *445*, 337–347.

(130) Lefrançois, A.; Pouget, S.; Vaure, L.; Lopez-Haro, M.; Reiss, P. Direct Synthesis of Highly Conductive *Tert* -Butylthiol-Capped $CuInS_2$ Nanocrystals. *ChemPhysChem* **2016**, *17*, 654–659.

(131) Turo, M. J.; Macdonald, J. E. Crystal-Bound *vs* Surface-Bound Thiols on Nanocrystals. *ACS Nano* **2014**, *8*, 10205–10213.

(132) Dierick, R.; Van den Broeck, F.; De Nolf, K.; Zhao, Q.; Vantomme, A.; Martins, J. C.; Hens, Z. Surface Chemistry of $CuInS_2$ Colloidal Nanocrystals, Tight Binding of L-Type Ligands. *Chem. Mater.* **2014**, *26*, 5950–5957.

(133) Allen, P. M.; Bawendi, M. G. Ternary I−III−VI Quantum Dots Luminescent in the Red to Near-Infrared. *J. Am. Chem. Soc.* **2008**, *130*, 9240–9241.

(134) Niezgoda, J. S.; Yap, E.; Keene, J. D.; McBride, J. R.; Rosenthal, S. J. Plasmonic $Cu_X In_Y S_2$ Quantum Dots Make Better Photovoltaics Than Their Nonplasmonic Counterparts. *Nano Lett.* **2014**, *14*, 3262–3269.

(135) Wang, X.; Swihart, M. T. Controlling the Size, Shape, Phase, Band Gap, and Localized Surface Plasmon Resonance of $Cu_{2-X} S$ and $Cu_X In_Y S$ Nanocrystals. *Chem. Mater.* **2015**, *27*, 1786–1791.

(136) Park, J.; Kim, S.-W. $CuInS_2$/ZnS Core/shell Quantum Dots by Cation Exchange and Their Blue-Shifted Photoluminescence. *J. Mater. Chem.* **2011**, *21*, 3745.

(137) De Trizio, L.; Prato, M.; Genovese, A.; Casu, A.; Povia, M.; Simonutti, R.; Alcocer, M. J. P.; D'Andrea, C.; Tassone, F.; Manna, L. Strongly Fluorescent Quaternary Cu–In–Zn–S Nanocrystals Prepared from $Cu_{1-X} InS_2$ Nanocrystals by Partial Cation Exchange. *Chem. Mater.* **2012**, *24*, 2400–2406.

(138) Shabaev, A.; Mehl, M. J.; Efros, A. L. Energy Band Structure of $CuInS_2$ and Optical Spectra of $CuInS_2$ Nanocrystals. *Phys. Rev. B* **2015**, *92*, 35431.

114

(139) Leach, A. D. P.; Macdonald, J. E. Optoelectronic Properties of CuInS$_2$ Nanocrystals and Their Origin. *J. Phys. Chem. Lett.* **2016**, *7*, 572–583.

(140) Zhong, H.; Zhou, Y.; Ye, M.; He, Y.; Ye, J.; He, C.; Yang, C.; Li, Y. Controlled Synthesis and Optical Properties of Colloidal Ternary Chalcogenide CuInS$_2$ Nanocrystals. *Chem. Mater.* **2008**, *20*, 6434–6443.

(141) Castro, S. L.; Bailey, S. G.; Raffaelle, R. P.; Banger, K. K.; Hepp, A. F. Synthesis and Characterization of Colloidal CuInS$_2$ Nanoparticles from a Molecular Single-Source Precursor. *J. Phys. Chem. B* **2004**, *108*, 12429–12435.

(142) Omata, T.; Nose, K.; Kurimoto, K.; Kita, M. Electronic Transition Responsible for Size-Dependent Photoluminescence of Colloidal CuInS$_2$ Quantum Dots. *J. Mater. Chem. C* **2014**, *2*, 6867.

(143) Liu, W.; Zhang, Y.; Zhai, W.; Wang, Y.; Zhang, T.; Gu, P.; Chu, H.; Zhang, H.; Cui, T.; Wang, Y.; *et al.* Temperature-Dependent Photoluminescence of ZnCuInS/ZnSe/ZnS Quantum Dots. *J. Phys. Chem. C* **2013**, 130912104257009.

(144) Lei, S.; Wang, C.; Liu, L.; Guo, D.; Wang, C.; Tang, Q.; Cheng, B.; Xiao, Y.; Zhou, L. Spinel Indium Sulfide Precursor for the Phase-Selective Synthesis of Cu–In–S Nanocrystals with Zinc-Blende, Wurtzite, and Spinel Structures. *Chem. Mater.* **2013**, *25*, 2991–2997.

(145) Pan, D.; An, L.; Sun, Z.; Hou, W.; Yang, Y.; Yang, Z.; Lu, Y. Synthesis of Cu−In−S Ternary Nanocrystals with Tunable Structure and Composition. *J. Am. Chem. Soc.* **2008**, *130*, 5620–5621.

(146) Oja, I.; Nanu, M.; Katerski, A.; Krunks, M.; Mere, A.; Raudoja, J.; Goossens, A. Crystal Quality Studies of CuInS$_2$ Films Prepared by Spray Pyrolysis. *Thin Solid Films* **2005**, *480*, 82–86.

(147) Omata, T.; Nose, K.; Otsuka-Yao-Matsuo, S. Size Dependent Optical Band Gap of Ternary I-III-VI$_2$ Semiconductor Nanocrystals. *J. Appl. Phys.* **2009**, *105*, 73106.

(148) Czekelius, C.; Hilgendorff, M.; Spanhel, L.; Bedja, I.; Lerch, M.; Müller, G.; Bloeck, U.; Su, D.-S.; Giersig, M. A Simple Colloidal Route to Nanocrystalline ZnO/CuInS$_2$ Bilayers. *Adv. Mater.* **1999**, *11*, 643–646.

(149) Chen, B.; Zhong, H.; Zhang, W.; Tan, Z.; Li, Y.; Yu, C.; Zhai, T.; Bando, Y.; Yang, S.; Zou, B. Highly Emissive and Color-Tunable CuInS$_2$-Based Colloidal Semiconductor Nanocrystals: Off-Stoichiometry Effects and Improved Electroluminescence Performance. *Adv. Funct. Mater.* **2012**, *22*, 2081–2088.

(150) Yazdani, N.; Bozyigit, D.; Yarema, O.; Yarema, M.; Wood, V. Hole Mobility in Nanocrystal Solids as a Function of Constituent Nanocrystal Size. *J. Phys. Chem. Lett.* **2014**, *5*, 3522–3527.

(151) Stolle, C. J.; Panthani, M. G.; Harvey, T. B.; Akhavan, V. A.; Korgel, B. A. Comparison of the Photovoltaic Response of Oleylamine and Inorganic Ligand-Capped CuInSe$_2$ Nanocrystals. *ACS Appl. Mater. Interfaces* **2012**, *4*, 2757–2761.

(152) Clark, S. W.; Harbold, J. M.; Wise, F. W. Resonant Energy Transfer in PbS Quantum Dots. *J. Phys. Chem. C* **2007**, *111*, 7302–7305.

(153) Lingley, Z.; Lu, S.; Madhukar, A. The Dynamics of Energy and Charge Transfer in Lead Sulfide Quantum Dot Solids. *J. Appl. Phys.* **2014**, *115*, 84302.

(154) Choi, J. J.; Luria, J.; Hyun, B.-R.; Bartnik, A. C.; Sun, L.; Lim, Y.-F.; Marohn, J. A.; Wise, F. W.; Hanrath, T. Photogenerated Exciton Dissociation in Highly Coupled Lead Salt Nanocrystal Assemblies. *Nano Lett.* **2010**, *10*, 1805–1811.

(155) Mork, A. J.; Weidman, M. C.; Prins, F.; Tisdale, W. A. Magnitude of the Förster Radius in Colloidal Quantum Dot Solids. *J. Phys. Chem. C* **2014**, *118*, 13920–13928.

(156) Meulenberg, R. W.; Lee, J. R. I.; Wolcott, A.; Zhang, J. Z.; Terminello, L. J.; van Buuren, T. Determination of the Exciton Binding Energy in CdSe Quantum Dots. *ACS Nano* **2009**, *3*, 325–330.

(157) Draguta, S.; McDaniel, H.; Klimov, V. I. Tuning Carrier Mobilities and Polarity of Charge Transport in Films of CuInSe$_x$S$_{2-x}$ Quantum Dots. *Adv. Mater.* **2015**, *27*, 1701–1705.

(158) Li, L.; Auer, E.; Liao, M.; Fang, X.; Zhai, T.; Gautam, U. K.; Lugstein, A.; Koide, Y.; Bando, Y.; Golberg, D. Deep-Ultraviolet Solar-Blind Photoconductivity of Individual Gallium Oxide Nanobelts. *Nanoscale*

2011, *3*, 1120.

(159) Konstantatos, G.; Clifford, J.; Levina, L.; Sargent, E. H. Sensitive Solution-Processed Visible-Wavelength Photodetectors. *Nat. Photonics* **2007**, *1*, 531–534.

(160) Park, S.; Lim, B. T.; Kim, B.; Son, H. J.; Chung, D. S. High Mobility Polymer Based on a π-Extended Benzodithiophene and Its Application for Fast Switching Transistor and High Gain Photoconductor. *Sci. Rep.* **2014**, *4*, 3–24.

(161) Chen, B.; Chang, S.; Li, D.; Chen, L.; Wang, Y.; Chen, T.; Zou, B.; Zhong, H.; Rogach, A. L. Template Synthesis of $CuInS_2$ Nanocrystals from In_2S_3 Nanoplates and Their Application as Counter Electrodes in Dye-Sensitized Solar Cells. *Chem. Mater.* **2015**, *27*, 5949–5956.

(162) Bozyigit, D.; Lin, W. M. M.; Yazdani, N.; Yarema, O.; Wood, V. A Quantitative Model for Charge Carrier Transport, Trapping and Recombination in Nanocrystal-Based Solar Cells. *Nat. Commun.* **2015**, *6*, 6180.

(163) Jasieniak, J.; Califano, M.; Watkins, S. E. Size-Dependent Valence and Conduction Band-Edge Energies of Semiconductor Nanocrystals. *ACS Nano* **2011**, *5*, 5888–5902.

(164) Sun, J.; Zhao, J.; Masumoto, Y. Shell-Thickness-Dependent Photoinduced Electron Transfer from $CuInS_2/ZnS$ Quantum Dots to TiO_2 Films. *Appl. Phys. Lett.* **2013**, *102*, 53119.

(165) Krause, C.; Scheunemann, D.; Parisi, J.; Borchert, H. Three-Dimensional Morphology of $CuInS_2$:P3HT Hybrid Blends for Photovoltaic Applications. *J. Appl. Phys.* **2015**, *118*, 205501.

(166) Rath, T.; Edler, M.; Haas, W.; Fischereder, A.; Moscher, S.; Schenk, A.; Trattnig, R.; Sezen, M.; Mauthner, G.; Pein, A.; *et al.* A Direct Route Towards Polymer/Copper Indium Sulfide Nanocomposite Solar Cells. *Adv. Energy Mater.* **2011**, *1*, 1046–1050.

(167) Nanu, M.; Schoonman, J.; Goossens, A. Nanocomposite Three-Dimensional Solar Cells Obtained by Chemical Spray Deposition. *Nano Lett.* **2005**, *5*, 1716–1719.

(168) Cheshmekhavar, A. H.; Mahjoub, A. R.; Fakhri, H.; Dehghani, M. An All Solution-Based Process for the Fabrication of Superstrate-Type Configuration CuInS$_2$ Thin Film Solar Cells. *RSC Adv.* **2015**, *5*, 97381–97390.

(169) Chen, Z.; Tang, M.; Song, L.; Tang, G.; Zhang, B.; Zhang, L.; Yang, J.; Hu, J. In Situ Growth of CuInS$_2$ Nanocrystals on Nanoporous TiO$_2$ Film for Constructing Inorganic/organic Heterojunction Solar Cells. *Nanoscale Res. Lett.* **2013**, *8*, 354.

(170) So, D.; Konstantatos, G. Thiol-Free Synthesized Copper Indium Sulfide Nanocrystals as Optoelectronic Quantum Dot Solids. *Chem. Mater.* **2015**, *27*, 8424–8432.

(171) Levcenko, S.; Syrbu, N. N.; Tezlevan, V. E.; Arushanov, E.; Doka-Yamigno, S.; Schedel-Niedrig, T.; Lux-Steiner, M. C. Optical Spectra and Energy Band Structure of Single Crystalline CuGaS$_2$ and CuInS$_2$. *J. Phys. Condens. Matter* **2007**, *19*, 456222.

(172) Barkhouse, D. A. R.; Pattantyus-Abraham, A. G.; Levina, L.; Sargent, E. H. Thiols Passivate Recombination Centers in Colloidal Quantum Dots Leading to Enhanced Photovoltaic Device Efficiency. *ACS Nano* **2008**, *2*, 2356–2362.

(173) Jean, J.; Chang, S.; Brown, P. R.; Cheng, J. J.; Rekemeyer, P. H.; Bawendi, M. G.; Gradečak, S.; Bulović, V. ZnO Nanowire Arrays for Enhanced Photocurrent in PbS Quantum Dot Solar Cells. *Adv. Mater.* **2013**, *25*, 2790–2796.

(174) Wang, H.; Gonzalez-Pedro, V.; Kubo, T.; Fabregat-Santiago, F.; Bisquert, J.; Sanehira, Y.; Nakazaki, J.; Segawa, H. Enhanced Carrier Transport Distance in Colloidal PbS Quantum-Dot-Based Solar Cells Using ZnO Nanowires. *J. Phys. Chem. C* **2015**, *119*, 27265–27274.

(175) Lee, D.; Yong, K. ZnO-Based Nanostructuring Strategy Using an Optimized Solution Process in CuInS$_2$ Superstrate Photovoltaics. *J. Phys. Chem. C* **2014**, *118*, 7788–7800.

(176) Sun, Z.; Sitbon, G.; Pons, T.; Bakulin, A. A.; Chen, Z. Reduced Carrier Recombination in PbS - CuInS$_2$ Quantum Dot Solar Cells. *Sci. Rep.* **2015**, *5*, 10626.

(177) Chung, C.-H.; Bob, B.; Song, T.-B.; Yang, Y. Current–voltage Characteristics of Fully Solution Processed High Performance CuIn(S,Se)$_2$ Solar Cells: Crossover and Red Kink. *Sol. Energy Mater. Sol. Cells* **2014**, *120*, 642–646.

(178) Zhao, N.; Osedach, T. P.; Chang, L.-Y.; Geyer, S. M.; Wanger, D.; Binda, M. T.; Arango, A. C. et al Colloidal PbS Quantum Dot Solar Cells with High Fill Factor. *ACS Nano* **2010**, *4*, 3743–3752.

(179) Hages, C. J.; Carter, N. J.; Agrawal, R. Generalized Quantum Efficiency Analysis for Non-Ideal Solar Cells: Case of Cu2ZnSnSe$_4$. *J. Appl. Phys.* **2016**, *119*, 14505.

(180) Troviano, M.; Taretto, K. Temperature-Dependent Quantum Efficiency Analysis of Graded-Gap Cu(In,Ga)Se$_2$ Solar Cells. *Sol. Energy Mater. Sol. Cells* **2011**, *95*, 3081–3086.

(181) Foertig, A.; Rauh, J.; Dyakonov, V.; Deibel, C. Shockley Equation Parameters of P3HT:PCBM Solar Cells Determined by Transient Techniques. *Phys. Rev. B* **2012**, *86*, 115302.

(182) Kirchartz, T.; Pieters, B. E.; Kirkpatrick, J.; Rau, U.; Nelson, J. Recombination via Tail States in Polythiophene:fullerene Solar Cells. *Phys. Rev. B* **2011**, *83*, 115209.

(183) Knowles, K. E.; Nelson, H. D.; Kilburn, T. B.; Gamelin, D. R. Singlet–Triplet Splittings in the Luminescent Excited States of Colloidal Cu$^+$:CdSe, Cu$^+$:InP, and CuInS$_2$ Nanocrystals: Charge-Transfer Configurations and Self-Trapped Excitons. *J. Am. Chem. Soc.* **2015**, *137*, 13138–13147.

(184) Hages, C. J.; Koeper, M. J.; Agrawal, R. Optoelectronic and Material Properties of Nanocrystal-Based CZTSe Absorbers with Ag-Alloying. *Sol. Energy Mater. Sol. Cells* **2016**, *145*, 342–348.

(185) Miranti, R.; Krause, C.; Parisi, J.; Borchert, H. Charge Transport through Thin Films Made of Colloidal CuInS$_2$ Nanocrystals. *Mater. Res. Express* **2015**, *2*, 66401.

(186) So, D.; Pradhan, S.; Konstantatos, G. Solid-State Colloidal CuInS$_2$ Quantum Dot Solar Cells Enabled by Bulk Heterojunctions. *Nanoscale,* in press, **DOI:** 10.1039/C6NR05563J, **2016**.

120